Receiver Design for Multi-band Ultra-Wideband Systems

WONG SAI HO

(B.Eng (Hons.), NUS)

A THESIS SUBMITTED

FOR THE DEGREE OF MASTER OF ENGINEERING

DEPARTMENT OF ELECTRICAL AND COMPUTER ENGINEERING

NATIONAL UNIVERSITY OF SINGAPORE

2004

Acknowledgments

I would like to thank Dr Francois Chin for his advices, focus, and preparatory talks to keep me on track.

I am indebted to Mr Peng Xiaoming, who has been selfless for the many hours of help, suggestions, ideas and advices.

I would also like to thank Dr AS Madhukumar, who has given me a year of useful guidance.

Most importantly to God, whose love has no bandwidth.

Table of Contents

Summary

Ultra Wideband (UWB) has been identified as a possible key technology for high data rate systems such as wireless personal area network. Of particular interest is multi-band UWB system, which divides the available spectrum into multiple bands. The multi-band UWB system has the flexibility to eliminate interference and coexistence problems with narrowband systems by turning off the affected bands. Multi-band UWB is also able to support high data rate with relatively low pulse repetition interval.

This work concentrates on the receiver design of multi-band UWB systems, exploiting the unique characteristics of the UWB channel, which has been represented by 4 channel models provided by IEEE. To harness the inherent flexibility of multi-band UWB, investigations have been based on 3 transmission modes. Each mode is able to handle inter-symbol interference (ISI) of different degrees.

Various aspects of the multi-band UWB receiver have been considered, including receiver filter design, acquisition, equalization, coding and multi-user interference issues. This work recommends a common low pass filter design for all transmission bands that has high energy captured and favorable correlation properties. This work proposes a rapid acquisition design that makes use of certain properties special only to multi-band UWB. It also includes a simplified concatenated coding scheme that is powerful and yet of low complexity, by employing Reed-Solomon codes as the outer code and Quadrature M-ary Orthogonal Keying as the inner code. Lastly, special emphasis has been placed on the equalization performance study, comparing between MMSE and RAKE, two often-used UWB receiver schemes. Over-sampling equalization has been proposed, which has been shown to achieve temporal diversity.

The results demonstrated that while ISI caused error floor in RAKE receiver in some modes, over-sampling MMSE equalization was effective in ISI-alleviation at all modes and channel models. With the proposed concatenated coding, the bit error rate performance was further improved. Coded over-sampling MMSE equalizer was also shown to be able to counter multi-user interference, handling piconet collision of different severity.

List of Figures

List of Tables

Nomenclature

List of Symbols

α	Multipath gain coefficient
ϕ	Phase difference between LO and received signal
$\otimes$	Convolution operation
$\delta(t)$	Dirac-delta function
η	Over-sampling factor
η_0	Number of samples within one PRI
$\tau_{k,l}$	*k*th multipath component relative to the *l*th cluster
τ_{max}	Maximum delay spread
b_m	Data symbols
c	Tap weights
c(t)	LO signal
C^*	Conjugate of any complex number C
C_{16}	CAZAC sequence of length-16
${}_pC^N_{16x6}$	Starting phase p of a zero-inserted CAZAC-16 code repeated N times
ceil	Ceiling function
$\mathbf{C}^H$	Conjugate transpose of any complex matrix **C**
c_n	n^{th} element of CAZAC sequence
D_m	Data rate for a multi-band system
D_{min}	Minimum distance of RS code
D_s	Data rate for a single band system
f(t)	Impulse response of LPF
f_c	Center frequency of the various sub-bands

f_{pass}	Passband Frequency for LPF
f_s	Sampling frequency
h(t)	Channel impulse response
$\mathbf{I_k}$	Identity matrix of order k
K	RS code symbol length
k	Bits per symbol
K_4	Barker sequence of length-4
${}_pK^N_{4x6}$	Starting phase p of a zero-inserted Barker-4 code repeated N times
K_c	Constraint length of convolutional code
k_n	n^{th} element of Barker sequence
L_b	Number of strongest multipaths
L_p	Number of multipaths, starting from the first
L_r	Number of resolvable multipaths
m(t)	Data pulse
N	RS code word length
N_0	Noise power
N_B	Number of bands in multi-band UWB system
N_{IB}	Number of interfering bands per piconet
N_{ISI}	Number of pulses corrupted by ISI
N_P	Number of simultaneously operating piconets
N_q	Length of preamble sequence
N_w	Length of correlation window for RST
P	Transmitted power
$p_c(t)$	Transmitted pulse (in-phase component)

P_{eb}	Reed-Solomon code bit error probability
P_{es}	Reed-Solomon code symbol error probability
P_{ew}	Reed-Solomon code word error probability
P_{fa}	Probability of false alarm
P_m	Probability of miss
P_M	Symbol error rate of an uncoded system
P_{qb}	QMOK code bit error probability
P_{qs}	QMOK code symbol error probability
$p_s(t)$	Transmitted pulse (quadrature component)
q(n)	The n^{th} element of the preamble sequence
R(m)	Periodic auto-correlation of shift m
R_c	Code rate
t	Maximum number of symbol errors that can be corrected by RS code
T_l	Delay of the l^{th} multipath cluster
T_s	Pulse repetition internal
T_u	Time uncertainty of slide-correlator
T_w	Data pulse width
T_w'	Effective pulse width

List of Abbreviations

AWGN	Additive white gaussian noise
BER	Bit error rate
BPSK	Binary phase shift keying
CAZAC	Constant amplitude zero auto-correlation
CC	Convolutional code
FEC	Forward error correction
ISI	Inter-symbol interference
LO	Local oscillator
LOS	Line-of-sight
LPF	Low pass filter
MAI	Multiple-access interference
Mbps	Mega bits-per-second
Mpps	Mega pulse-per-second
MMSE	Minimum mean square error
MRC	Maximum ratio combining
NLOS	Non line-of-sight
PRI	Pulse repetition internal
PSD	Power spectral density
QMOK	Quadrature M-ary Orthogonal Keying
RF	Radio frequency
RS	Reed-Solomon
RST	Ratio statistics test
SER	Symbol error rate
SNR	Signal-to-noise ratio

TF	Time-frequency
UWB	Ultra wideband

Chapter 1 Introduction

Ultra-wideband (UWB) technology has generated much interest and discussion since its inception by Federal Communication Commission (FCC) in 2002 [1]. Monopulses, with a pulse width of nanoseconds, are used to transmit data. The resulting system is able to achieve high data rate with relatively low power consumption. This scheme is known as single-band UWB, since the nanosecond monopulses occupy most of the available spectrum allowed that spans from 3.1Ghz to 10.6GHz. The power-spectral density (PSD) of the signal is even lower than the noise floor [2], as the radiated energy is spread over a large bandwidth.

Different flavors of single-band UWB have been proposed, such as pulse-position modulation (PPM) in [3], biphase modulation (BPM) in [4] and pulse amplitude modulation (PAM) in [5]. Being "carrierless" is a frequently quoted advantage of single-band UWB. The frequency of the data-carrying UWB monopulses is in the orders of GHz, thus eliminating the need for up- or down-conversion before transmission. Local oscillators (LOs), mixers and other components, commonly found in narrowband systems for intermediate frequency operations, are not required [6]. This simplifies the transceiver design and reduces power consumption when compared to traditional narrowband communication systems.

Since UWB systems have the potential to support very high data rate at short range with relatively easy-to-build and cheap components with low power, it is an attractive candidate for wireless personal networks (WPANs). In fact the IEEE 802.15 Task Group 3a (TG3a) specializes in the standardization of UWB as the physical layer for WPANs at high data rates and short distances. In order to compare the performance of

different proposals, TG3a has provided 4 channel models (CMs) to simulate the channel characteristics peculiar to UWB systems [7]. This is because conventional models for narrowband signals do not accurately describe the short pulse and dense multipath environment that UWB is operating in. These conventional methods are also insufficient to model the line-of-sight (LOS) and non line-of-sight (NLOS) UWB channels that have different delay spreads and path loss parameters. UWB multipath components do not come arrive at a continuum but in clusters, and do not suffer from fading that results from destructive interference of the reflected multipath pulses. The IEEE channel models are able to address these features and details on the CMs are given in Section 2.1.

The very wide bandwidth occupied by single-band UWB spells concern for interference and coexistence issues with existing narrowband systems. In fact interference to global positioning system (GPS) and other narrowband communication systems by UWB has been a major deciding factor in the approval process by FCC. Within the allowed bandwidth for UWB usage, a major interferer comes from 802.11a operating at the vicinity of 5GHz. Elaborate efforts have been put to mitigate this in-band interference for single-band UWB, for example in [8]-[9].

To this end, multi-band UWB has been proposed, in which the very wide bandwidth allowed for UWB applications is divided into N_B different sub-bands. Each sub-band occupies a 10-dB bandwidth of at least 500MHz, as required by the FCC ruling. The bands that are susceptible to existing narrowband interference, for example at the vicinity of 5GHz, are simply turn off. This is an elegant solution to the interference problem, with some added transceiver complexity. Up- and down-conversion is

necessary to transmit the data bits, and the transceiver needs to switch to the different bands at various transmit instances. This could increase the cost and power consumption of multi-band UWB systems. Multi-band UWB is more scalable as it can be made adaptive to the different channel conditions. This can be achieved by varying the pulse-repetition interval (PRI) of each sub-band. In an adverse channel with a long delay spread, a longer PRI can be used to combat inter-symbol interference (ISI). In a single-band system this would decrease the data rate, but in multi-band UWB, a high data rate can be obtained even with a long PRI. This would be explained in Section 2.2. This also allows the pulsed sub-bands to be transmitted in non-overlapping time intervals, significantly reducing the PAR problem common to multicarrier systems. A reduction in ISI is also beneficial to acquisition purposes, since the preambles that are used for acquisition are usually not protected by coding. Besides, the receiver processes such as coding can be better exploited, with better energy collection and bit-error rate (BER) performance.

Multi-band UWB provides for multiple access, in which each user is given a time frequency (TF) sequence for transmission. At each switched instance, different users can transmit at different bands. Take N_B=6 for example, there are 6!=720 TF sequences available. A more detailed comparison between single- and multi-band UWB can be found in [10]. The transceiver for the multi-band UWB system is shown in Figure 1.1.

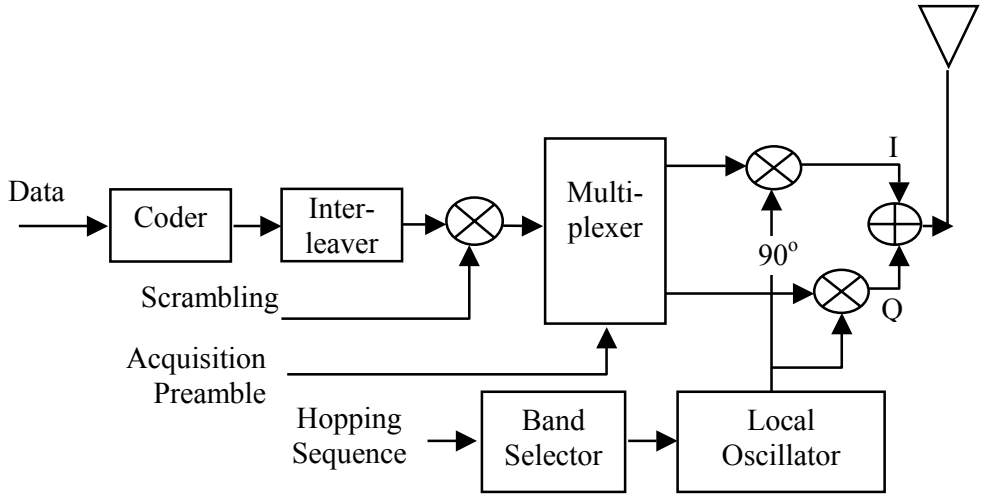

(a) Transmitter

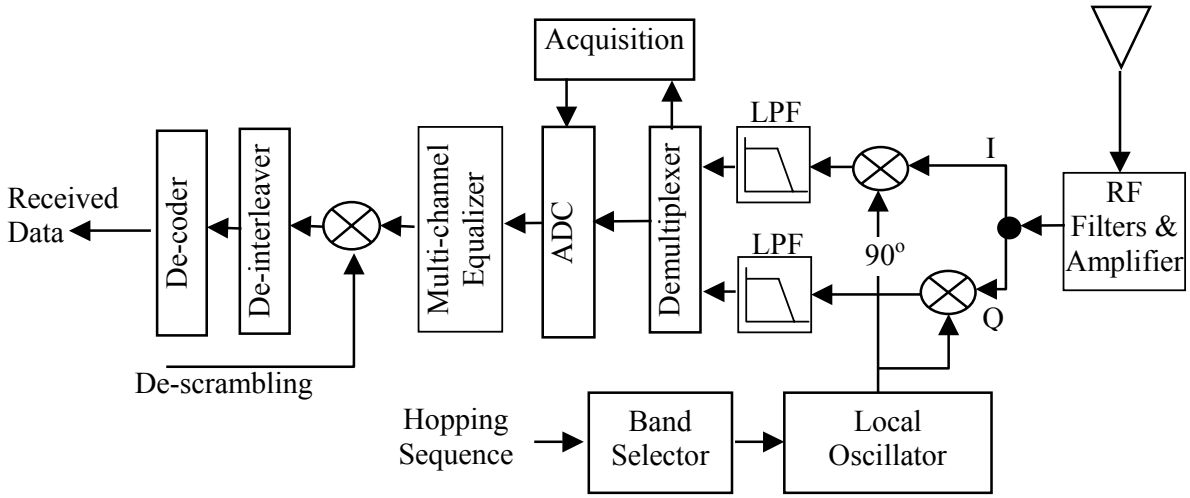

(b) Receiver

Figure 1.1 – Transceiver structure for multi-band UWB

1.1 Scope of Thesis

As mentioned, multi-band UWB has the potential to achieve high data rate over short distances without suffering from narrowband interference, at the same time being more adaptive and scalable than single-band implementation. Traditional narrowband channel analysis is not applicable, due to the narrow pulse width used.

The object of this work is to make design considerations for a multi-band UWB receiver, based on the IEEE UWB channel models. In the existing literature, there are very few receiver analyses for multi-band UWB. It is hoped that by capitalizing on the distinctive features of multi-band UWB, the findings of this thesis are able to make a positive contribution to the receiver design. The areas that are investigated include receiver low pass filter (LPF) design, acquisition, multi-channel equalization, coding and lastly multiple access interference. In fact most of the blocks in Figure 1.1(b) are covered in this work. Such considerations are useful due to the notable differences between UWB and narrowband systems. The availability of an accepted channel model allows for dedicated schemes that exploit the pertinent channel characteristics unique only to UWB systems. The high rate nature of UWB also calls for detailed analysis into the various receiver operations, and make suitable provisions due to hardware constrains.

Proposal for each component was tested with extensive simulation studies. Simulations were based on the IEEE channel models applied to different transmission modes, and to simplify analysis, perfect channel estimation was assumed. Special emphasis has been put into the analysis and comparison of the effectiveness of the over-sampling

minimum mean square error (MMSE) and RAKE receivers in multi-band UWB settings, two popular receiver schemes for UWB systems.

1.2 Organization of Thesis

In Chapter 2, the background of multi-band UWB, its system model and the IEEE channel models are provided. Three transmission modes, which represent different PRIs, are introduced. The characteristics of multi-band UWB are presented, and these parameters, together with the IEEE channel models are used throughout this work.

In Chapter 3, the issue of receiver LPF design is investigated. The choice of a practical filter, which can be used for all sub-bands, is demonstrated. The choice of LPF is based on certain metrics, and is discussed in details in that chapter.

In Chapter 4, an acquisition scheme suitable for multi-band UWB is proposed. This scheme makes use of certain channel characteristics that is unique only to UWB channels to reduce acquisition time. Two different preamble sequences have been tested and compared for the use for the proposed acquisition scheme.

In Chapter 5, the analysis and simulation results for a multi-channel over-sampling MMSE and RAKE receiver are given. The over-sampling proposal is demonstrated to achieve temporal diversity. These two popular receivers operations have been simulated in different transmission modes and channel models, and the effects of ISI on the BER performance of each scheme are investigated.

In Chapter 6, a coding scheme that is suitable for multi-band UWB is presented. The proposed code consists of the concatenation of two linear codes, as high-speed linear coders/decoders are less prohibitive in cost than its convolutional counterparts. Single-

streaming and multi-streaming, two different implementations in which data bits are sent on the sub-bands, is investigated also.

Chapter 7 takes multi-band UWB into multi-user environment, and investigates the effects of multiple-access interference (MAI) on the proposed coding and receiver scheme.

The whole thesis will be concluded in Chapter 8, summarizing the findings of this work and proposing areas for future research.

Chapter 2 Background Information

This chapter provides the important parameters that are used throughout this work. Firstly, a brief overview of the IEEE channel model and the prominent characteristics of the UWB channel are presented. These parameters have a great influence on the receiver design. Secondly, the system overview of the multi-band UWB system and the 3 transmission modes are introduced. These 3 transmission modes are of different PRIs and sampling rates, allowing adaptivity to the channel.

2.1 IEEE Channel Model

UWB systems suffer from severe multipath effects [11], and the received signals contain a significant number of resolvable multipath components [12]-[13]. They arrive in clusters rather than uniformly spread in time. Due to the very narrow pulses used, these components do not overlap in time domain, thus reducing fading. Unlike narrowband Rayleigh fading, UWB channel fading has been shown to be log-normally distributed.

In order to accurately represent the unique characteristics of a UWB propagation channel, the IEEE 802.15.3a standards task group has established standard channel models for the evaluation of UWB systems. Four channel models have been proposed, each characterizing a practical UWB propagation channel, they are:

- CM1 – Line-of-sight (LOS) 0-4 meters
- CM2 – Non line-of-sight (NLOS) 0-4 meters
- CM3 – Non line-of-sight 4-10 meters
- CM4 – Extreme non line-of-sight

The salient characteristics of each CM can be found in [7], from which it can be observed that CM1 has the least delay spread, and it increases through CM2 and CM3, and CM4 has the longest delay spread. This can be deduced form the fact that CM1 is a LOS channels, while CM2, CM3 and CM4 are NLOS ones with increasing distance between the transmitter and receiver. The impulse response h(t) of any CM can be represented by

$$h(t) = \mathrm{X}\sum_{l=0}^{L}\sum_{k=0}^{K}\alpha_{k,l}\delta(t - T_l - \tau_{k,l}) \tag{2.1}$$

in which $\alpha_{k,l}$ are the multipath gain coefficients, T_l is the delay of the lth cluster, $\tau_{k,l}$ is the delay of the kth multipath component relative to the lth cluster, and X represents log-normal shadowing.

2.2 Multi-band System Overview

As mentioned, the available spectrum for UWB is divided into multiple bands. In this work, a 7 bands model was used. One of the bands was turned off for 802.11a coexistence, making $N_B = 6$. The frequency allocation of each band is recorded in Table 2.1. Pulse shaping is done by the rectified cosine function with pulse width T_w for constraining the signal within the specified transmission band. The in-phase component $p_c(t)$ of the transmitted pulse is described by (2.2), and $p_c(t)$ for the first transmission band is illustrated in Figure 2.1. The quadrature component $p_s(t)$ is described by (2.3).

$$p_c(t) = \sin(\frac{\pi t}{T_w}) \cdot \cos(2\pi f_c t) \tag{2.2}$$

$$p_s(t) = \sin(\frac{\pi t}{T_w}) \cdot \sin(2\pi f_c t) \tag{2.3}$$

Table 2.1 – Frequency allocation of different sub-bands

Band Number	Lower Freq (GHz)	Center Freq f_c (GHz)	Upper Freq (GHz)
1	3.308	3.619	3.930
2	3.847	4.158	4.469
3	4.386	4.967	5.008
(skipped)	4.925	5.236	5.547
4	5.464	5.775	6.086
5	6.003	6.314	6.625
6	6.542	6.853	7.164

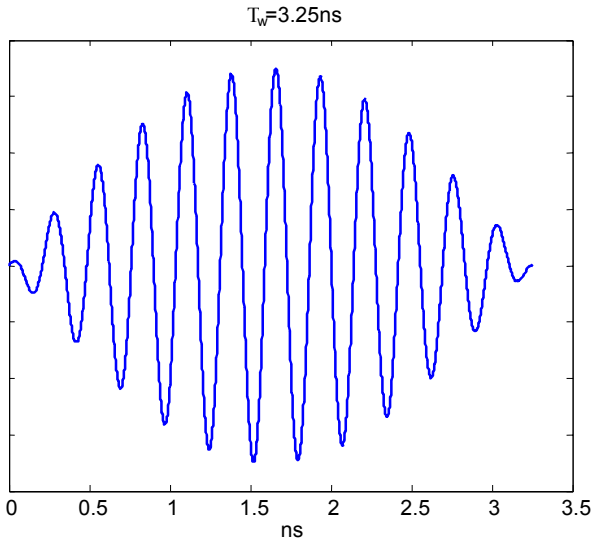

Figure 2.1 – Transmitted pulse shape $p_c(t)$ for band 1

Each band is allocated a certain timeslot that data is sent. At the next time instance, the center frequency is hopped to another band, as shown in Figure 2.2. Information is transmitted across multiple bands resulting in frequency diversity, and this is demonstrated in Chapter 6. This TF hopping scheme allows for multiple-access, with a unique TF sequence assigned to each user. With N_B = 6, there are a total of 720 (=6!) possible time-frequency sequences. The effect of this TF sequence assignment on the BER performance is discussed in Chapter 7.

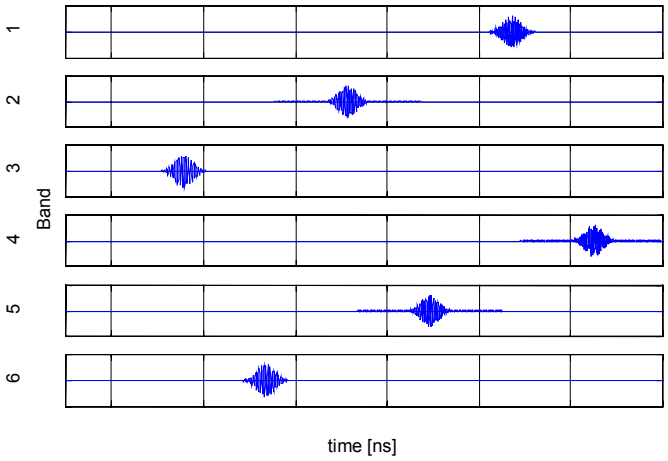

Figure 2.2 – Time-frequency hopping for various bands

From [7], the delay spreads of the various channel models can range from a few tens of the sampling time in CM1 to a few hundreds of sampling time in CM4. The long delay spread contributes to ISI, affecting adversely the BER performance of UWB systems. Denoting PRI by T_s, ISI can be eliminated by having T_s longer than the delay spread, without any additional processes such as equalizer or coding. For example, if the excess delay of a certain channel is 25ns, T_s has to be at least 25ns to eliminate ISI. However, this will also bring down the data rate. In single-band UWB, the data rate D_s is evaluated by

$$D_s = \frac{1}{T_s} \tag{2.4}$$

In the previous hypothetical BPSK system with T_s = 25ns, D_s=40Mbps. With coding, errors introduced by ISI can be reduced but this brings down the overall data rate. The issue of ISI is partially addressed by multi-band UWB, in which a high overall data rate can be achieved with a relatively long PRI on each band. When the conditions are adverse, for example in a NLOS channel, a longer PRI can be chosen so that multipath delays are allowed to "die down" significantly before the next pulse is sent. It has been shown from (2.4) that a long PRI translates to a low data rate, as illustrated in Figure 2.3(a). Nonetheless six bands are available for data transmission in multi-band UWB, an overall high data rate can be achieved, as shown in Figure 2.3(b). This low ISI property is another benefit of multi-band UWB, allowing for a simpler receiver structure and better bit error rate (BER) performance, and this aspect is explored in Chapter 5. The data rate of multi-band UWB D_m can be written as

$$D_m = \frac{N_B}{T_s} \tag{2.5}$$

From (2.5), the data rate can be changed by varying either the N_B or T_s.

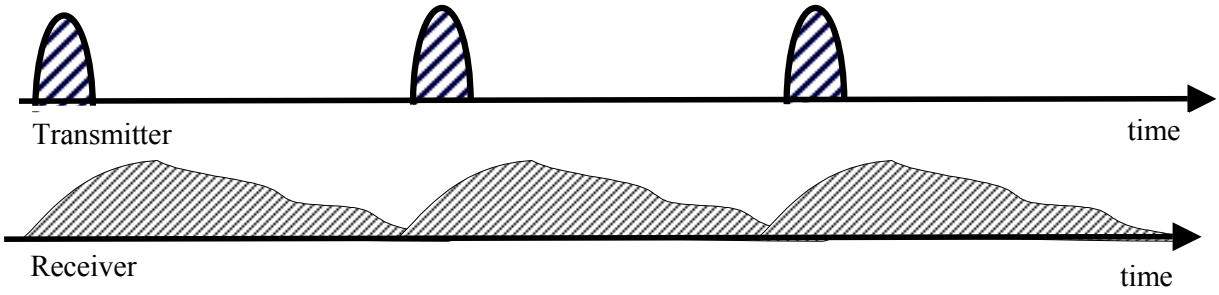

Figure 2.3(a) – Single-band UWB – Low PRI, low data rate

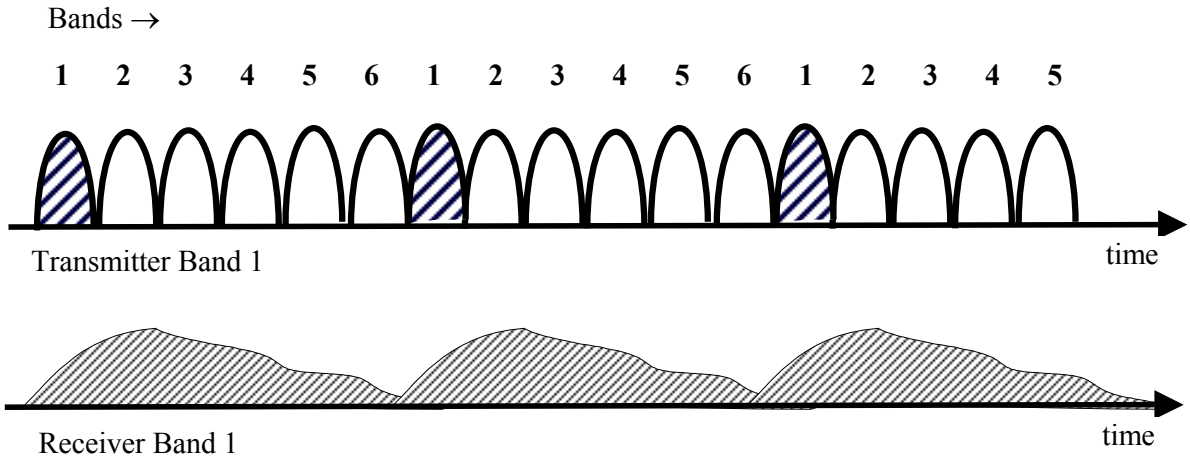

Figure 2.3(b) - Multi-band UWB – Low PRI, high data rate

In this work, 3 modes of data transmission are proposed, to exploit the scalability and adaptivity of multi-band UWB scheme to various design requirements. Each mode has a different PRI and hence different chip rate and ISI immunity. Sampling frequency f_s changes with chip rate, so as to reduce power consumption at lower chip rates. The signal pulse width T_w is set to be at 3.25ns, so that a maximum raw pulse rate of 308Mbps can be attained. The various modes with 4-times over-sampling are illustrated in Figure 2.4. By this 4-times over-sampling, a temporal diversity of order 4 can be achieved. This will be explored with more details in Chapter 5.

The effective pulse width T_w' can be defined as

$$T_w' = \frac{T_s}{N_B} \tag{2.6}$$

The PRI per band, effective pulse width, chip rate and sampling rate for different transmission modes are recorded in Table 2.2.

Table 2.2 – PRI per band, pulse rate and sampling rate for various modes, T_w=3.25ns

Mode	PRI per band T_s	Effective Pulse Width T_w'	Pulse rate D_m	Sampling rate $f_s=4D_m$
A	19.5ns	3.25ns	308 Mpps	1232 MHz
B	39ns	6.50ns	154 Mpps	616 MHz
C	78ns	13.0ns	77 Mpps	308 MHz

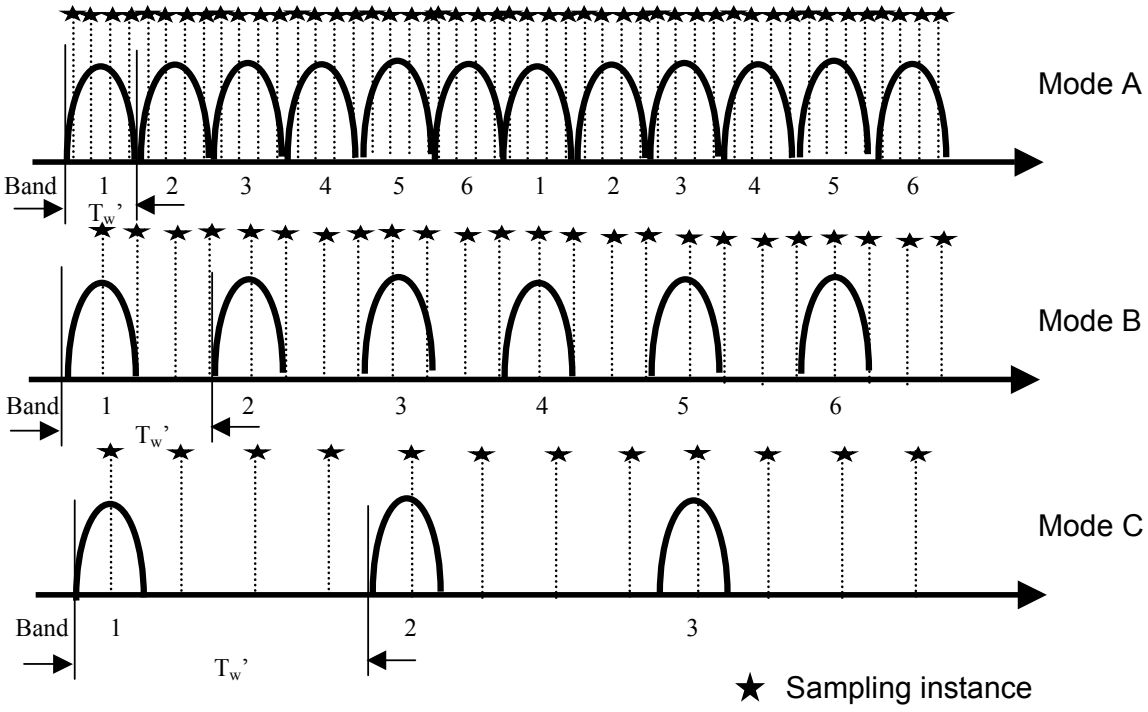

Figure 2.4 - Transmission modes A, B and C

The multi-band scheme also aids in multipath energy collection. For example, the complexity of a RAKE receiver increases with the system bandwidth, and this can become the limiting factor for a single-band UWB [7]. Since a smaller bandwidth is used in multi-band UWB, the RAKE receiver is less complex. More on RAKE reception is presented in Chapter 5.

In summary, the multi-band proposal is:

- Unaffected by narrowband interference such as from 802.11a
- More adaptive and scalable than single-band UWB
- ISI resistant by varying PRI in various transmission modes without lowering data rate
- Better power consumption by varying sampling rates
- Better multiple access capability
- Improved energy collection due to a smaller bandwidth
- Able to support different data rates by either using different number of sub-bands for transmission or by altering the PRI.

All these benefits however, come at a price. The transceivers for multi-band UWB are more complex than single-band ones. For example, acquisition needs to be carried out on every sub-band, because the channel characteristics of every sub-band vary, and this is discussed in Chapter 4. Indeed each sub-band can be considered as a self-contained transceiver pair, an option explored in Chapter 6. This first component of the multi-band receiver chain is the low pass filter, and is presented in the next chapter.

Chapter 3 Joint LPF Design Method for Multi-band UWB

Referring to Figure 1.1, the data pulse of pulse width T_w is up-converted by a local oscillator to the sub-band frequency f_c before transmission. The transmitted pulse $p_c(t)$ after up-conversion is represented by (2.2). After passing through the channel, the received signal is first band-pass filtered and amplified to get rid of out-of-band interference and other radio frequency (RF) artifacts. Then it is down-converted by the receiver LO with an appropriate f_c, and then low pass filtered. Ignoring channel effects and noise, the output signal for the in-phase component $p_c'(t)$ after down-conversion can be written as

$$\begin{aligned} p_c'(t) &= \left[p_c(t) + p_s(t)\right] \cdot \cos(2\pi f_c t + \phi) \\ &= \left[\sin(\frac{\pi t}{T_w}) \cdot \cos(2\pi f_c t) + \sin(\frac{\pi t}{T_w}) \cdot \sin(2\pi f_c t) \right] \cdot \cos(2\pi f_c t + \phi) \\ &= \frac{1}{2}\sin(\frac{\pi t}{T_w})\left[\cos(\phi) + \cos(4\pi f_c t + \phi)\right] + \frac{1}{2}\sin(\frac{\pi t}{T_w})\left[\sin(\phi) + \sin(4\pi f_c t + \phi)\right] \end{aligned} \quad (3.1)$$

where ϕ is the phase difference between the LO and $p_c(t)$. The quadrature component $p_s'(t)$ can be similarly derived as

$$\begin{aligned} p_s'(t) &= \left[p_c(t) + p_s(t)\right] \cdot \sin(2\pi f_c t + \phi) \\ &= \left[\sin(\frac{\pi t}{T_w}) \cdot \cos(2\pi f_c t) + \sin(\frac{\pi t}{T_w}) \cdot \sin(2\pi f_c t) \right] \cdot \sin(2\pi f_c t + \phi) \\ &= \frac{1}{2}\sin(\frac{\pi t}{T_w})\left[\sin(\phi) + \sin(4\pi f_c t + \phi)\right] + \frac{1}{2}\sin(\frac{\pi t}{T_w})\left[\cos(\phi) - \cos(4\pi f_c t + \phi)\right] \end{aligned} \quad (3.2)$$

In both (3.1) and (3.2), the data pulse can be extracted by low-pass filtering to remove the high frequency parts. Another benefit of using a quadrature mixer at the transceiver can be seen when considering $\phi = 90°$, the peaks of the received signal coincide with the zero crossings of the LO. The output signal after down-conversion would be very small if only the in-phase mixer is employed. However, with a quadrature mixer, the

output after the LPF contains both a sin(ϕ) and cos(ϕ) term, so that neither branch will register a small output at any ϕ [14], as shown in (3.1) & (3.2). Hence time drift has become phase drift, and time tracking turns into phase tracking. The upcoming sections deal with the selection of a practical LPF, based on two metrics – energy captured and ratio statistics test (RST). The use of these two criteria for LPF selection was published by the author of this work in [15], however it was based on single-band UWB. With some modifications, it is possible to apply these two criteria for multi-band UWB, with a LPF specification that is suitable for all the 6 sub-bands.

3.1 LPF Design Criteria

To facilitate the design process, 3 well-known filter types are chosen for consideration, namely Butterworth, Chebychev and Elliptic filters. For any of the filter types, 3 parameters are to be determined:

- Normalized passband frequency f_{pass}
- Filter type
- Filter order

These parameters can be determined by the criteria presented below.

3.1.1 Criterion 1 - Energy Captured for Passband of Filter

If (2.2) is rewritten as

$$\begin{aligned} p_c(t) &= \sin(\frac{\pi t}{T_w}) \cdot \cos(2\pi f_c t) \\ &= m(t) \cdot c(t) \end{aligned} \tag{3.3}$$

where m(t) is the data pulse and c(t) is the transmit LO signal. To simplify analysis, ϕ in (3.1) is assumed to be the zero. Considering only additive white gaussian noise (AWGN), the received antenna signal v(t) is

$$v(t) = m(t) \cdot c(t) + n(t) \tag{3.4}$$

where n(t) is AWGN. And the input signal-to-noise ratio SNR_I is

$$SNR_I = \frac{[m(t)c(t)]^2}{N_0/2} \tag{3.5}$$

In (3.5), $N_0/2$ is the noise variance.

The down-converted signal, defined as p_c'(t), is

$$\begin{aligned} p_c'(t) &= [p_c(t) + n(t)] \cdot c(t) \\ &= m(t) \cdot c^2(t) + n(t) \cdot c(t) \end{aligned} \tag{3.6}$$

Using *f*(t) to denote the filter impulse response of the LPF, the signal at the filter output v'(t) is

$$\begin{aligned} v'(t) &= p_c'(t) \otimes f(t) \\ &= \int m(\tau)c^2(\tau)f(t-\tau)d\tau + \int n(\tau)c(\tau)f(t-\tau)d\tau \end{aligned} \tag{3.7}$$

where $\otimes$ denotes convolution.

And the signal-to-noise ratio (SNR_o) of (3.7) is

$$
\begin{aligned}
SNR_o &= \frac{\left[\int m(\tau)c^2(\tau)f(t-\tau)d\tau\right]^2}{E\left[\int n(\tau)c(\tau)f(t-\tau)d\tau\int n(s)c(s)f(t-s)ds\right]} \\
&= \frac{\left[\int m(\tau)c^2(\tau)f(t-\tau)d\tau\right]^2}{\int\int E\left[n(\tau)n(s)\right]c(\tau)f(t-\tau)c(s)f(t-s)d\tau ds} \\
&= \frac{\left[\int m(\tau)c^2(\tau)f(t-\tau)d\tau\right]^2}{\frac{N_0}{2}\int c^2(\tau)f^2(t-\tau)d\tau}
\end{aligned}
\tag{3.8}
$$

There is no way to simplify (3.8) further analytically. By letting $f(t) = \delta(t)$, where $\delta(t)$ is the dirac-delta function, SNR_o can be written as

$$
\begin{aligned}
SNR_o &= \frac{\left[\int m(\tau)c^2(\tau)\delta(t-\tau)d\tau\right]^2}{\frac{N_0}{2}\int c^2(\tau)\delta^2(t-\tau)d\tau} \\
&= \frac{\left[m(t)c^2(t)\right]^2}{\frac{N_0}{2}\left[c^2(t)\right]} \\
&= \frac{\left[m(t)c(t)\right]^2}{N_0/2} \\
&= SNR_I
\end{aligned}
\tag{3.9}
$$

Equation (3.9) shows that it is possible for the output SNR to be equal to the input SNR, a similar conclusion given in [16], when match filtering is used. Nevertheless a filter of impulse response $f(t) = \delta(t)$ is unrealizable, and it is necessary to turn to other techniques to obtain a practical LPF. In terms of hardware implementation in high frequency, it is easier to use well-known LPF designs. The performance of Butterworth, Chebychev and Elliptic filters for the proposed receiver structure was investigated by simulation studies, as presented in Section 3.2.

Comparison among the different filter designs is based on the energy captured, which is defined as

$$\begin{aligned}
&\text{Energy Captured (\%)} \\
&= \frac{\text{Energy received}}{\text{Energy transmitted}} \\
&= \frac{\left\|(\text{received pulse} \cdot \text{LO}) \otimes \text{LPF}\right\|^2}{\left\|(\text{received pulse} \cdot \text{LO})\right\|^2} \\
&= \frac{\left\|\left[p_c(t) \cdot c(t)\right] \otimes h(t)\right\|^2}{\left\|p_c(t) \cdot c(t)\right\|^2}
\end{aligned} \tag{3.10}$$

where $\|\cdot\|$ denotes the norm operation. Equation (3.10) is the ratio of the energy retained after low-pass filtering, without taking channel conditions into account. A good filter design is one with high energy captured, without the need of a large passband. In addition, the filter order should be low to reduce complexity and settling time; the trade-off is that a low order filter has a slower roll-off. The LPF also needs to be realizable at all bands. A filter that works well at band 1 for example, may have a passband that is capturing too little energy for band 6. These considerations are discussed in Section 3.2.1, through simulations of different passband frequencies.

3.1.2 Criterion 2 - Ratio Statistics Test for Type and Order of Filter

Besides energy captured, another important parameter that influences the LPF design is the auto-correlation of the output samples. After the transmitted signals have propagated through the channel and processed by the receiver, these output samples should be of low correlation. This is to ensure that the implicit diversity caused by multipath effects can be exploited, a property used in the over-sampling equalizer in Chapter 5. Two filters of different orders may capture the same amount of energy with the same passband, but the one with better correlation properties is chosen for implementation.

The length of the correlation window N_w influences the number of sampling instances within it. It can be seen from Figure 3.1 more sampling instances are contained in a large correlation window. A correlation window of length N_w corresponds to N_w possible sampling instances.

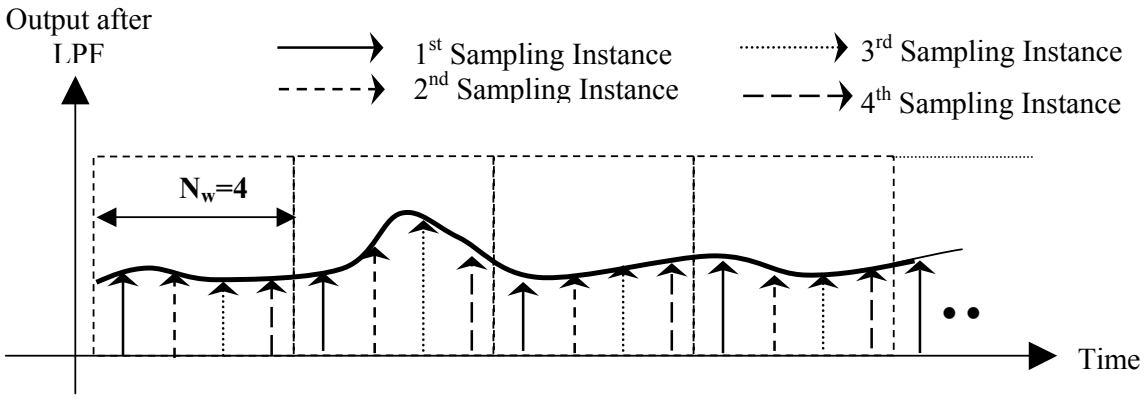

Figure 3.1 – Correlation window and sampling instance

For each possible sampling instance, its auto-correlation is computed, resulting in N_w auto-correlation curves, as illustrated in Figure 3.2.

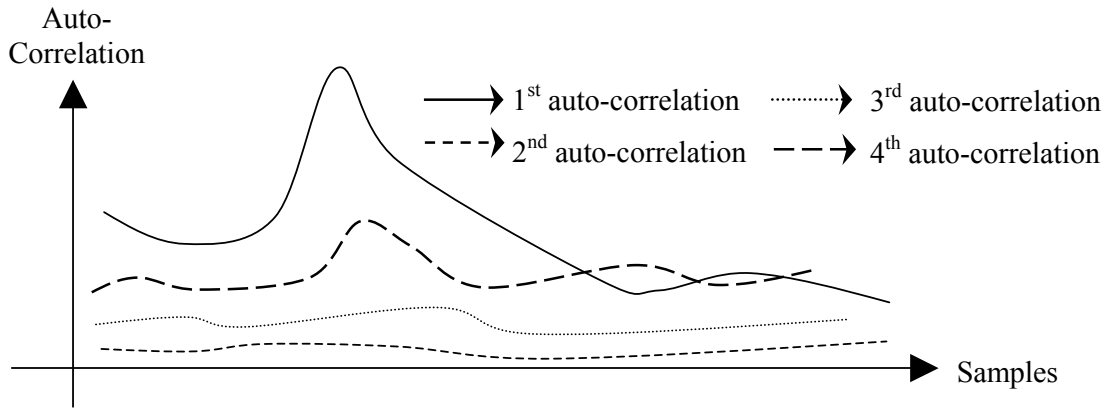

Figure 3.2 – Auto-correlation curves with N_w=4

Similar to filter order, an N_w with lowly correlated samples is favorable. Correlation properties are compared using a measure called ratio statistics test (RST) [17].

$$RST = \frac{Maximum\ Correlation\ Values}{2nd\ Maximum\ Correlation\ Values} \tag{3.11}$$

Graphically, RST can be visualized as the point-by-point division of the top most auto-correlation curve with the second top most auto-correlation curve. For Figure 3.2, RST is calculated by the point-to-point division of the 1st auto-correlation curve to the 4th one; the output of RST is also a curve. A system with good correlation properties should have a high average RST value. This means that the maximum correlation is many times greater than the second maximum correlation, therefore the samples are almost uncorrelated. The LPF specifications can now be determined using energy captured and RST.

3.2 Simulation Results & Discussion for LPF Specifications

The selection of LPF specifications based on energy captured and RST was extensively simulated for a multi-band UWB system. Only odd-order filters, from 3rd to 9th orders, were simulated for energy captured comparison. Odd orders were used to avoid the possible impedance mismatch issues involved in the practical implementation of Chebychev filters. The passband and stopband attenuations for the filters, where applicable, are recorded in Table 3.1.

Table 3.1 – Passband and stopband attenuations used in the simulations

	Passband Attenuation(dB)	Stopband Attenuation(dB)
Butterworth	-	-
Chebychev	0.3	-
Elliptic	0.3	80

3.2.1 Passband Determined by Energy Captured

As mentioned in 3.1.1, the metric of energy capture only considers the energy retained after low-pass filtering, and ignores channel effects such as multipath and noise. The passband frequency f_{pass} was normalized to the sampling frequency. The aim of this exercise was to specify a f_{pass} that have a high energy captured for all sub-bands.

The results for odd orders Butterworth, Chebychev and Elliptic filters for band 1 are shown in Figure 3.3.

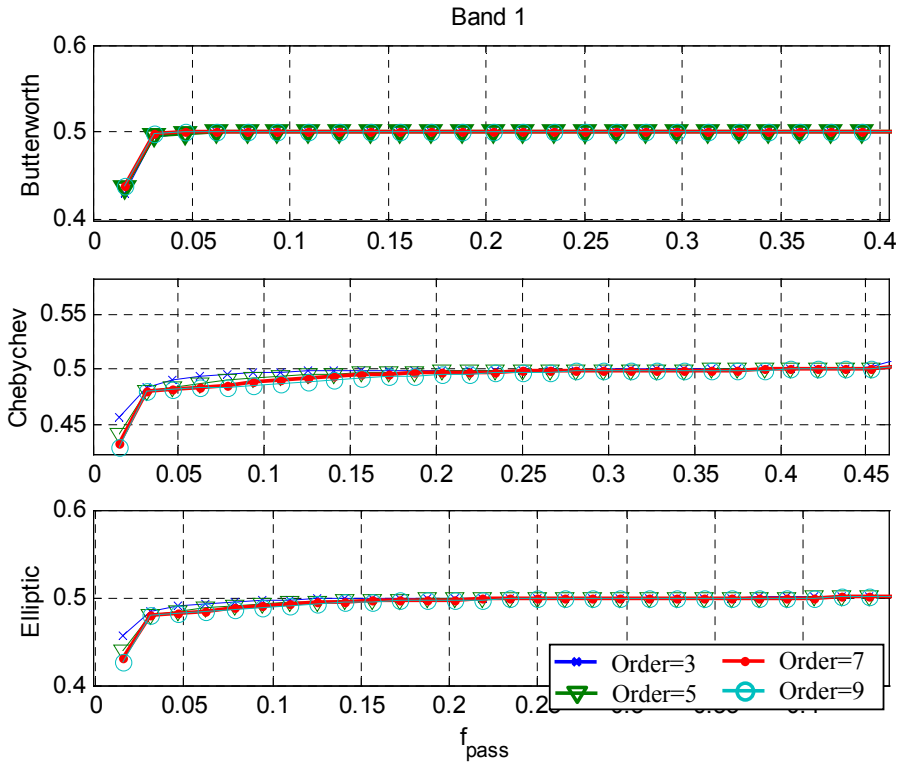

Figure 3.3 – Energy captured for Band 1

It could be seen from Figure 3.3 that the passband frequencies leveled off at 50% energy captured. This observation could be explained from a quick inspection of (3.2),

that the other 50% of the higher frequency energy was filtered off. For Band 1, the minimum normalized passband frequency to achieve an energy captured of 50% was at f_{pass} = 0.05, regardless of the filter order. The procedure was repeated in Band 6, and the results are shown in Figure 3.4.

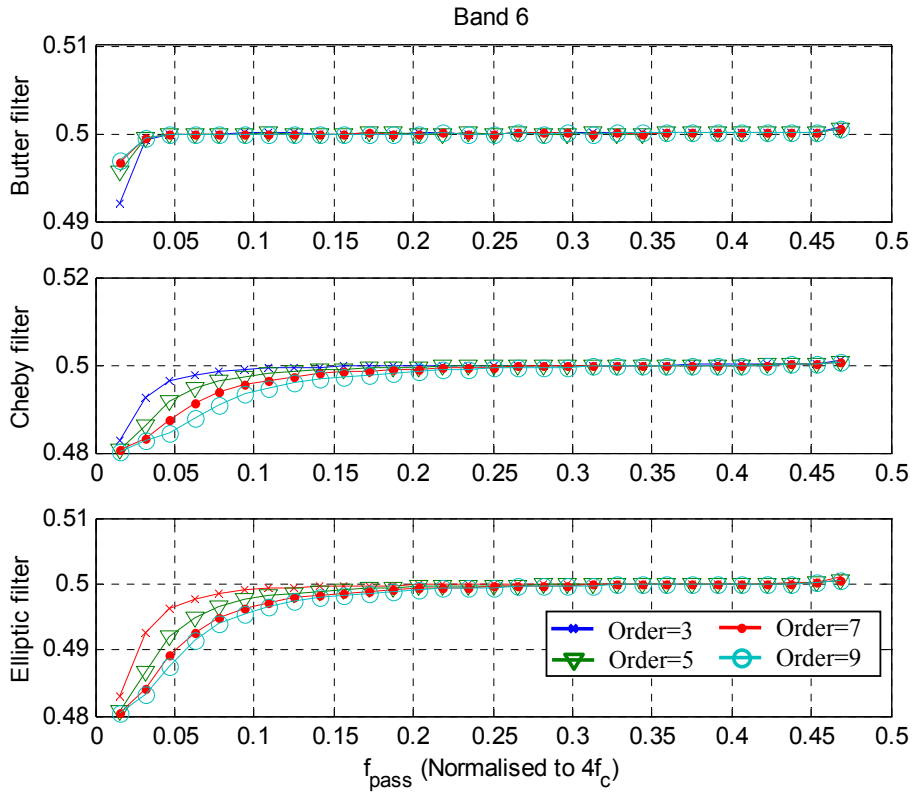

Figure 3.4 – Energy captured for Band 6

Although the same leveling off at 50% could be seen for Band 6, the energy captured by a lower order filter was observed to be superior to a higher order one. This was especially evident from the curves of Chebychev and Elliptic filters. At f_{pass} = 0.1, energy captured started to peak at 50% for filter orders 3 and 5. At orders 7 and 9, the f_{pass} = 0.15 was needed for 50% energy captured.

The rest of the bands showed similar trends, and their minimum passband frequencies for 50% energy captured were between f_{pass} = 0.05 and f_{pass} = 0.15 for each band. Therefore the energy captured of other bands are not reproduced here.

From the simulation of all 6 bands, it was possible to conclude from the energy captured criterion that an f_{pass} = 0.10 was good for filter orders 3 and 5, when an f_{pass} = 0.15 was needed for orders 7 and 9. It should be noted that a larger f_{pass} could be less desirable as it might admit more unwanted signals to the next stage of the receiver. With the choice f_{pass} resolved, the determination of filter type and order was carried out next.

3.2.2 Filter Type and Order by Ratio Statistics Test

For RST, the correlation properties of the received signals were tested in a Channel Model 1 environment, in the presence of a 10dB AWGN. The received signals were down-converted and low pass filtered, using the f_{pass} results from Section 3.2.1. For filter orders 3 and 5, f_{pass} = 0.10 and for orders 7 and 9, f_{pass} = 0.15. Two LPFs were chosen for comparison, one of higher order (9th order) and another of lower order (3rd order). These two extreme orders were chosen so that the difference in results would be more pronounced. Other parameters of the different filters were the same as that recorded in Table 3.1.

There were four permutations of parameters for RST to be carried out for each filter type. They were 3rd order filter with short N_w, 3rd order with long N_w, 9th order filter with short N_w and 9th order filter with long N_w. The size of the correlation window N_w for each of the filters was recorded in Table 3.2, in which the values for N_w were chosen arbitrarily.

Table 3.2 – Size of N_w for different filter types

	Short N_w	Long N_w
Butterworth	35	50
Chebychev	48	100
Elliptic	48	130

The RST values from the output of the LPF were then calculated, and this process was repeated for 100 different channels. Comparison was based on the average of 100 RSTs. The RST results of the three filters, operating in Band 1 and Band 6, are shown in Figure 3.5 and Figure 3.6 respectively.

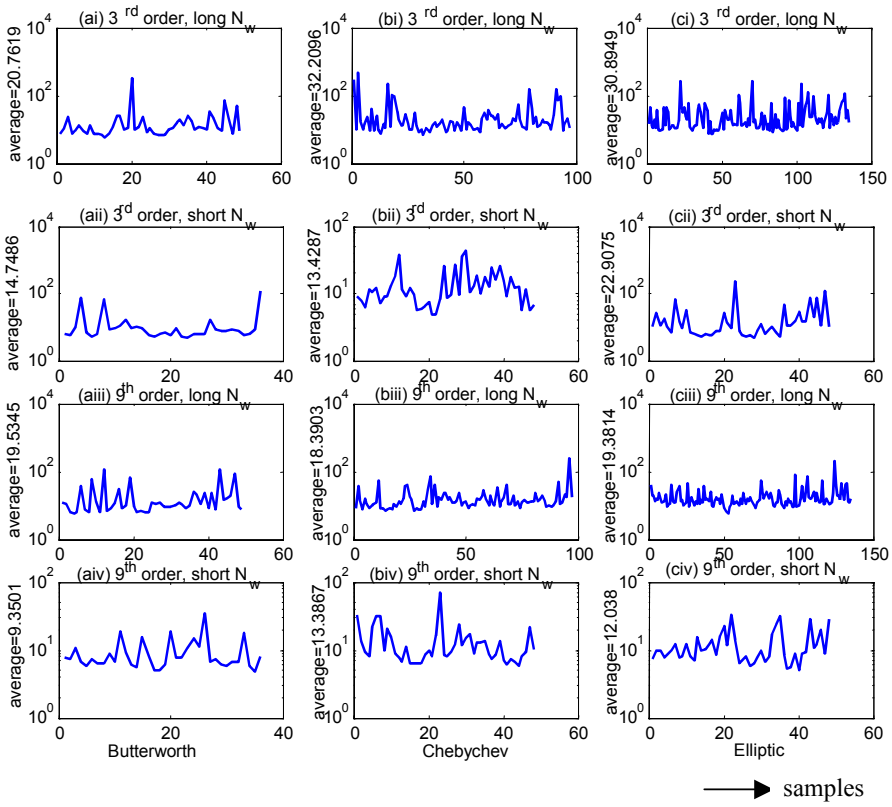

Figure 3.5 – RST for Band 1

From the figure above, a long N_w gave higher average RST value than a short N_w most of the time. Figure 3.5 also showed that 3rd order filters had superior correlation properties than 9th order filters. Take for instance the average in Figure 3.5(bii) (3rd order) against that of Figure 3.5 (biv) (9th order).

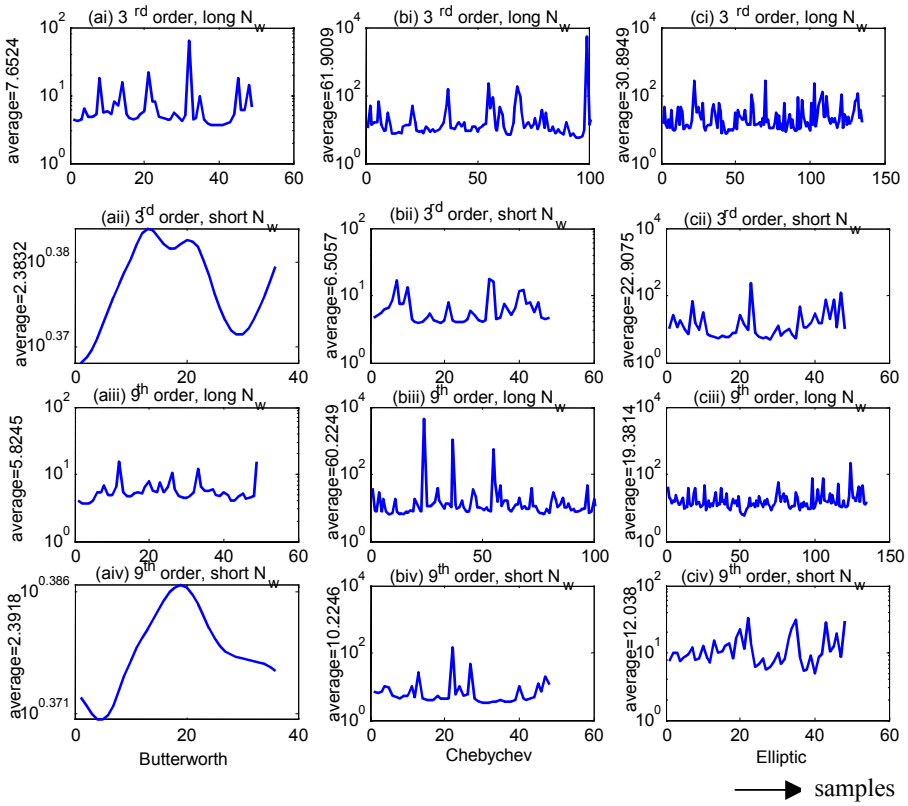

Figure 3.6 – RST for Band 6

Similar interpretation could be made on Figure 3.6. A long N_w again had a higher average RST than a short N_w. This was because samples drawn from long N_w were spaced further from each other, hence less likely to be correlated. Conversely a short N_w meant the samples were drawn at a shorter interval, and more correlated. This provided the vindication for the use of RST to measure correlation properties.

Again, 3rd order filter showed better correlation properties than 9th order ones, if the same N_w was used. They also required a smaller f_{pass}, making them more favorable than 9th order filters. Chebychev and Elliptic filters had better RST performance than Butterworth filter. Between Chebychev and Elliptic filters, Chebychev filters performed slightly better. Besides having slightly better correlation properties, Chebychev filters were simpler to realize than Elliptic filters too.

3.3 Conclusion for Filter Selection

In summary, a Chebychev 3rd order filter with f_{pass} = 0.10 was found to be suitable as the LPF for multi-band UWB receiver. This configuration had a good energy captured percentage with a relatively small f_{pass}, showed good correlation properties and was fairly simple to implement.

With this it is possible to move to the next block of the multi-band receiver - acquisition.

Chapter 4 Acquisition

After down-conversion of the received multi-band UWB signals, timing information needs to be acquired. Accurate acquisition is necessary for all baseband processes at later stages, and fast acquisition is critical for high data rate systems such as UWB. With the same packet size, the overheads involved in acquisition become more accentuated as data rate increases [10]. In the literature so far, attempts to investigate acquisition issues are limited to singleband UWB systems. For example in [18], an efficient linear search algorithm is proposed for a single-band UWB channel with dense multipath. In [19], a non-consecutive search acquisition analysis based on time-hopping spread spectrum UWB is presented. In [20], a rapid UWB acquisition scheme based on Kasami code is proposed.

For the acquisition of multi-band UWB systems, certain properties of a practical UWB channel are exploited and presented in this chapter. The results has also been published in [21].

Timing information is usually transmitted in preambles, added before UWB data blocks before transmission, as shown in Figure 1.1(a). Timing information is acquired by a slide-correlator at the receiver, in which the known preambles and the received signal are correlated at all possible time delays. The periodic auto-correlation of the preamble sequence is therefore vital for the operation of the slide correlator. The length of the preamble sequences is another important design consideration. The preamble chosen should be short to reduce overhead, since it carries no data. However, a shorter sequence has a lower correlation peak, making it susceptible to acquisition

errors with noise and multipath effects. These errors are costly. If acquisition does not occur at the maximum of the received signal, the received SNR may be adversely affected, degrading the bit error rate (BER) performance of the system.

The low ISI property of multi-band UWB is helpful to acquisition, because preambles are often not protected by coding or equalization. Multipath reflections are allowed to subside, so that the slide-correlator is able to detect a signal peak without any influence form the previous signal.

The choice of preambles and the proposed acquisition scheme are discussed more in details in upcoming sections.

4.1 Preamble Sequences in Multi-band UWB

From [21], the periodic auto-correlation R(m) of a preamble sequence q_n of length N_q is defined as

$$R(m) = \sum_{n=0}^{N_q-1} q_n^* \cdot q_{n+m} \tag{4.1}$$

in which q_n refers to the n^{th} element of the sequence, and $q_{Nq+n} = q_n$. A sequence is said to have good auto-correlation properties if it has high correlation peak at m = 0 and low correlation at other values of m. The low correlation ensures an easily detectable peak at the receiver output with zero delay.

Two popular preamble sequences were chosen as possible candidates for multi-band acquisition scheme, namely constant amplitude zero auto-correlation (CAZAC) and Barker sequences, chosen to show the performance difference between long and short codes respectively. Both codes display favorable properties that are provided in the next section.

4.1.1 Properties of Barker Sequences

Preamble are usually taken from root-of-unity sequences, whose elements are all complex roots of unity in the form of exp(j2πx), with x a rational number as defined in [23]. From [24], a binary Barker sequence, limited to [-1,1] is defined as

$$R(m) = \begin{cases} \sum_{n=0}^{N_q-1} k_n^* \cdot k_n , & m = 0 \\ \leq 1 , & otherwise \end{cases} \tag{4.2}$$

where k_n is the n^{th} component of the Barker code. Binary barker codes are short sequences that only exist for N_q = 2, 3, 4, 5, 7, 11 and 13, as shown in [25]. For this work, a Barker sequence of length-4 was chosen. It is written as K_4, and its constituents are recorded in (4.3), and its autocorrelation is shown in Figure 4.1.

$$\begin{aligned} K_4 &= \{k_0, k_1, k_2, k_3\} \\ k_0 &= k_1 = k_2 = 1, \quad k_3 = -1 \end{aligned} \tag{4.3}$$

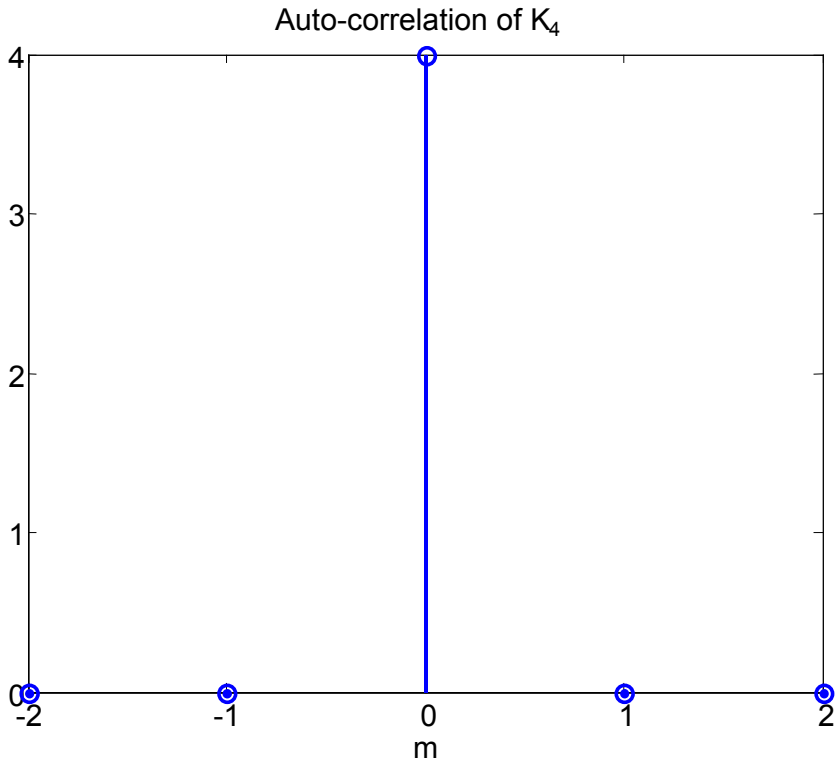

Figure 4.1 - Autocorrelation of one length-4 Barker sequence (K_4)

At the beginning of this chapter the interplay between the preamble length and acquisition time has been briefly described. If only one length-4 Barker code is used as the preamble, the peak at the slide-correlator is likely to be overwhelmed by additive noise and multipath effects, causing acquisition errors. To increase the peak correlation, N Barker sequences are repeated, denoted by K_4^N. Figure 4.2 shows the autocorrelation 10 Barker sequences K_4 at different time delays.

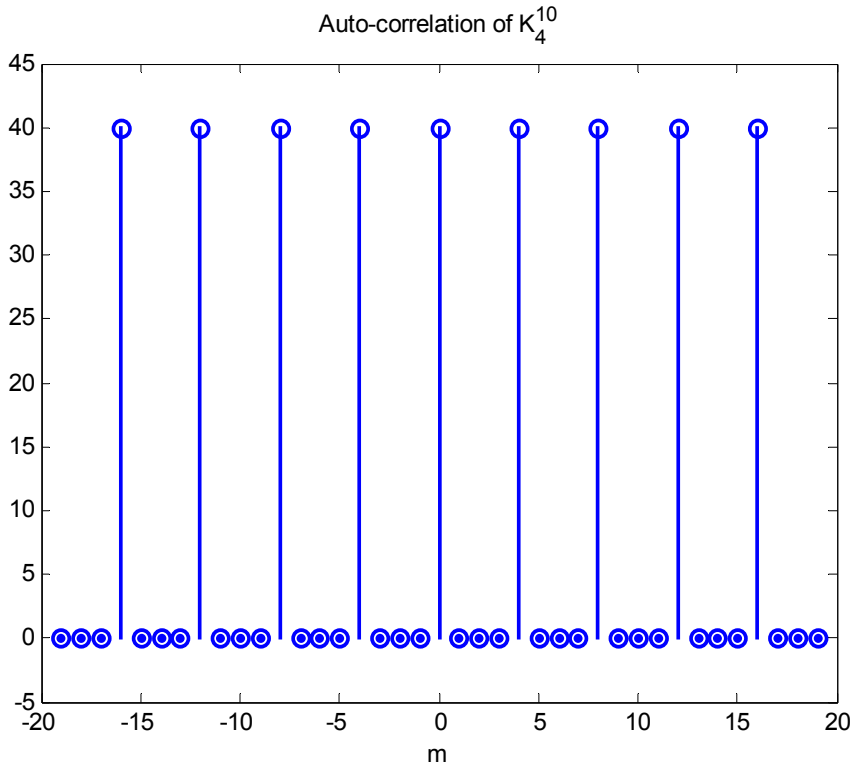

Figure 4.2 - Autocorrelation of ten length-4 Barker sequences (K_4^{10})

As shown in Figure 4.2, the maximum correlation is increased ten-fold to 40. Another important observation is that the correlation peaks occur in regular intervals, not only at zero time delay. This translates to faster acquisition, as the correlator does not have to sweep through the whole uncertainty region. Once a correlation peak is detected, the actual signal maximum is within a few length-4 symbols. This property is especially

important for UWB, in which the first signal peak in non line-of-sight channels may have delays equivalent to several Barker symbols.

In order to enhance piconet isolation and increase multipath resistance, the preamble sequences are applied on a per band basis. Each band is assigned a rotated version of the acquisition sequence, according to the TF code. A possible implementation using length-4 Barker code is shown in Figure 4.3.

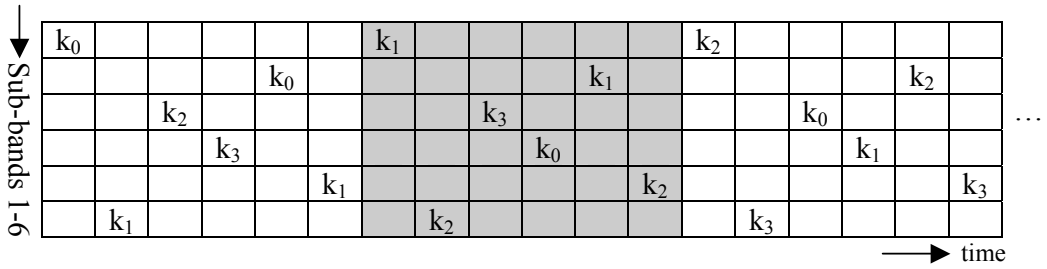

Figure 4.3 - Barker code assignment for each sub-band

Referring to Figure 4.3, since there are 6 sub-bands and 4 possible Barker phases, the sub-band assignment pattern repeats itself after 24 chips. These 24 chips constitute a zero-inserted Barker symbol K_{4x6}. The autocorrelation properties of this zero-inserted Barker code is similar to that shown in Figure 4.2, except that the peaks occurs at every 24 chips, which corresponds to the symbol period of K_{4x6}. Due to the short length of the Barker code used, the starting phase of some sub-bands are repeated. A series of N zero-inserted Barker-4 symbol, with a starting phase of k_p, is denoted by the symbol ${}_pK_{4x6}^{N}$. For example sub-bands 1 and 2 both use the Barker sequence ${}_0K_{4x6}^{10}$, with their start positions are separated in time by a few chips.

4.1.2 Properties of CAZAC Sequences

If a root-of-unity sequence has an out-of-phase periodic auto-correlation of zero, as in (4.4), this is known as constant amplitude zero auto-correlation (CAZAC) sequence,

$$R(m) = \begin{cases} \sum_{n=1}^{N_q-1} c_n^* \cdot c_n , & m = 0 \\ 0 , & otherwise \end{cases} \tag{4.4}$$

where c_n refers to the n^{th} element of the CAZAC sequence. A length-16 CAZAC sequence C_{16} was chosen to contrast the acquisition performance from K_4. The mathematical representation of C_{16} is

$$\begin{aligned} c_{4k+l} &= j^{k \cdot l}, \quad j = \sqrt{-1}, \quad k = 0,1,2,3, \quad l = 0,1,2,3 \\ C_{16} &= \{1,1,1,1,1, j, -1, -j, 1, -1, 1, -1, 1, -j, -1, j\} \end{aligned} \tag{4.5}$$

The 4-phase CAZAC sequence in (4.5) can be converted into QPSK by a 45° phase rotation. The auto-correlation is shown in Figure 4.4

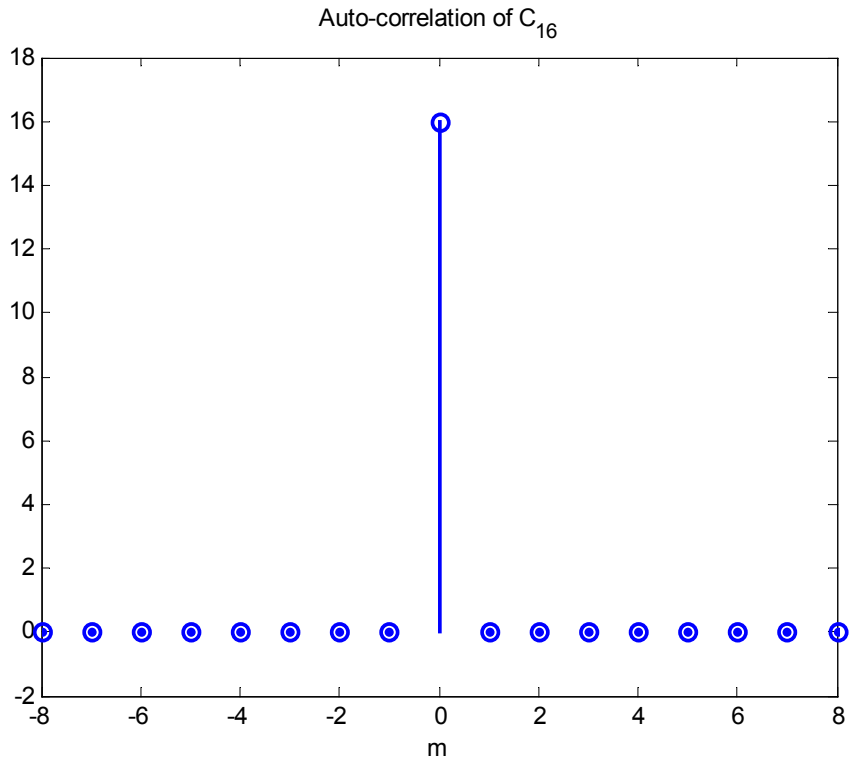

Figure 4.4 - Autocorrelation of one length-16 CAZAC sequence (C_{16})

Being a longer symbol, its maximum correlation value is 16 and only two CAZAC symbols C_{16}^2 as preambles are needed for a substantial peak to be detected at the slide correlator, as shown in Figure 4.5. Signal peaks occur less frequently than that in Figure 4.4, and therefore a longer acquisition time is needed before a peak is detected.

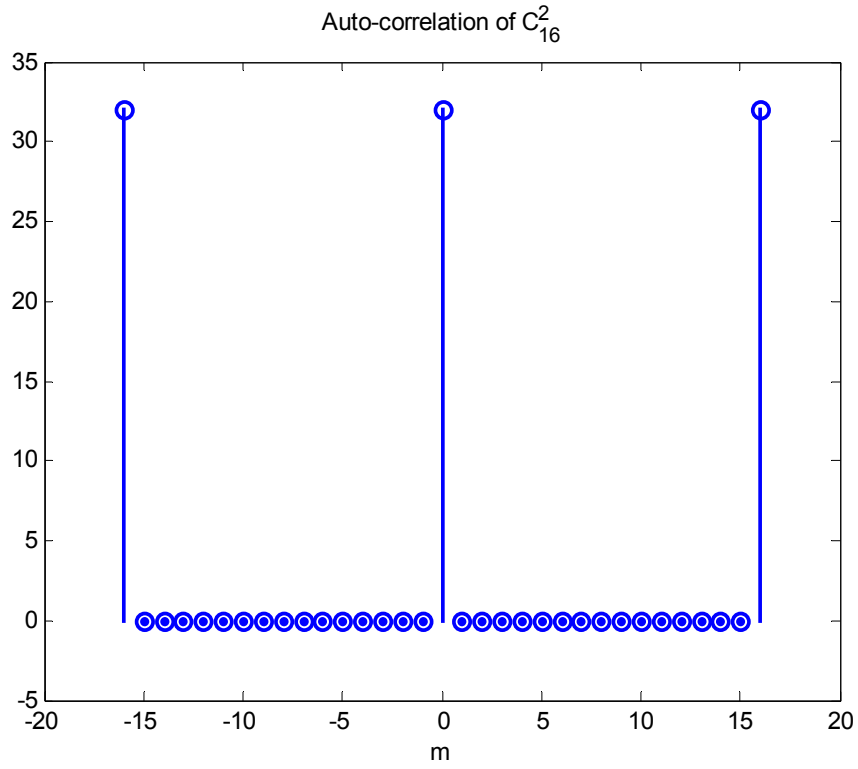

Figure 4.5 - Autocorrelation of two length-16 CAZAC sequences (C_{16}^2)

A possible sub-band allocation for a zero-inserted C_{16x6}^2 preamble can be found in Figure 4.6. The starting phase ${}_pC_{16x6}^2$ is not repeated in any sub-band.

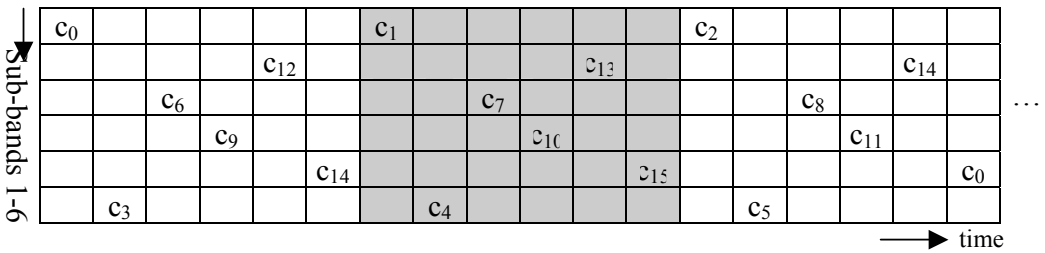

Figure 4.6 - CAZAC code assignment for each sub-band

4.2 System Model of the Proposed Acquisition Scheme

4.2.1 Parallel Search Correlators

In acquisition, both phase and time uncertainties need to be resolved. Conventionally, the phase is fixed at the slide-correlator, so that only time uncertainty needs to be determined by searching serially through all possible time delay locations. By fixing a certain phase at the correlator, the time uncertainty T_u for a slide-correlator is given by

$$T_u = N_B \times N_q \tag{4.6}$$

In (4.6), it has been assumed that channel delay occurs in multiples of chip duration T_w. Any channel delay beyond T_u chips is taken care of by the next preamble symbol, as explained in Section 4.1.1. The T_u for the two preamble candidates chosen in this study is recorded in Table 4.1.

Table 4.1 – Time uncertainty T_u for K_{4x6}^{10} and C_{16x6}^{2}

	K_{4x6}^{10}	C_{16x6}^{2}
T_u	24	96

A parallel search reduces acquisition time by correlating more than one phase at each instance. For example 4 slide-correlators can be used for a K_{4x6}^{10} system in parallel, one for each starting phase of k_p. Each correlator needs to perform 6 correlations to ascertain the timing uncertainty. This is because any time delay beyond 6 chip locations has a strong correlation with an adjacent phase. Figure 4.7 shows an example of this behavior. The transmitter sends the ${}_1K_{4x6}^{10}$ preamble, but due to channel delay it has a strong correlation with ${}_0K_{4x6}^{10}$.

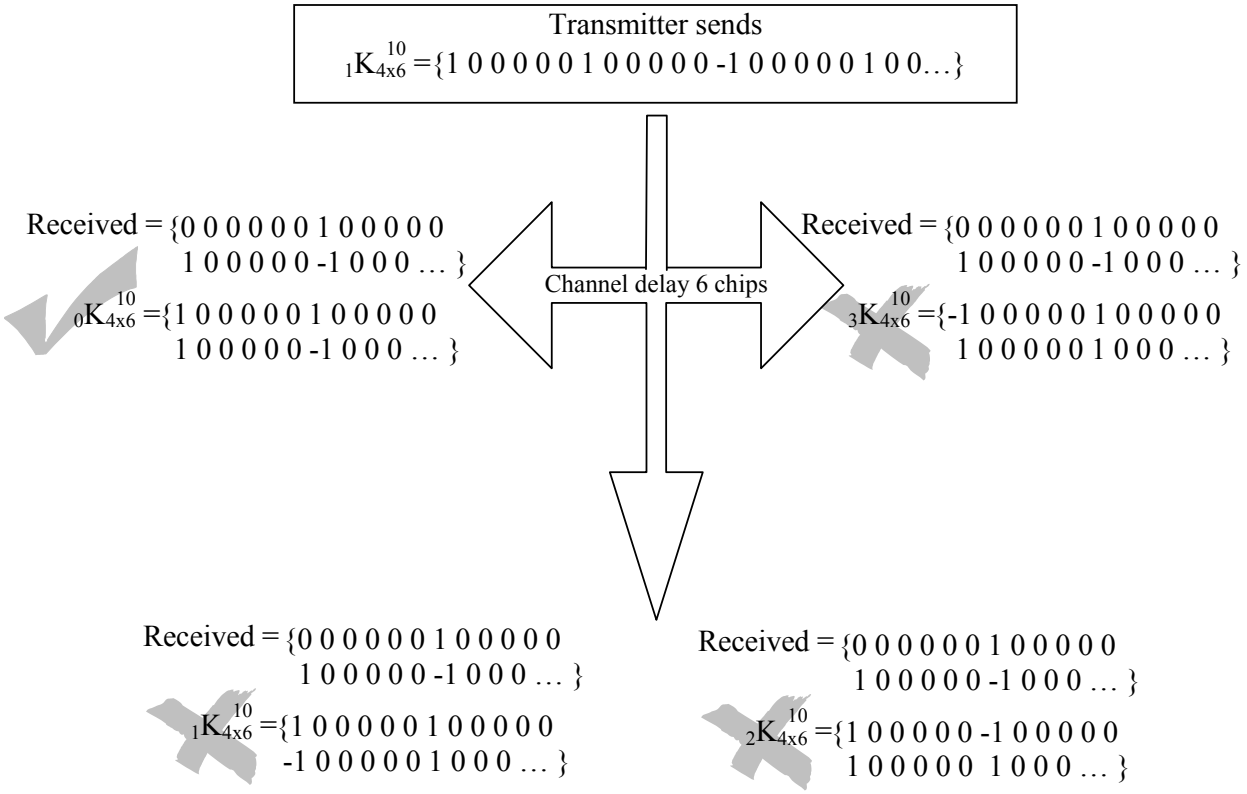

Figure 4.7 - Strong correlation with an adjacent phase by parallel correlators

4.2.2 Double Dwell Detection

Besides using parallel correlators, double-dwell structure is used to decrease the probability of miss P_m and probability of false detection P_{fa}. The first stage performs a half-length correlation, using K_{4x6}^{5} or C_{16x6}^{1} as appropriate. The first stage is to have a low P_m in the expense of a high P_{fa}. If the correlation value is above a certain threshold, the second stage of a full-length correlation is entered, with K_{4x6}^{10} or C_{16x6}^{2} as required. The purpose of the second stage is to minimize P_{fa}.

If the threshold values are too low, the true correlation peak may be missed as acquisition is declared too early, affecting the SNR. On the contrary, a threshold level too high increases acquisition time, as more correlation operations are needed before the threshold is exceeded.

In order to appreciate of the maximum correlation obtained from a conventional slide-correlator, serial slide-correlation is performed at the receiver and the cumulative frequency of the maximum half- and full-length correlation value is recorded. The curves for Barker and CAZAC sequences in various channel conditions are shown in Figure 4.8 & Figure 4.9.

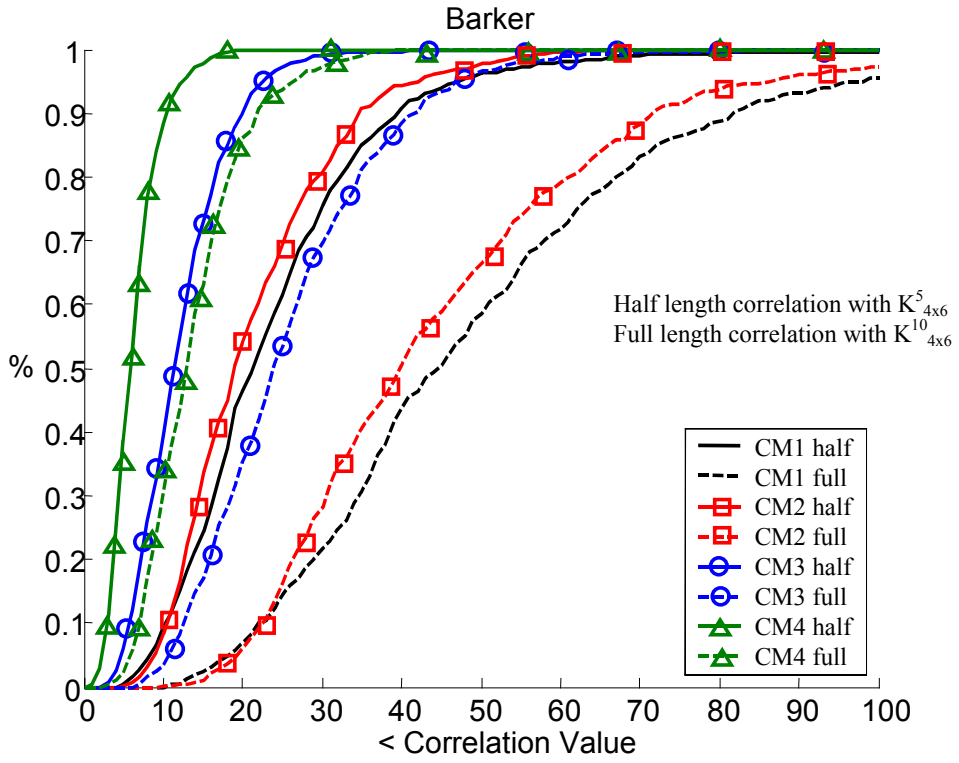

Figure 4.8 – Cumulative frequency of maximum half- and full-length correlation, for Barker code in various CMs

From the above figure, it can be observed that the maximum correlation values vary a great deal under practical UWB channels. Take the correlation values for Barker code in CM1 environment in Figure 4.8 for example; its maximum half-length correlation ranges from 4 to 80. To minimize P_m, the threshold for this stage should be held at 4. However this threshold value causes the second stage to be entered too frequently, increasing acquisition time. As a result, a threshold that depends on the channel conditions, as obtained from the first half-length correlation, is used as the first stage threshold. By making the first stage threshold to depend on the channel, the second stage will not be activated too frequently while keeping P_m low.

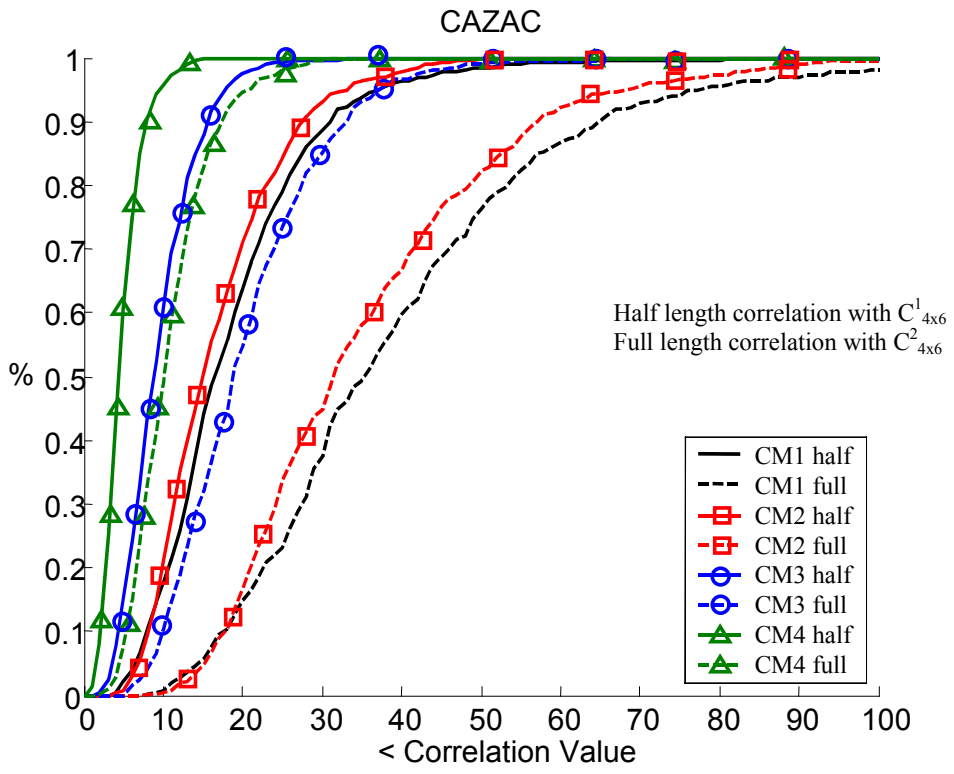

Figure 4.9 – Cumulative frequency of maximum half- and full-length correlation, for CAZAC code in various CMs

For the second stage of detection, the threshold consists of a variable and a fixed component. The fixed threshold is determined based on Figure 4.8 & Figure 4.9. If the fixed threshold is set at 60th percentile for a C^{2}_{16x6} system (a correlation value of 40 in CM1), 60% of the maximum correlation lies below it. The variable component, which again depends on the channel conditions, caters for the 40% that lies above it. Both the thresholds must be exceeded for the declaration of acquisition. If not, the maximum correlation value is chosen, which is also the value of the variable threshold. Figure 4.11 shows the details for the initialization of the two variable thresholds.

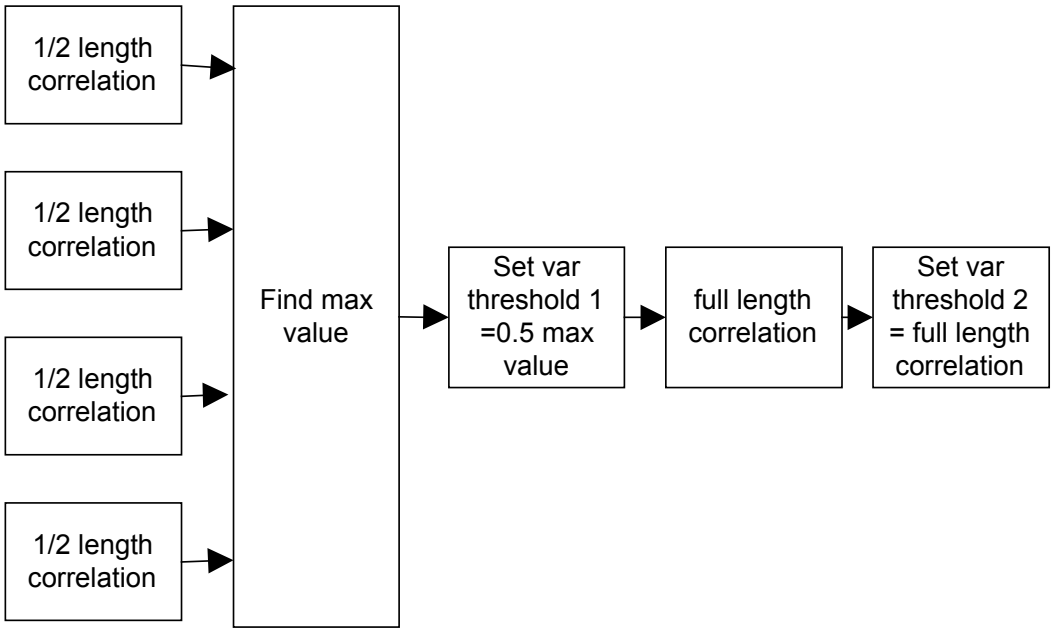

Figure 4.10 - Initialization of the variable thresholds

4.2.3 Phase Elimination

The methods described in Sections 4.2.1 and 4.2.2 are commonly used acquisition techniques. In this section, a method unique to multi-band UWB is introduced, called phase elimination, which is the most unique feature of the proposed scheme.

In either Figure 4.3 or Figure 4.6, it is interesting to note that once the phase sequence of any sub-band is determined, the phase and time of the sequence on other sub-bands can be predicted. If every sub-band suffers the same channel effects, this inherent coding property allows acquisition to be done only on one band, as the rest can be deduced. However, the practical situation is far from ideal. Every sub-band suffers different channel conditions. The preamble pattern will not be completely deterministic, due to the different channel delay at each sub-band. Through simulations using different channel models, it was found that certain relationship still exists between the phase of the present sub-band with the previous one, in such a way that one of the four test phases can be eliminated. This is summarized in Table 4.2.

Table 4.2 – Relationship between phases of the previous and the present sub-bands

Phase in Previous Sub-band	Phases to Test for Present Sub-band
0	0, 1, 2
1	1, 2, 3
2	2, 3, 0
3	3, 0, 1
No results available	0, 1, 2, 3

Since phase elimination depends on the results of the previous acquisition, errors may propagate. Therefore the correct acquisition of the first sub-band is crucial, and every phase is tested as shown in the last row of Table 4.2. Figure 4.11 shows the system model of the proposed scheme.

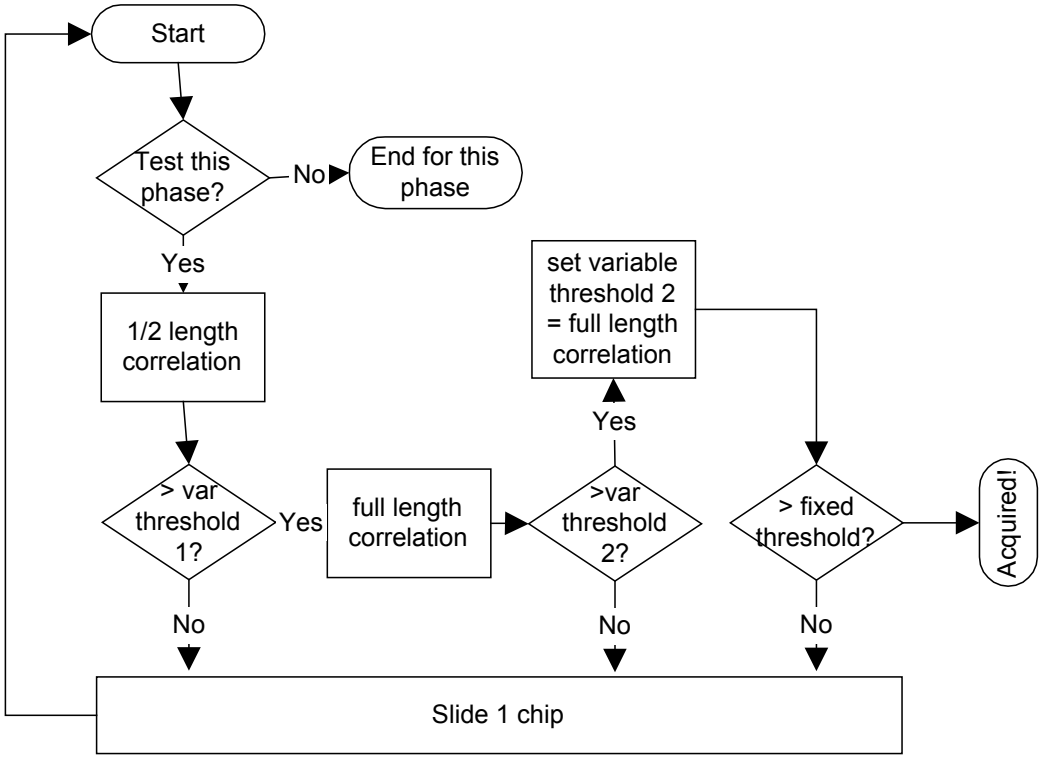

Figure 4.11 – Acquisition block diagram at one of the sub-bands for a particular phase

4.3 Simulation Results and Discussions for Acquisition

The proposed system was simulated with 100 multi-band channels with various SNR. Parameters investigated were P_{fa} and correlation count ratio, plotted with different full-length threshold percentile value obtained from Figure 4.8 & Figure 4.9. Without any loss of generality, only Mode A of CM1 has been simulated.

The acquired phase and correlation magnitude of the proposed system operating in a noisy environment was compared with an exhaustive serial search correlator in a noiseless environment. A false alarm was declared if:

- The acquired phase p_{noisy} by the proposed system was different from the phase of a noiseless system $p_{noiseless}$.
- The acquired correlation magnitude M_{noisy} was more than 3dB below the noiseless maximum magnitude $M_{noiseless}$.

Correlation count on the other hand was the ratio between the total number of half-length correlation operations needed by the proposed scheme to that of an exhaustive serial search. For an exhaustive full-length correlation search, the total number of half-length correlations C was

$$C = 2 \times T_u \times N_B \times \#channels \tag{4.7}$$

Correlation count showed if the number of computations needed for acquisition was reduced using the proposed scheme. Low correlation count meant a faster acquisition, but at the same time it should not sacrifice in P_{fa} performance.

4.3.1 Probability of False Alarm and Correlation Count of Barker Code

Figure 4.12 shows the performance of Barker preamble K_{4x6}^{10}, averaged over 100 CM1 channels, with its correlation count shown in Figure 4.13. The full-length threshold percentile values were obtained from Figure 4.8.

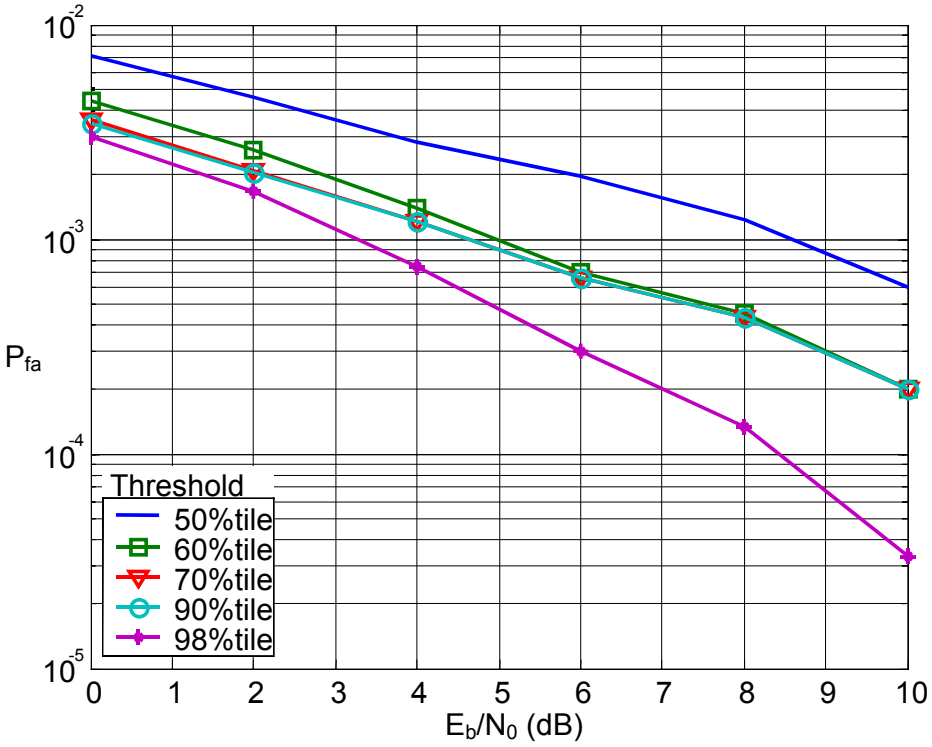

Figure 4.12 - P_{fa} performance of K_{4x6}^{10} Sequence in CM1

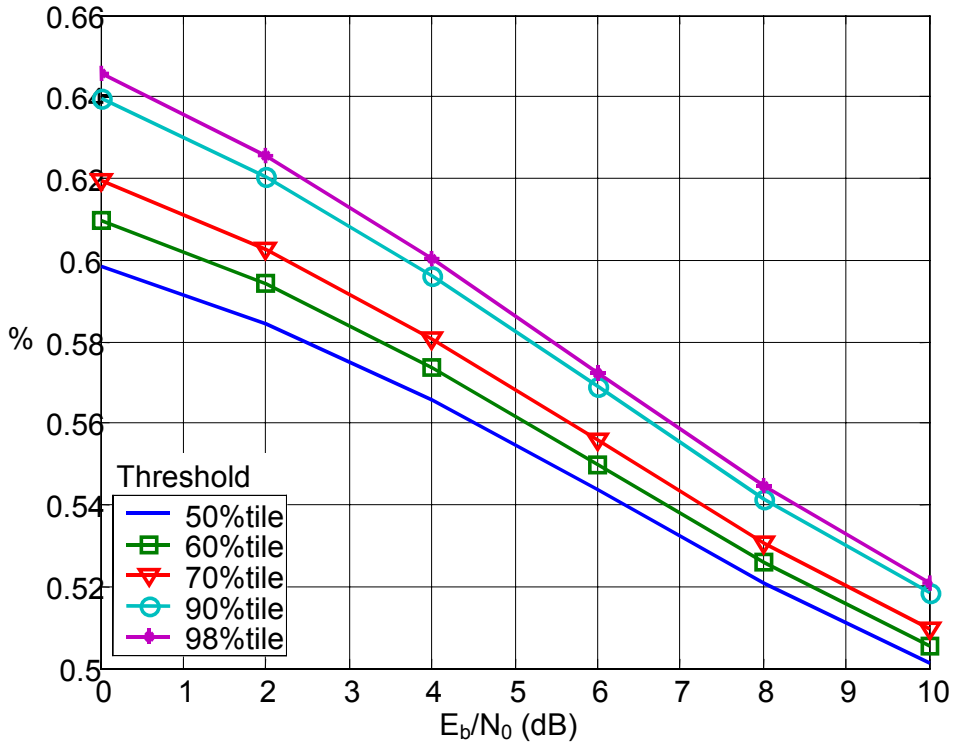

Figure 4.13 - Correlation count ratio of K_{4x6}^{10} Sequence in CM1

From Figure 4.12, it could be seen that the proposed scheme was able to achieve low P_{fa} under different SNRs for a K_{4x6}^{10} sequence. P_{fa} performance improved with a higher threshold, but this was done in the expense of more correlation operations, as shown in Figure 4.13. This was because more correlations have to be taken before acquisition was declared with a higher threshold. The P_{fa} performance of threshold at 60%-, 70%- and 80%-tile appeared to converge, but a lower threshold was preferred, as the correlation count was lower consequently.

4.3.2 Probability of False Alarm and Correlation Count of CAZAC Code

The simulation was repeated for CAZAC preambles C_{16x6}^{2}. The same parameters were investigated i.e. P_{fa} (Figure 4.14) and correlation count (Figure 4.15). The full-length threshold percentile values were obtained from Figure 4.9.

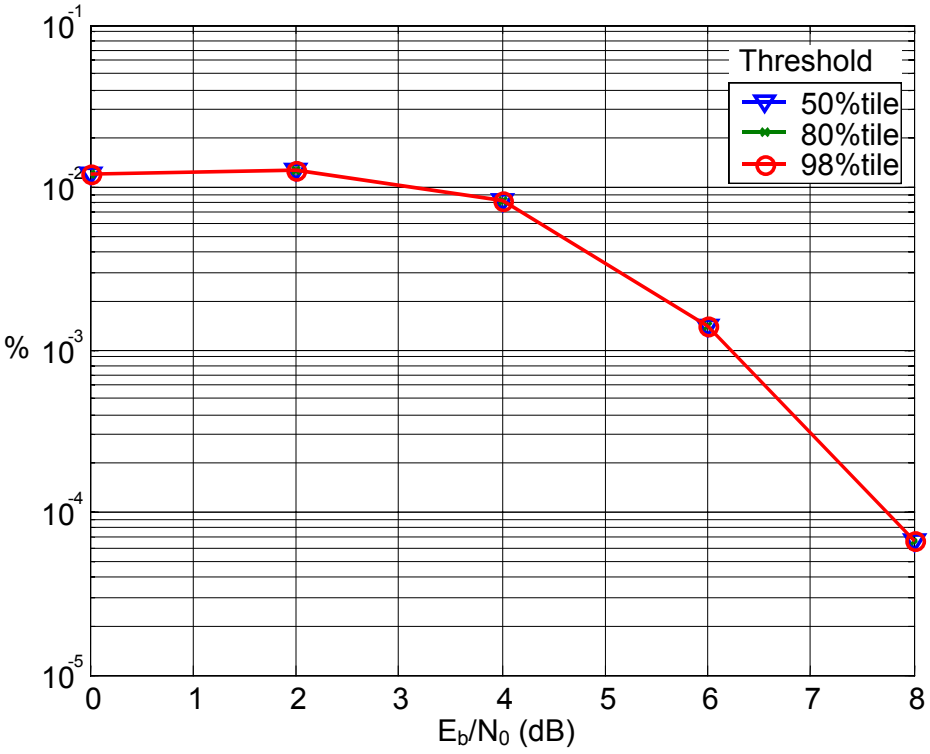

Figure 4.14 - P_{fa} performance of C_{16x6}^{2} Sequence in CM1

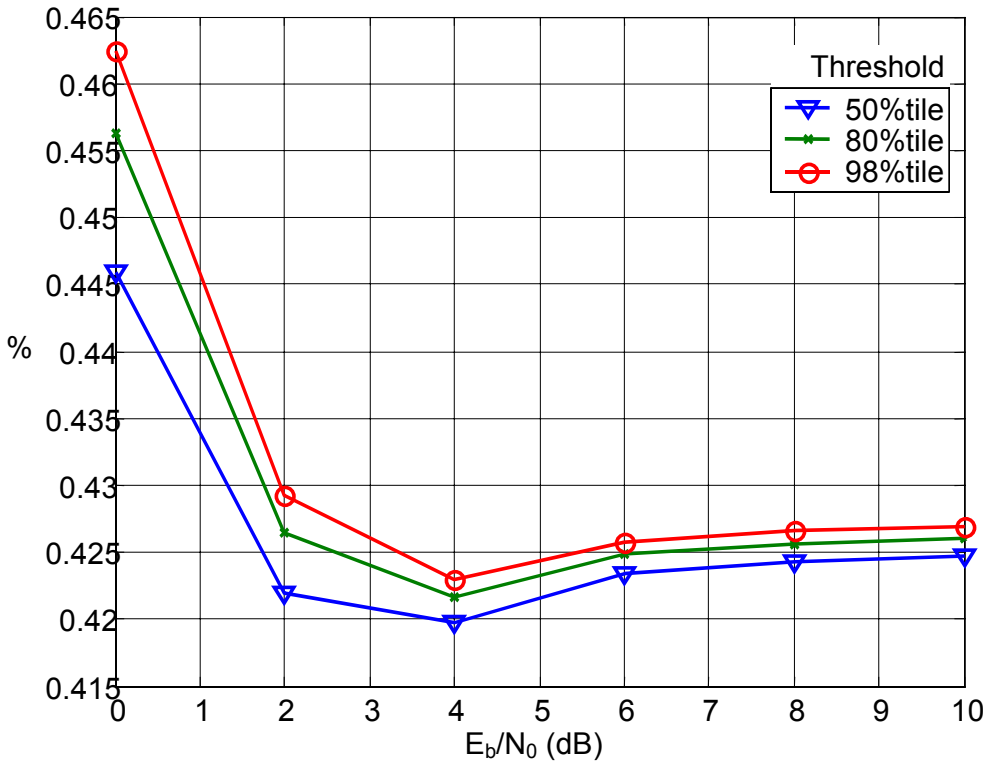

Figure 4.15 - Correlation count ratio of C_{16x6}^{2} Sequence in CM1

In comparison, the acquisition proposed scheme did not work well for the C_{16x6}^{2} sequence. Different thresholds had no effect on P_{fa} as seen from Figure 4.14. The P_{fa} performance was also worse than Barker sequences. The correlation count in Figure 4.15 appeared to level off at high SNR. CAZAC performance for the proposed acquisition scheme could be possibly improved by using more parallel search phases for a longer sequence such as C_{16}, in the expense of added complexity to the system.

4.4 Conclusion for Acquisition

Rapid acquisition is crucial to the functioning of high data rate systems like UWB. This is achieved in the expense of greater system complexity. By assigning each sub-band to a certain preamble pattern, the multi-band UWB system can exploit this inherent coding property during acquisition. As a result, certain test phases are unnecessary at the correlator. A unique scheme of using phase elimination in the double-dwell acquisition of multi-band UWB is proposed in this chapter. The thresholds have a fixed and a variable component. The fixed component is derived from the statistics of the maximum correlation values of a certain channel model. The variable threshold on the other hand depends on the channel itself.

Extensive simulations of the proposed scheme have been done and it has been found to work better with short sequences, with a low probability of false alarm and a reduced number of correlation operations required. There was a trade-off between the fixed threshold value and the correlation count ratio.

With the timing information of multi-band UWB acquired, baseband processing can begin, which is presented in the next few chapters.

Chapter 5 Multi-channel Equalization - MMSE vs RAKE

As described in Section 2.2, the main motivation for multi-band UWB is to deal with interference issues. This issue of ISI is partially addressed by multi-band UWB, in which a high overall data rate can be achieved with a relatively long PRI on each band. The channel delay spread differs under different CMs, and it is valuable to investigate the ISI that still exists under the different transmission modes, and how to deal with the residual ISI in a multi-band environment.

In this chapter, two popular receiver operations – RAKE receiver and minimum mean-square error (MMSE) equalization proposal were applied to a multi-channel system for ISI mitigation. As mentioned in Section 2.1, the multipath components are highly resolvable, making RAKE receiver a favorable choice for UWB systems. In fact, majority of the performance analysis for UWB systems utilizes RAKE receivers [26]-[28], due to its effectiveness in multipath combining. The basic version of the RAKE receiver consists of multiple fingers where each finger can detect one of the multipath components, and the signal from different paths is combined based on maximum ratio combining (MRC). MMSE equalization for UWB on the other hand is found in [28]-[30]. To harness the temporal diversity available in the dense multipath UWB channel, an over-sampling MMSE equalizer is proposed, and its merits is discussed in details in this chapter.

Through detailed theoretical analysis and extensive simulations, it was shown that the proposed 4-arm over-sampling equalizer scheme is superior to a 4-arm conventional RAKE receiver in the presence of ISI at all signal-to-noise ratios, chip rates and

channel conditions without coding. The simulated performance was shown to conform the analytical predictions. The RAKE receiver was incapable of effective ISI compensation, and a moderate level of ISI caused severe bit error rate (BER) degradation. The proposed over-sampling equalizer, on the other hand, was able to handle ISI under any channel conditions or data rate, with an acceptable BER. Over-sampling was able to achieve diversity gain, and improved the output SNR.

5.1 Inter-symbol Interference and Over-sampling Multi-channel Equalization

Having a long PRI alone is not adequate in eliminating ISI completely, especially in NLOS environment. ISI can still affect the system's performance adversely. The extent of ISI can be calculated using the maximum delay spread of each CM, defined as the time delay in the multipath impulse profile that falls below the maximum multipath power by 10dB. Through simulation of the average power decay profile of 100 UWB channels as described in [7], the 10dB maximum delay spreads τ_{max} for various CMs are complied in Table 5.1.

Table 5.1 – 10dB maximum delay spread of various CMs

	10dB maximum delay spread τ_{max}
CM1	8.92 ns
CM2	26.786 ns
CM3	56.413 ns
CM4	77.111 ns

Using the data in Table 5.1, the extent of ISI suffered by the various modes of transmission under different CMs can be estimated by the relationship

$$N_{ISI} = \begin{cases} ceil(\frac{\tau_{\max}}{T_s}) & \tau_{\max} \geq T_s \\ 0 & otherwise \end{cases} \quad (5.1)$$

where *ceil* denotes the ceiling function. N_{ISI} refers to the number of future signal pulses that suffers from ISI due to channel delay spread of the present pulse. The results from (5.1) are reproduced in Table 5.2, observing that CM1 suffers from no ISI under any modes, which is expected as it has the shortest τ_{max}. Conversely, CM4 having the

longest τ_{max}, performs worst under Mode A. The ISI in this mode affects 4 future pulses, because the PRI is the shortest.

Table 5.2 – N_{ISI} suffered by the 3 transmission modes under various CMs

	CM1	CM2	CM3	CM4
Mode A	0	2	3	4
Mode B	0	0	2	2
Mode C	0	0	0	0

As mentioned in the opening section, RAKE receiver is a popular choice for UWB reception. There are 3 types of RAKE receiver – all RAKE (ARake), selection RAKE (SRake) and partial RAKE (PRake) as described in [31]. ARake refers to a receiver with unlimited taps and is able combine signals from all L_r resolvable multipath components. SRake is able to choose the best L_b strongest paths to combine, while PRake combines the first L_p available paths, which may not necessarily be the best. SRake and PRake are therefore complexity-reduced version of ARake. PRake is simpler to implement that SRake, as PRake does not involving sorting and choosing the best path to combine.

From [32], it has been shown that under a realistic UWB channel, the performances of PRake and SRake are comparable even with L_p=L_b=4 fingers. Treating each data band as a separate channel, these results can be applied to the multi-channel equalizer, combining multipath signals from each band using PRake with 4 fingers, with perfect acquisition and synchronization assumed.

There are two kinds of interference that affects the performance of RAKE receiver: one is multipath interference (MPI) that causes ISI; the other is multiple access

interference (MAI). MPI and MAI limit the system capacity when RAKE receivers are applied. Moreover the number of RAKE fingers is practically limited for high rate systems due to large delay spread. When the delay spread is large, the frequency selective fading channel may be transformed into a frequency non-selective fading channel through channel equalization. Therefore, equalization receiver based on adaptive algorithms seems to be an effective way to recover the transmitted data by suppressing both MPI and MAI.

With this consideration, an over-sampling multi-channel equalizer per sub-band for a multi-band UWB system is proposed, which provides more effective inter-symbol interference (ISI) suppression compared with the conventional RAKE receiver when operating in channels with large delay spread. Figure 5.1 shows the block diagram for the proposed over-sampling multi-channel equalizer. With each sub-band over-sampled η-times, a temporal diversity of order η can be obtained. The diversity gain obtained by this over-sampling receiver structure is similar to the receiver diversity achieved from multiple receive antennae. The η-times over-sampled data stream is converted to η parallel streams. These parallel streams go through an adaptive MMSE equalizer for efficient equalization to minimize the effect channel distortion. Each equalizer takes in the η samples within each pulse repetition interval, and combines with a η-tap adaptive multi-channel MMSE equalizer. In addition to self-interference suppression in each band, the proposed equalizer can also reduce MAI generated by simultaneously operating piconets. With η=4, the 4-tap MMSE over-sampling equalizer shown in Figure 5.1 is similar in structure as the 4-finger RAKE structure described earlier, so that a fair performance comparison between the two receiver schemes can be carried out.

The over-sampling factor η, is related to the effective pulse width T_w' and sampling frequency f_s by

$$\eta = T_w^{'} f_s \tag{5.2}$$

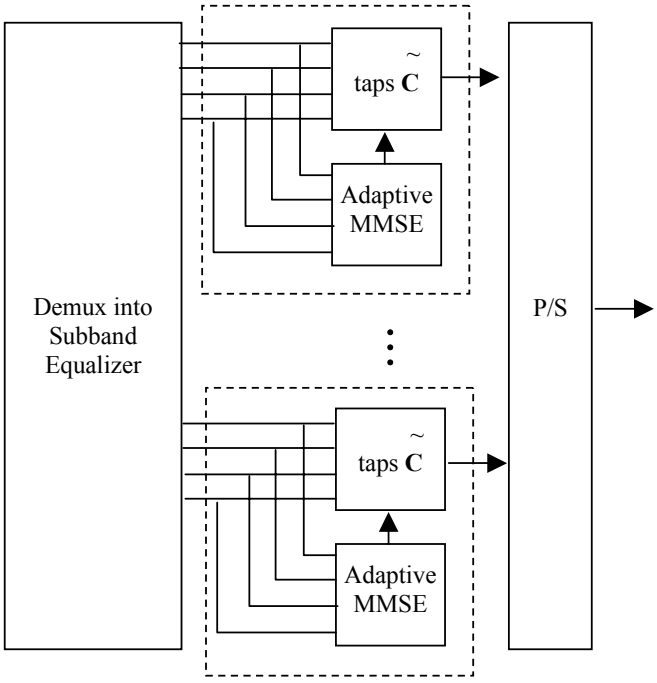

Figure 5.1 – Details of η-times over-sampling multi-channel equalizer

5.2 Bit Error Analysis

Referring to (2.2), the transmitted signal in each band can be written as

$$s(t) = \sqrt{P} \sum_{m=-\infty}^{\infty} b_m p(t - mT_s) \tag{5.3}$$

where p(t) is the pulse shaping function, with the assumption that $\int_0^{T_w} [p(t)]^2 = 1$. T_s is the PRI as listed in Table 2.2, P is the transmitted power, and b_m are normalized data symbols. According to [35], Equation (2.1) can be re-written as

$$h(t) = \sum_{k=0}^{K} h_k \delta(t - \tau_k) \tag{5.4}$$

where $h_k = X \sum_{l=0}^{L} \alpha_{k,l}$ and $\tau_k = T_l + \tau_{k,l}$. Noting that beyond a delay of τ_{max} the channel can be considered as to have faded completely, it is also possible to write

$$K = \tau_{max} f_s \tag{5.5}$$

while the number of samples η_0 within each PRI is

$$\eta_0 = T_s f_s \tag{5.6}$$

From (2.6) and (5.2), (5.6) can also be written as

$$\begin{aligned} \eta_0 &= T_w' N_B f_s \\ &= N_B \eta \end{aligned} \tag{5.7}$$

Partitioning the total channel response by the PRI of each band, within each PRI there are η_0 samples, arriving at

$$h(t) = \sum_{p=0}^{N_{ISI}} \sum_{q=0}^{\eta_0 - 1} h_{q+p\eta_0} \delta(t - \tau_{q+p\eta_0}) \tag{5.8}$$

In (5.8), the channel responses from p=1 to N_{ISI} contributes to ISI, as the delay spread spills into the next symbol period. The received signal r(t) can be obtained by convolving (5.3) with (5.8), added with AWGN n(t) of spectral density $\frac{N_0}{2}$ to get

$$u(t) = \sqrt{P} \sum_{m=-\infty}^{\infty} b_m \sum_{p=0}^{N_{ISI}} \sum_{q=0}^{\eta_0 - 1} h_{q+p\eta_0} p(t - \tau_{q+p\eta_0} - mT_s) + n(t) \tag{5.9}$$

n(t) has a two sided spectral density of $\frac{N_0}{2}$. The baseband expression for the j^{th} symbol $\mathbf{y}_j$ is

$$\mathbf{y}_j = [y_{j,0}\ y_{j,1}\ \mathrm{K}\ y_{j,\eta_0-1}]^T, \quad \text{where} \tag{5.10}$$

$$y_{j,k} = T_p \sqrt{P} \sum_{p=0}^{N_{ISI}} b_{p+j} h_{k+p\eta_0} + n_{j,k} \tag{5.11}$$

and $n_{j,k}$ is the match-filtered noise with $E(n_{j,k}^2) = \frac{N_0}{2} T_p$ and $T_p = \frac{1}{f_s}$. From (5.11), (5.10) can be rewritten as

$$\begin{aligned} \mathbf{y}_j &= \begin{pmatrix} y_{j,0} \\ y_{j,1} \\ \mathrm{M} \\ y_{j,\eta_0-1} \end{pmatrix} = T_p \sqrt{P} \begin{pmatrix} \sum_{p=0}^{N_{ISI}} b_{p+j} h_{p\eta_0} \\ \sum_{p=0}^{N_{ISI}} b_{p+j} h_{1+p\eta_0} \\ \mathrm{M} \\ \sum_{p=0}^{N_{ISI}} b_{p+j} h_{(\eta_0-1)+p\eta_0} \end{pmatrix} + \begin{pmatrix} n_{j,0} \\ n_{j,1} \\ \mathrm{M} \\ n_{j,\eta_0-1} \end{pmatrix} \\ &= T_p \sqrt{P} \begin{pmatrix} h_0 & h_{\eta_0} & \Lambda & h_{\eta_0(N_{ISI})} \\ h_1 & \mathrm{O} & & \mathrm{M} \\ \mathrm{M} & & \mathrm{O} & \mathrm{M} \\ h_{\eta_0-1} & h_{(\eta_0-1)+\eta_0} & \Lambda & h_{(\eta_0-1)+\eta_0(N_{ISI})} \end{pmatrix} \begin{pmatrix} b_j \\ b_{1+j} \\ \mathrm{M} \\ b_{N_{ISI}+j} \end{pmatrix} + \begin{pmatrix} n_{j,0} \\ n_{j,1} \\ \mathrm{M} \\ n_{j,\eta_0-1} \end{pmatrix} \end{aligned} \tag{5.12}$$

With N_B=6 bands, the receiver at only "sees" the UWB channel at each switched instance. Therefore out of a total of η_0 multipath components, only $\frac{\eta_0}{N_B} = \eta$ components are going to affect the receiver performance, recalling that η is the over-sampling factor. Equation (5.12) can be revised as

$$\hat{\mathbf{y}}_j = T_p\sqrt{P}\begin{pmatrix} h_0 & h_\eta & \Lambda & h_{\eta(N_{ISI})} \\ h_1 & \mathrm{O} & & \mathrm{M} \\ \mathrm{M} & & \mathrm{O} & \mathrm{M} \\ h_{\eta-1} & h_{(\eta-1)+\eta} & \Lambda & h_{(\eta-1)+\eta(N_{ISI})} \end{pmatrix}\begin{pmatrix} b_j \\ b_{1+j} \\ \mathrm{M} \\ b_{N_{ISI}+j} \end{pmatrix} + \begin{pmatrix} n_{j,0} \\ n_{j,1} \\ \mathrm{M} \\ n_{j,\eta-1} \end{pmatrix} \qquad (5.13)$$

$$= T_p\sqrt{P}\begin{pmatrix} \mathbf{h}_0 & \mathbf{h}_1 & \Lambda & \mathbf{h}_{N_{ISI}} \end{pmatrix}\begin{pmatrix} b_j \\ b_{1+j} \\ \mathrm{M} \\ b_{N_{ISI}+j} \end{pmatrix} + \begin{pmatrix} n_{j,0} \\ n_{j,1} \\ \mathrm{M} \\ n_{j,\eta-1} \end{pmatrix}$$

In (5.13) $\mathbf{h}_p=[h_{0+p\eta}\, h_{1+p\eta} \ldots h_{(\eta-1)+p\eta}]^T$ has been used.

5.2.1 RAKE Receiver

Collecting multipath components (h_k) by RAKE operations with taps **c** based on maximal-ratio combining (MRC), the received j^{th} symbol becomes

$$r_j = \mathbf{c}^H \hat{\mathbf{y}}_j = T_p \sqrt{P} (\sum_{p=0}^{N_{ISI}} b_{p+j} \mathbf{c}^H \mathbf{h}_p) + \mathbf{c}^H \mathbf{n}_j \tag{5.14}$$

in which $\hat{\mathbf{y}}_j = [y_{j,0}\ y_{j,1}\ \ldots\ y_{j,\eta-1}]^T$, $\mathbf{n}_j = [n_{j,0}\ n_{j,1}\ \ldots\ n_{j,\ \eta-1}]^T$ and when there is no ISI ($N_{ISI}=0$), the expression in (5.14) can be simplified to

$$r_j = T_p \sqrt{P} b_j \mathbf{c}^H \mathbf{h}_0 + \mathbf{c}^H \mathbf{n}_j, \quad N_{ISI} = 0 \tag{5.15}$$

And when there is ISI,

$$r_j = \mathbf{c}^H \hat{\mathbf{y}}_j = T_p \sqrt{P} b_j \mathbf{c}^H \mathbf{h}_0 + T_p \sqrt{P} (\sum_{p=1}^{N_{ISI}} b_{p+j} \mathbf{c}^H \mathbf{h}_p) + \mathbf{c}^H \mathbf{n}_j, \quad N_{ISI} \neq 0 \tag{5.16}$$

The first term in (5.16) is the j^{th} desired symbol, the middle term refers to ISI, and the last term is the noise term after RAKE combining. Assuming that all data symbols b_m are independent, and the ISI term is approximately Gaussian, the BER of a multi-band UWB conditioned on the channel parameters can be computed as

$$\begin{aligned} BER &= Q(\sqrt{SINR}) \\ &= Q\left(\sqrt{\frac{E(signal^2)}{E(ISI^2) + E(noise^2)}} \right) \end{aligned} \tag{5.17}$$

With the respective terms in (5.17) are defined as

$$E(signal^2) = E_b T_p (\mathbf{c}^H \mathbf{h}_0)^2 \tag{5.18}$$

$$E(ISI^2) = E_b T_p E(\sum_{k=1}^{N_{ISI}} b_{k+j} \mathbf{c}^H \mathbf{h}_k \sum_{l=1}^{N_{ISI}} b_{l+j} \mathbf{c}^H \mathbf{h}_l) \tag{5.19}$$

$$E(noise^2) = \mathbf{c}^H \mathbf{c} (\sigma^2 T_p) = \mathbf{c}^H \mathbf{c} \frac{N_0}{2} T_p \tag{5.20}$$

5.2.2 MMSE Equalizer

To obtain the optimal MMSE taps, the MMSE criterion is applied on (5.14)

$$\tilde{\mathbf{c}} = \arg\min E(\left| b_j - \tilde{\mathbf{c}}^H \hat{\mathbf{y}}_j \right|^2) \tag{5.21}$$

From [29], the solution to (5.21) is

$$\tilde{\mathbf{c}} = \left[E(\hat{\mathbf{y}}_j \hat{\mathbf{y}}_j^H) \right]^{-1} E(b_j \hat{\mathbf{y}}_j) \tag{5.22}$$

$$\begin{aligned} E(b_j \hat{\mathbf{y}}_j) &= T_p \sqrt{P} \begin{pmatrix} \mathbf{h}_0 & \mathbf{h}_1 & \Lambda & \mathbf{h}_{N_{ISI}} \end{pmatrix} E \begin{pmatrix} b_j^2 \\ b_j b_{1+j} \\ \text{M} \\ b_j b_{p+j} \end{pmatrix} \\ &= T_p \sqrt{P} \begin{pmatrix} \mathbf{h}_0 & \mathbf{h}_1 & \Lambda & \mathbf{h}_{N_{ISI}} \end{pmatrix} \begin{pmatrix} 1 \\ 0 \\ \text{M} \\ 0 \end{pmatrix} \\ &= T_p \sqrt{P} \mathbf{h}_0 \end{aligned} \tag{5.23}$$

$$\begin{aligned} E(\hat{\mathbf{y}}_j \hat{\mathbf{y}}_j^H) &= \begin{pmatrix} \mathbf{h}_0 & \mathbf{h}_1 & \Lambda & \mathbf{h}_{N_{ISI}} \end{pmatrix} E \left[\begin{pmatrix} b_j \\ b_{1+j} \\ \text{M} \\ b_{p+j} \end{pmatrix} \begin{pmatrix} b_j & b_{1+j} & \Lambda & b_{p+j} \end{pmatrix} \right] \begin{pmatrix} \mathbf{h}_0^H \\ \mathbf{h}_1^H \\ \text{M} \\ \mathbf{h}_{N_{ISI}}^H \end{pmatrix} + E(\mathbf{n}_j \mathbf{n}_j^H) \\ &= \begin{pmatrix} \mathbf{h}_0 & \mathbf{h}_1 & \Lambda & \mathbf{h}_{N_{ISI}} \end{pmatrix} \begin{pmatrix} \mathbf{h}_0^H \\ \mathbf{h}_1^H \\ \text{M} \\ \mathbf{h}_{N_{ISI}}^H \end{pmatrix} + \frac{N_0}{2} \mathbf{I}_N, \quad \mathbf{I}_N = \text{identity matrix of size N} \\ &= \overline{\mathbf{H}} \overline{\mathbf{H}}^H + \frac{N_0}{2} \mathbf{I}_N \end{aligned} \tag{5.24}$$

In (5.24), $\overline{\mathbf{H}} = \begin{pmatrix} \mathbf{h}_0 & \mathbf{h}_1 & \Lambda & \mathbf{h}_{N_{ISI}} \end{pmatrix}$. The received j[th] symbol for a MMSE equalizer also takes the form of (5.16), with the definition of the desired signal, ISI and noise terms unchanged as that of a RAKE receiver. The BER expression, the calculations of the various energies described in (5.18)-(5.20) for RAKE receiver are applicable also to the MMSE case with taps weights $\tilde{\mathbf{c}}$.

5.2.3 RAKE vs MMSE Tap Weights When N_{ISI}=0

Without ISI, the instantaneous SNR γ after RAKE combining according to (5.18) and (5.20) is

$$\gamma = \frac{E_b \mathbf{c}^H \mathbf{h}_0 \mathbf{h}_0^H \mathbf{c}}{\mathbf{c}^H \mathbf{c} \sigma^2} = \frac{E_b \mathbf{c}^H \mathbf{R}_h \mathbf{c}}{\mathbf{c}^H \mathbf{c} \sigma^2} \tag{5.25}$$

where $\mathbf{R}_h = \mathbf{h}_0 \mathbf{h}_0^H$. Since RAKE aims to maximize instantaneous SNR of each finger, the conjugate derivative $\frac{\partial}{\partial \mathbf{c}^*}$ of (5.25) is taken and set to zero. From [36] this becomes

$$\begin{aligned} &\frac{\partial \gamma}{\partial \mathbf{c}^*} = 0 \\ &E_b \cdot \mathbf{R}_h \mathbf{c}(\sigma^2 \mathbf{c}^H \mathbf{c}) = \sigma^2 \mathbf{c}(E_b \cdot \mathbf{c}^H \mathbf{R}_h \mathbf{c}) \\ &\mathbf{R}_h \mathbf{c} = \left(\frac{\mathbf{c}^H \mathbf{R}_h \mathbf{c}}{\mathbf{c}^H \mathbf{c}} \right) \mathbf{c} = \lambda \mathbf{c} \end{aligned} \tag{5.26}$$

where $\lambda = \frac{\mathbf{c}^H \mathbf{R}_h \mathbf{c}}{\mathbf{c}^H \mathbf{c}}$, the maximum eigenvalue of $\mathbf{R}_h$. Since all entries in $\mathbf{R}_h$ are linear combinations of $\mathbf{h}_0$, the only non-trivial solution is to set

$$\mathbf{c} = k\mathbf{h}_0, \quad k \in \Re, k \neq 0 \tag{5.27}$$

Substituting (5.27) into λ,

$$\begin{aligned} \lambda &= \frac{(k\mathbf{h}_0^H)\mathbf{h}_0 \mathbf{h}_0^H (k\mathbf{h}_0)}{(k\mathbf{h}_0^H)(k\mathbf{h}_0)} \\ &= \mathbf{h}_0^H \mathbf{h}_0 \\ &= \sum_{k=0}^{\eta-1} h_k^2 \end{aligned} \tag{5.28}$$

Substituting (5.26) into (5.25),

$$\begin{aligned} \gamma &= \frac{E_b \mathbf{c}^H \lambda \mathbf{c}}{\mathbf{c}^H \mathbf{c} \sigma^2} = \frac{E_b \lambda}{\sigma^2} \\ &= \sum_{k=0}^{\eta-1} \frac{E_b h_k^2}{\sigma^2} \\ &= \sum_{k=0}^{\eta-1} \gamma_k \end{aligned} \tag{5.29}$$

Equation (5.29) verifies that the solution given in (5.27) is indeed MRC, where the final SNR is the sum of the individual SNRs of each finger.

For MMSE solution, (5.22)-(5.24) are used, noting that with N_{ISI}=0, the channel response is $\overline{\mathbf{H}} = \mathbf{h_0}$. Applying the Sherman-Morrison-Woodbury formula on (5.24)

$$\begin{aligned}\left[E(\hat{\mathbf{y}}_j \hat{\mathbf{y}}_j^H)\right]^{-1} &= \left(\mathbf{h}_0\mathbf{h}_0^H + \frac{N_0}{2}\mathbf{I}_K\right)^{-1} \\ &= \frac{2}{N_0}\mathbf{I}_K - \frac{\left(\frac{2}{N_0}\mathbf{I}_K\right)\mathbf{h}_0\mathbf{h}_0^H\left(\frac{2}{N_0}\mathbf{I}_K\right)}{1+\mathbf{h}_0^H\left(\frac{2}{N_0}\mathbf{I}_K\right)\mathbf{h}_0} \\ &= \frac{2}{N_0}\left(\mathbf{I}_K - \frac{2\mathbf{h}_0\mathbf{h}_0^H}{N_0+2\mathbf{h}_0^H\mathbf{h}_0}\right) \end{aligned} \quad (5.30)$$

Substituting (5.30) and (5.23) into (5.22),

$$\begin{aligned}\tilde{\mathbf{c}} &= \frac{2}{N_0}\left(\mathbf{I}_K - \frac{2\mathbf{h}_0\mathbf{h}_0^H}{N_0+2\mathbf{h}_0^H\mathbf{h}_0}\right)T_p\sqrt{P}\mathbf{h}_0 \\ &= \frac{2T_p\sqrt{P}}{N_0}\left(\mathbf{h}_0 - \frac{2\mathbf{h}_0\mathbf{h}_0^H\mathbf{h}_0}{N_0+2\mathbf{h}_0^H\mathbf{h}_0}\right) \\ &= \frac{2T_p\sqrt{P}}{N_0}\left(1-\frac{2\mathbf{h}_0^H\mathbf{h}_0}{N_0+2\mathbf{h}_0^H\mathbf{h}_0}\right)\mathbf{h}_0 = k\mathbf{h}_0 \end{aligned} \quad (5.31)$$

The MMSE tap weight in (5.31) is in the form of (5.27), and therefore MMSE equalization also maximizes the output SNR similar to that of RAKE, given in (5.29).

5.2.4 RAKE vs MMSE Tap Weights When $N_{ISI} \neq 0$

With ISI, the RAKE receiver continues to maximize output SNR by MRC, therefore the tap weights are still given by (5.27). For the weights of MMSE, the inverse to (5.24) needs to be obtained. By applying Sherman-Morrison-Woodbury formula,

$$\begin{aligned}\left[E(\hat{\mathbf{y}}_j \hat{\mathbf{y}}_j^H)\right]^{-1} &= \left[\overline{\mathbf{H}}\overline{\mathbf{H}}^H + \frac{N_0}{2}\mathbf{I}_N\right]^{-1} \\ &= \frac{2}{N_0}\mathbf{I}_N - \left(\frac{2}{N_0}\mathbf{I}_N\right)\overline{\mathbf{H}}\left(\mathbf{I}_{N_{ISI}} + \frac{2}{N_0}\overline{\mathbf{H}}^H\mathbf{I}_N\overline{\mathbf{H}}\right)^{-1}\overline{\mathbf{H}}^H\left(\frac{2}{N_0}\mathbf{I}_N\right) \\ &= \frac{2}{N_0}\mathbf{I}_N - \left(\frac{2}{N_0}\right)^2\overline{\mathbf{H}}\left(\mathbf{I}_{N_{ISI}} + \frac{2}{N_0}\overline{\mathbf{H}}^H\overline{\mathbf{H}}\right)^{-1}\overline{\mathbf{H}}^H \qquad (5.32)\end{aligned}$$

Equation (5.32) cannot be further simplified. Therefore, the MMSE tap weights for an ISI corrupted received signal have to be obtained experimentally.

The effects of over-sampling can be observed from (5.29). With a higher over-sampling factor η, the output SNR γ is going to increase, in turn bringing down the bit error rate. Although the MMSE tap weights when ISI$\neq$0 cannot be obtained analytically, BER is expected to decrease also with a higher η. The trade-off is an increased system complexity.

5.3 Simulation Results and Discussions for Multi-channel Equalization

The analysis presented in Section 5.2 was verified by extensive simulations presented in this section. The BER performance of a multi-channel RAKE and MMSE receiver was compared against each other in a multi-band UWB environment. The simulations were conducted in the various transmission modes and CMs, with chip rates and PRIs as shown in Table 2.2. Other simulation parameters are recorded in Table 5.3. Both receivers employed a 4-tap structure to gather multipath energy and suppress ISI, and perfect acquisition and channel estimation was assumed. The results were grouped by the CMs that each simulation was applied so to compare the performance of the various transmission modes.

Table 5.3 – Simulation Parameters

No. of sub-bands N_B	Over-sampling per sub-band η	No. of UWB channels per sub-band	Packet Size	Coding
6	4	100	1105 bytes	Nil

5.3.1 Channel Model 1

Figure 5.2 shows the simulated results of both RAKE and MMSE receiver in various transmission modes under CM1. It shows that there were little performance differences in terms of BER among the 3 modes, despite their different data rates. The difference in SNR among the 3 modes was less than 1dB at a BER of 10^{-4}. This could be explained from Table 5.2, in which none of the modes suffered from ISI. Using this fact and (5.15), the BER performance could be expected to be comparable. Under such favorable channel conditions (noting that CM1 refers to a LOS channel less than 4m), it would be prudent to apply the fastest mode for transmission i.e. Mode A, with little penalty in BER.

In addition, simulation also showed that in the absence of ISI, MMSE or RAKE receiver gave the same BER performance. This result agreed with the analysis presented in Section 5.2.3, in Equations (5.27) and (5.31).

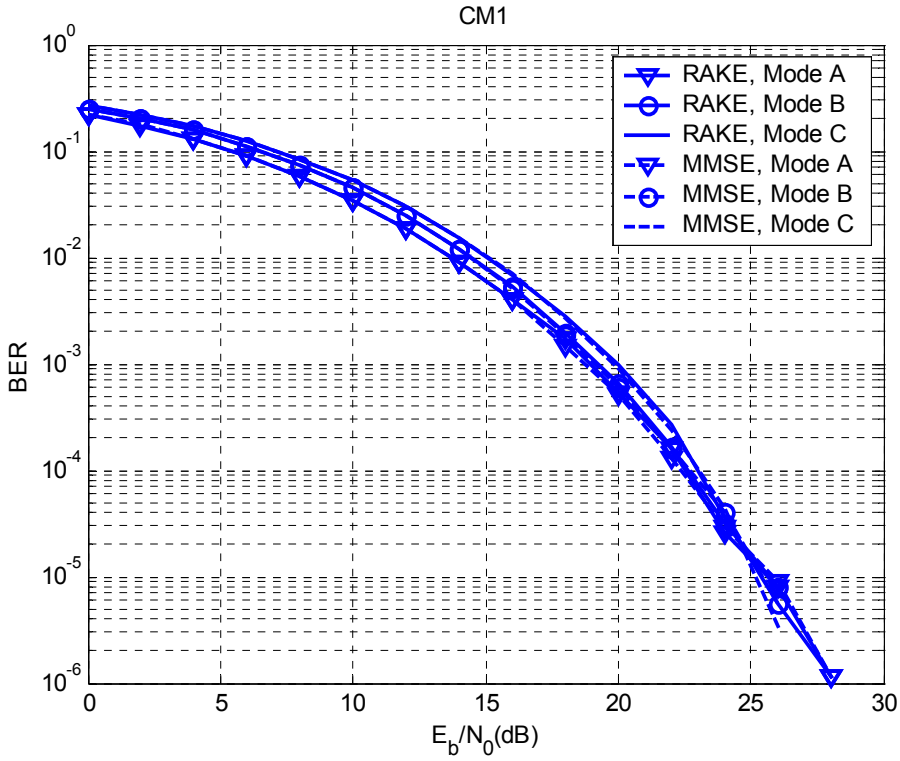

Figure 5.2 – RAKE vs MMSE in CM1

5.3.2 Channel Model 2

Figure 5.3 shows the BER performance results for CM2. Its behavior could be explained again from Table 5.2. In the absence of ISI with Modes B and C, the BER plot was again identical for both MMSE and RAKE. In fact the curves in these two modes concurred also with those in Figure 5.2, showing a BER of 10^{-4} at about 22dB. However in Mode A, having the shortest PRI that causing ISI in CM2 (N_{ISI}=2), MMSE outperformed RAKE in the high SNR region by a big margin. The curve for RAKE in Mode A was observed to be asymptotic at BER = 2 x 10^{-4}, in which there was no BER improvement with SNR increase beyond this point. No such asymptote was found in the curve for MMSE; it was a monotonically decreasing function. Expectedly, ISI took its toll on the BER performance of MMSE equalizer. An SNR of about 27dB was needed to achieve a BER of 10^{-4}. Nevertheless, MMSE equalizer outperformed RAKE receiver at all SNRs in this mode.

The asymptotic behavior of RAKE receiver meant that it had very little immunity against ISI. A RAKE receiver merely gathered energy, with the aim of SNR maximization. At high SNR, the noise term in (5.20) became much smaller than the ISI term in (5.19), and therefore the BER expression in (5.17) simplifies to

$$BER_{High\,\gamma} = Q\left(\sqrt{\frac{E(signal^2)}{E(ISI^2)}}\right)$$
$$= Q(\sqrt{SIR}) \qquad (5.33)$$

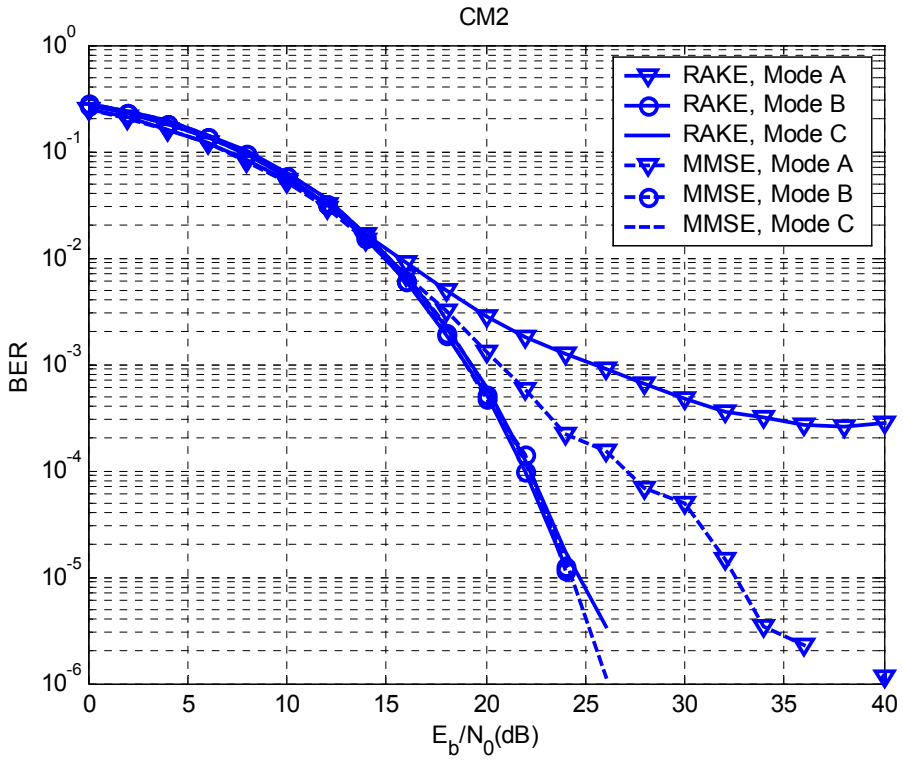

Figure 5.3 – RAKE vs MMSE in CM2

5.3.3 Channel Model 3

Figure 5.4 shows the performance of the various modes under CM3. Referring once more to Table 5.2, the performance of MMSE and RAKE receiver in Mode C could be expected to be identical, because in Mode C the PRI was long enough to eliminate ISI completely. In Mode B, N_{ISI}=2, and similar to that in Figure 5.3, MMSE outperformed RAKE receiver at all SNRs. At BER = 2 x 10^{-4}, MMSE had an almost 4dB gain over RAKE. In Mode A, where the problem of ISI was the most severe (N_{ISI}=3), the RAKE receiver again showed asymptotic trends at BER = 10^{-2}. On the contrary MMSE equalizer at Mode A was much better in terms of BER, showing again that it was much better equipped to handle ISI corrupted signals than RAKE receiver.

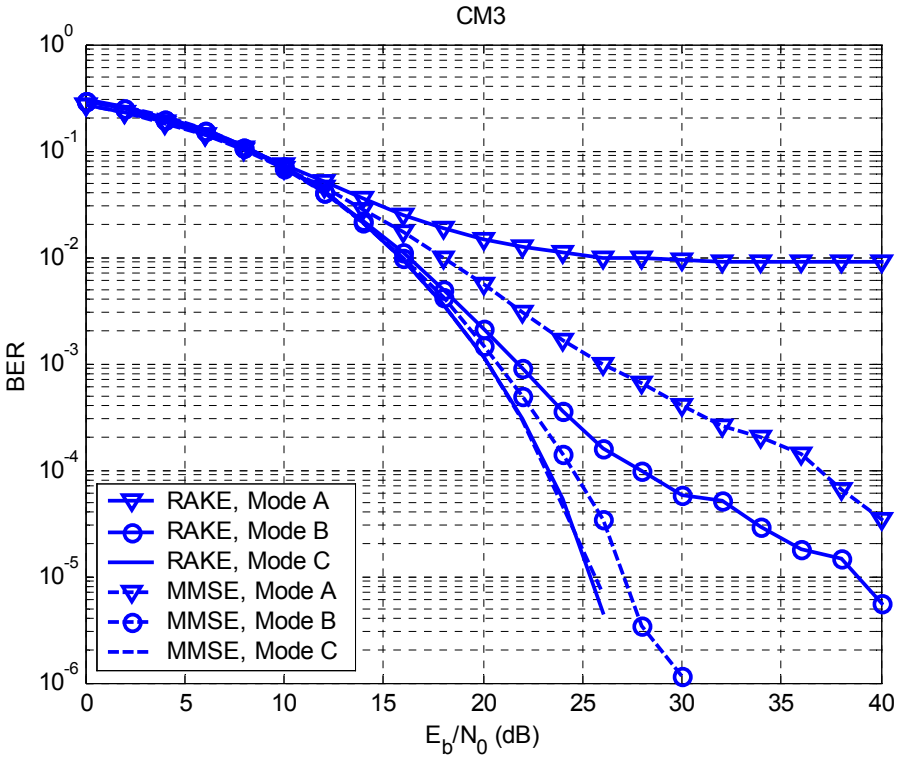

Figure 5.4 – RAKE vs MMSE in CM3

5.3.4 Channel Model 4

Figure 5.5 shows the performance of the various modes under CM4. Once again, under Mode C there was no difference between the performances the two receivers, due to the absence of ISI. The performances of the other 2 modes were worse, because of the relatively long delay spread. RAKE receiver plot showed an asymptote at BER = 2 x 10^{-3} and BER = 3 x 10^{-2} in modes B and A respectively. Since Mode A (N_{ISI}=4) suffered more ISI than Mode B (N_{ISI}=2), it was expected to have a lower SIR. For the modes with ISI, MMSE equalizer once again outperformed RAKE at all SNRs.

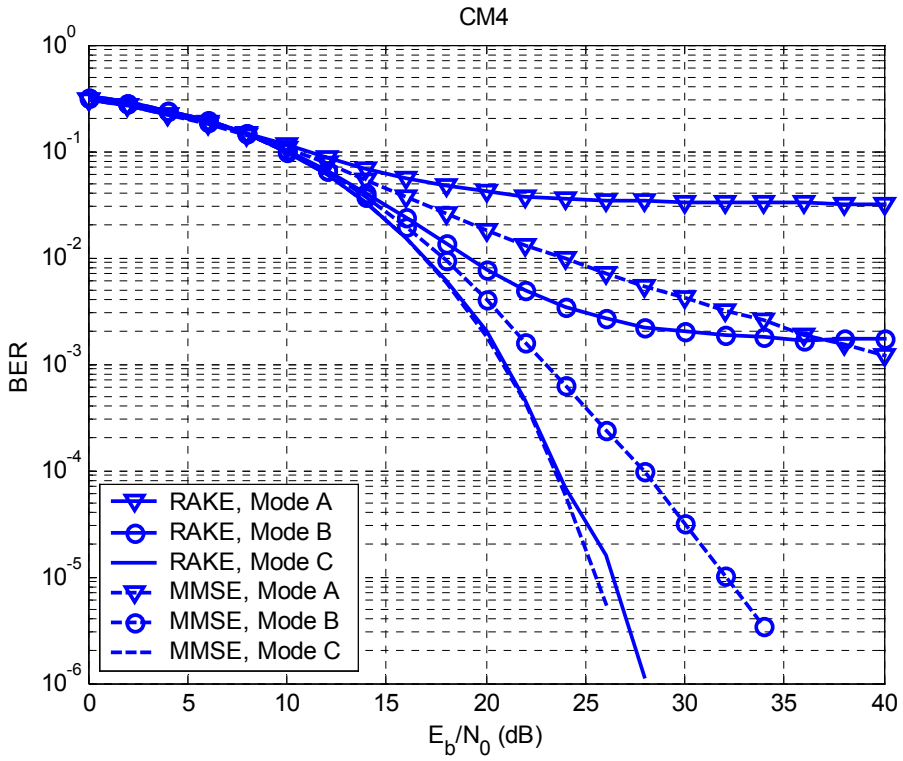

Figure 5.5 – RAKE vs MMSE in CM4

To verify the expressions in (5.17)-(5.20), the analysis curves in RAKE and MMSE were against the simulated curves in Figure 5.6 and Figure 5.7 respectively. CM4 is chosen because it encompasses all the various ISI scenarios – extreme ISI in Mode A, moderate ISI in Mode B, and zeros ISI in Mode C. In both figures, the simulated curves concurred with the analytic curves, in the ISI-corrupted and ISI-free cases. For the ISI-corrupted cases, error floors are observed in the analytical curves in the RAKE receiver again. This is not observed in the analytical curves at the receiver with MMSE equalizer, in which the BER decreases with increasing SNR. This agreement between analysis and simulation is observed in other CMs also, since none of their ISI corruption is worse than Mode A in CM4. The results for other CMs are not reproduced here. This validated the analysis presented in Section 5.2.

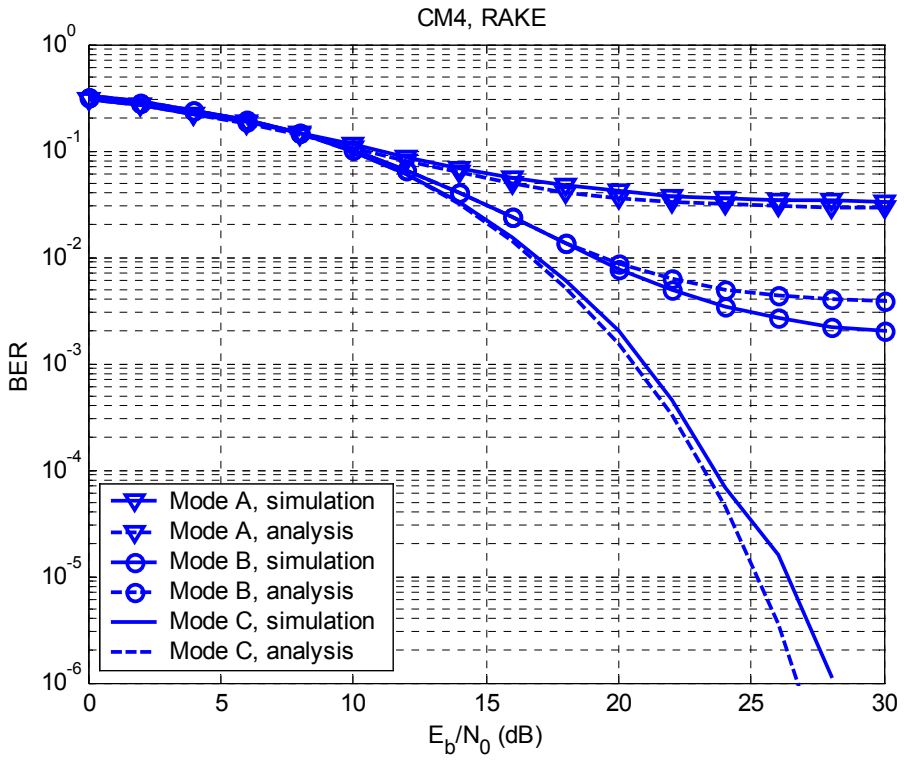

Figure 5.6 – Comparison between analytic and simulated results for RAKE receiver in CM4

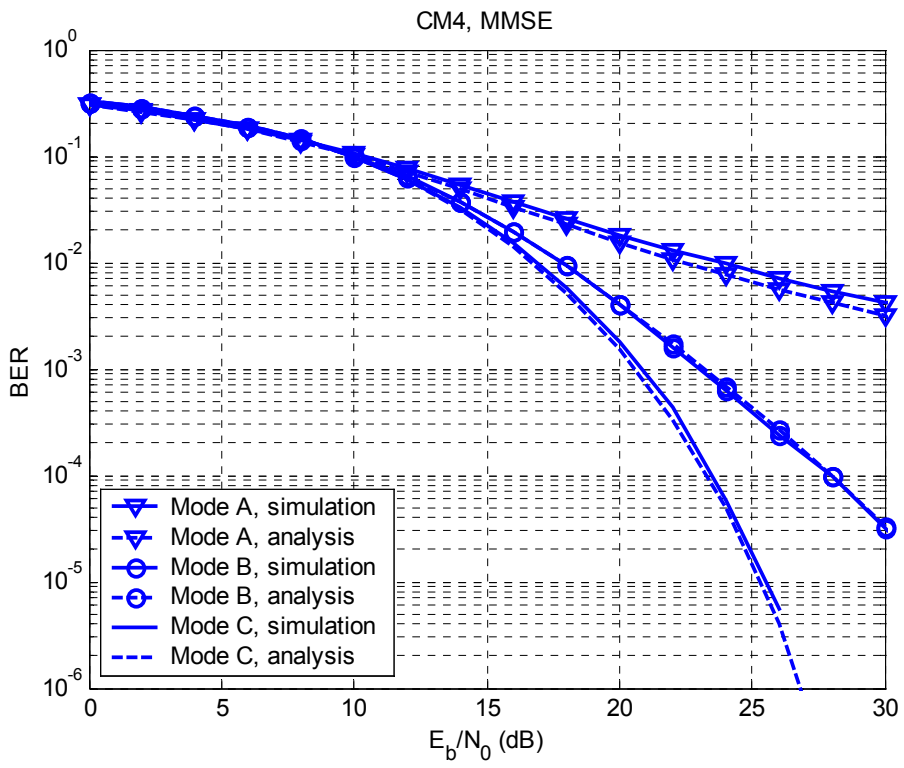

Figure 5.7 – Comparison between analytic and simulated results for MMSE receiver in CM4

5.4 Conclusion for Multi-channel Equalization

ISI is an important factor in influencing BER performance. In this chapter, the estimation of the number of symbols under the influence of ISI from previous symbols has been presented, using the 10dB maximum delay spread and PRI. The BER performance analysis for an over-sampled multi-band UWB system, based on this ISI estimate has been derived. Its validity has been confirmed by simulation, which agrees with the theoretical prediction using this method.

Through theoretical analysis, the merit of the over-sampling equalizer has been demonstrated. A temporal diversity of order η can be obtained by over-sampling η-times, similar to the receiver diversity achieved from multiple receive antennae. Output SNR is shown to improve with a higher over-sampling factor, in the expense of more complexity.

The BER performances of multi-channel RAKE and MMSE receivers have been extensively simulated, both in the ISI and ISI-free cases. The two receiver configurations were shown give similar BER curves when ISI was absent, which had been explained by theoretical analysis. However, when ISI is present, the over-sampling MMSE equalizer consistently outperformed RAKE receiver at all SNRs. RAKE showed little ISI tolerance, and its BER was observed to become asymptotic at high SNR. MMSE on the other hand was able to mitigate ISI and gave a reasonably well performance even at adverse channels. Therefore, MMSE was a more suitable candidate than RAKE for energy collection over UWB multipath channels.

The results presented in this chapter can be used to apply the other aspects of multi-band UWB design. For example, Mode C does not contribute to ISI under any channel model, hence a favorable mode for acquisition purposes, because preambles are not protected by coding. An ISI-free environment is therefore crucial for such purposes.

Lastly, the results of this work on multi-channel MMSE equalizer can easily be extended to a multi-user case, in which the multi-band UWB suffers not only from ISI but also multiple access interference (MAI). MMSE receiver will need to suppress both ISI and MAI. This will be explored in Chapter 7.

Chapter 6 Coding

In Chapter 5 the performance of the various transmission modes in different channel models analyzed and simulated. Bit error rate can be improved further by applying forward error correction (FEC) to the transmitted UWB signals. With the very high data rate of UWB systems, it is crucial to select a coding scheme that make the best possible use of the resources available for transmission, viz. bandwidth, power and complexity. Structured coding such as block code, convolutional code, turbo code and low-density parity-check is often utilized for conventional bandwidth limited applications. With plentiful spectrum, it is worthwhile to investigate the coding strategy for multi-band UWB system to make best use of bandwidth and complexity to meet low cost and low power consumption requirement.

In this chapter, a simplified coding scheme is proposed based on a concatenated Reed-Solomon (RS) code as outer-code and Quadrature M-ary Orthogonal Keying (QMOK) as inner-code. The performance of the proposed RS-QMOK coding scheme is compared against ½-rate convolutional code (CC) of constraint length K_c=7. An interleaver structure is examined to exploit the inherent frequency diversity available to multi-band UWB systems, giving further BER improvement.

Single-stream and multi-stream encode/decode strategies are also examined, and the system models are shown in Figure 6.1 (a) and (b) respectively. In multi-streaming, coding and decoding is done independently on each sub-band. Trade-off between performance and complexity, flexibility of using either single-stream or multi-streams

will be carefully examined and the detailed results will be presented in Section 6.2. The results of this chapter have been published in [37].

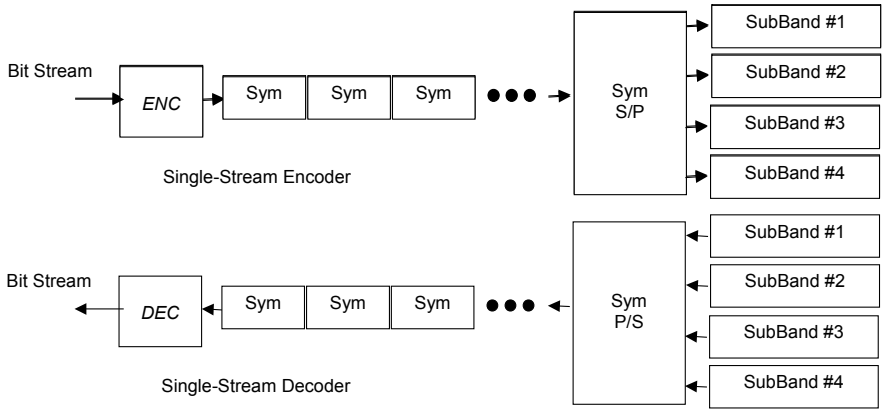

Figure 6.1 (a) - Single-stream encode/decode for multi-band UWB system

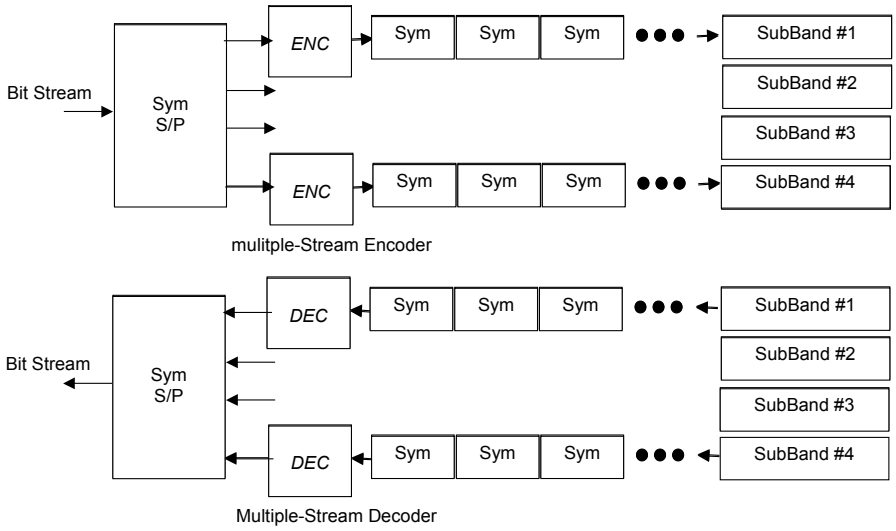

Figure 6.1 (b) - Multi-stream encode/decode for multi-band UWB system

6.1 Components of the Concatenated Code

In this section the choice of using RS as outer code and QMOK as inner code is explained with the properties of the individual codes. Based on the RS-QMOK proposal, the coder and decoder in Figure 1.1 can be expanded as shown in Figure 6.2.

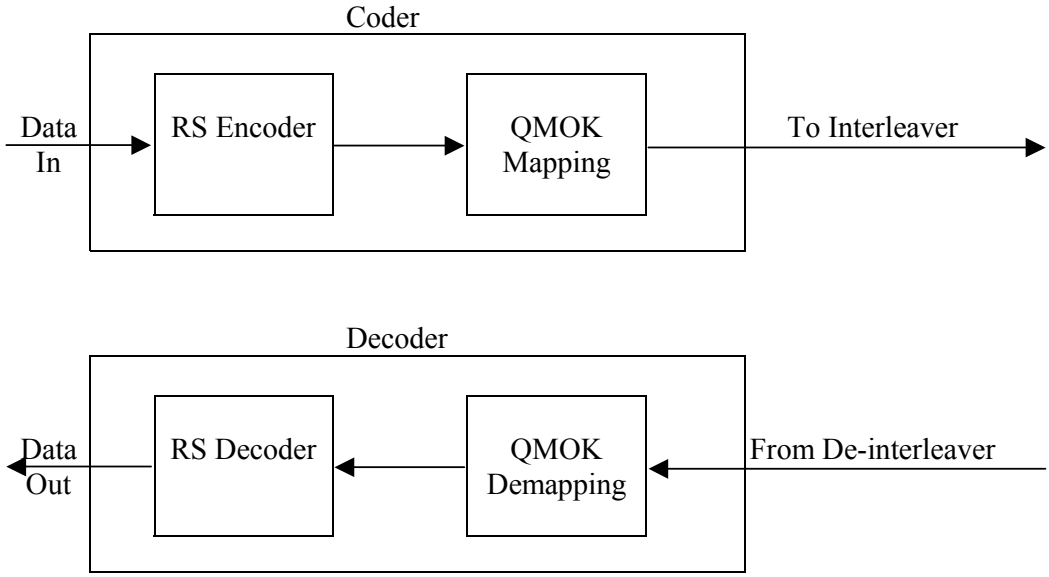

Figure 6.2 – Coder/decoder for RS-QMOK

The first observation is that both RS and QMOK are linear codes. This helps to lower hardware complexity, faster processing and lower power consumption than non-linear codes such as convolutional codes. More importantly, high-speed linear coders and decoders are easier to fabricate, which has become a design bottleneck for high data rate UWB systems.

6.1.1 Properties of the Quadrature M-ary Orthogonal Keying Inner Code

The inner QMOK is a ½ rate code, generating 8 bits with a 4 bits input, as shown in Figure 6.3. It makes use of an orthogonal mapping, such as the rows in the Walsh-hadamard matrix. M-ary orthogonal coding is chosen due to its power efficiency, making good use of the large bandwidth available to UWB systems. The availability of fast Walsh-hadamard transformer with low latency and complexity is another added advantage. The QMOK mapping matrix is shown in Table 6.1. The coded QMOK symbols are not exactly orthogonal with one another. Hence compared with Walsh-hadamard code, QMOK loses a little in coding gain, in exchange of transmitting one more bit per coded symbol.

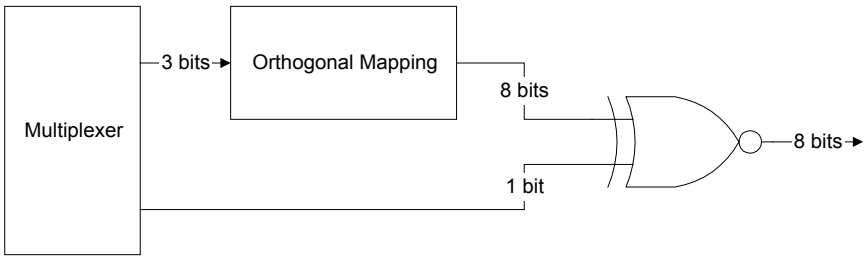

Figure 6.3 –QMOK encoder

Table 6.1 – QMOK mapping table

Input Symbol	Output Symbol	Input Symbol	Output Symbol
0 0 0 0	-1 -1 -1 -1 -1 -1 -1 -1	1 0 0 0	1 1 1 1 1 1 1 1
0 0 0 1	-1 1 -1 1 -1 1 -1 1	1 0 0 1	1 -1 1 -1 1 -1 1 -1
0 0 1 0	-1 -1 1 1 -1 -1 1 1	1 0 1 0	1 1 -1 -1 1 1 -1 -1
0 0 1 1	-1 1 1 -1 -1 1 1 -1	1 0 1 1	1 -1 -1 1 1 -1 -1 1
0 1 0 0	-1 -1 -1 -1 1 1 1 1	1 1 0 0	1 1 1 1 -1 -1 -1 -1
0 1 0 1	-1 1 -1 1 1 -1 1 -1	1 1 0 1	1 -1 1 -1 -1 1 -1 1
0 1 1 0	-1 -1 1 1 1 1 -1 -1	1 1 1 0	1 1 -1 -1 -1 -1 1 1
0 1 1 1	-1 1 1 -1 1 -1 -1 1	1 1 1 1	1 -1 -1 1 -1 1 1 -1

From [38], the symbol error rate of an orthogonal coded signal P_{oc} can be written as

$$P_{oc} = \exp\left(-\log_2 M \left(\frac{E_s}{N_0} + 1 \right) \right) \tag{6.1}$$

With 8 bits in a QMOK output symbol, its symbol error P_{qs} is

$$\begin{aligned} P_{qs} &= 1 - (1 - P_{oc})^8 \\ &\approx 8P_{oc} \\ &= 8\exp\left(-2\left(\frac{E_s}{N_0} + 1 \right) \right) \quad \text{if } P_{oc} \text{ is small} \end{aligned} \tag{6.2}$$

where M=4 for QMOK code. The corresponding bit error rate P_{qb} is

$$\begin{aligned} P_{qb} &= \frac{2^{k-1}}{2^k - 1} P_{qs} \\ &= \frac{4}{7}\left(8\exp\left(-2\left(\frac{E_s}{N_0} + 1 \right) \right) \right) \end{aligned} \tag{6.3}$$

The coding gain of soft-decision QMOK in an AWGN channel according to (6.3) is shown in Figure 6.4. Coding gain is registered even at low SNR, and this gain increases slowly with SNR. At a BER of 10^{-5}, the coding gain is about 2.1dB. These properties will be revisited in the examination of RS-QMOK code.

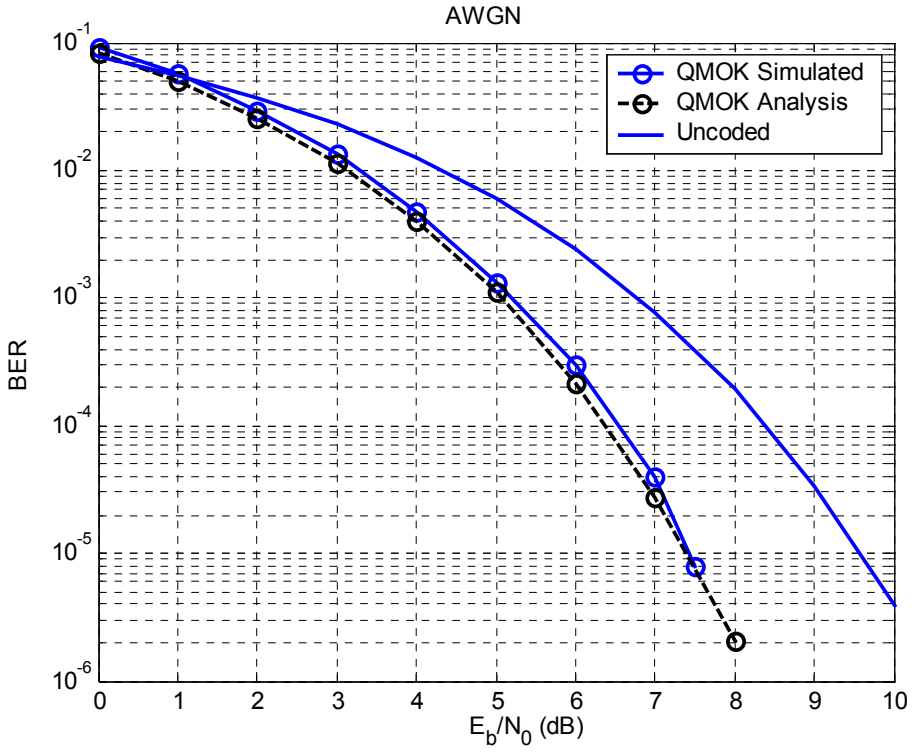

Figure 6.4 – BER performance of QMOK in AWGN channel

6.1.2 Properties of the Reed-Solomon Outer Code

Reed-Solomon code is a non-binary code that is able to correct multiple symbol errors. Existence of efficient hard-decision decoding algorithms also allow relatively long RS codes to be used, and high speed implementation is possible. Reed-Solomon code is used as outer code for many applications, such as [39]. The various properties of the outer code selected for the RS-QMOK coding scheme is summarized in Table 6.2.

Table 6.2 –RS outer code parameters

k (bits per symbol)	N (Word Length)	K (Symbol Length)	R_c (Code Rate)	D_{min} (Minimum Distance)	t (No. of correctable symbol errors
8	255	221	$\frac{221}{255}$	35	17

The code was chosen with this configuration so that it is able to correct multiple symbol errors without sacrificing the code rate R_c too much.

From [16], the hard-decision word error probability P_{ew}, the symbol error probability P_{es} and bit error probability P_{eb} is given by

$$P_{ew} = \sum_{i=t+1}^{N} \binom{N}{i} P_M^i (1-P_M)^{N-i} \tag{6.4}$$

$$P_{es} = \frac{1}{N} \sum_{i=t+1}^{N} i \binom{N}{i} P_M^i (1-P_M)^{N-i} \tag{6.5}$$

$$P_{eb} = \frac{2^{k-1}}{2^k - 1} P_{es} \tag{6.6}$$

where P_M is the symbol error probability of an uncoded system. Considering 4 QPSK symbols (since k=8) as a RS symbol, the P_M with this symbol arrangement is

$$P_M = 1 - \left(1 - 2Q\left(\sqrt{\frac{E_s}{N_0}}\right)\right)^4 \tag{6.7}$$

$$\approx 4\left(2Q\left(\sqrt{\frac{E_s}{N_0}}\right)\right) \quad \text{if } 2Q\left(\sqrt{\frac{E_s}{N_0}}\right) \text{ is small}$$

And the corresponding decoded bit error rate P'_{eb} is

$$P'_{eb} = \frac{1}{4} P_{eb} \tag{6.8}$$

The BER performance of the chosen RS code in an AWGN channel based on (6.4)-(6.8) is shown in Figure 6.5.

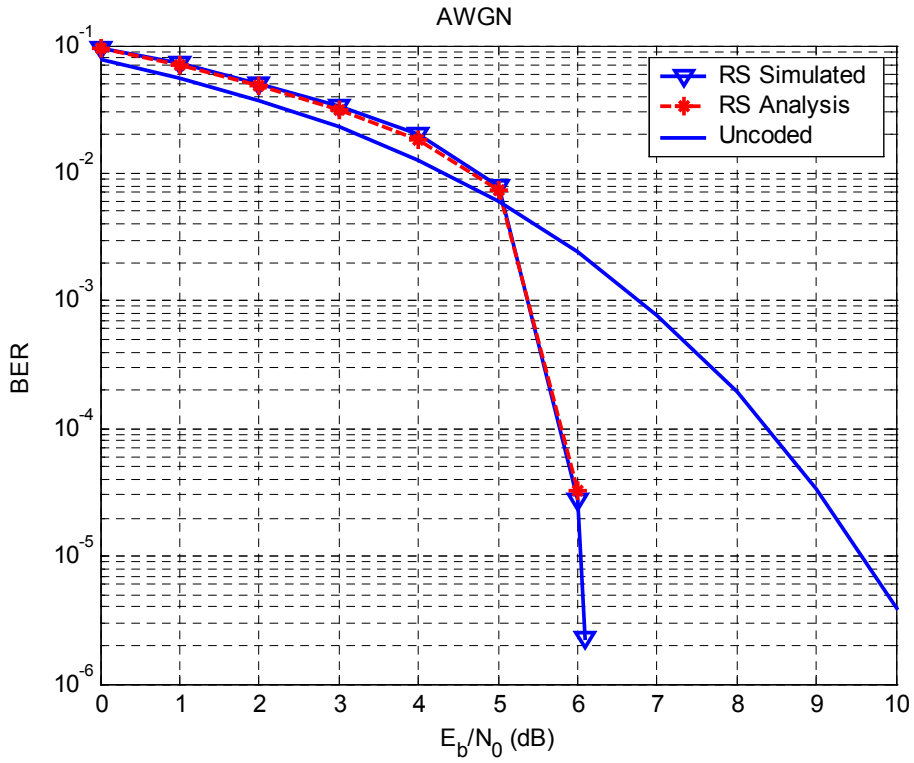

Figure 6.5 – BER performance of Reed-Solomon code in AWGN channel

At high SNR, Reed-Solomon code is very powerful, with a coding gain of 3.5dB at a BER of 10^{-5}. In fact the BER curve after 6dB is almost vertical, giving an even greater coding gain at lower BER level.

6.1.3 Properties of the RS-QMOK Concatenated Code

As shown in Table 6.2, since k=8, two QMOK symbols are needed for a RS symbol at the outer code. Equation (6.2) can be used to derive the symbol error rate P_{QM} of 2 QMOK symbols for (6.5) and (6.6),

$$P_{QM} = 16\exp\left(-2\left(\frac{E_s}{N_0}+1\right)\right) \tag{6.9}$$

The theoretical BER performance of the concatenated RS-QMOK code in AWGN is plotted in Figure 6.6. The analytical curves for RS and QMOK as individual codes are reproduced for comparison.

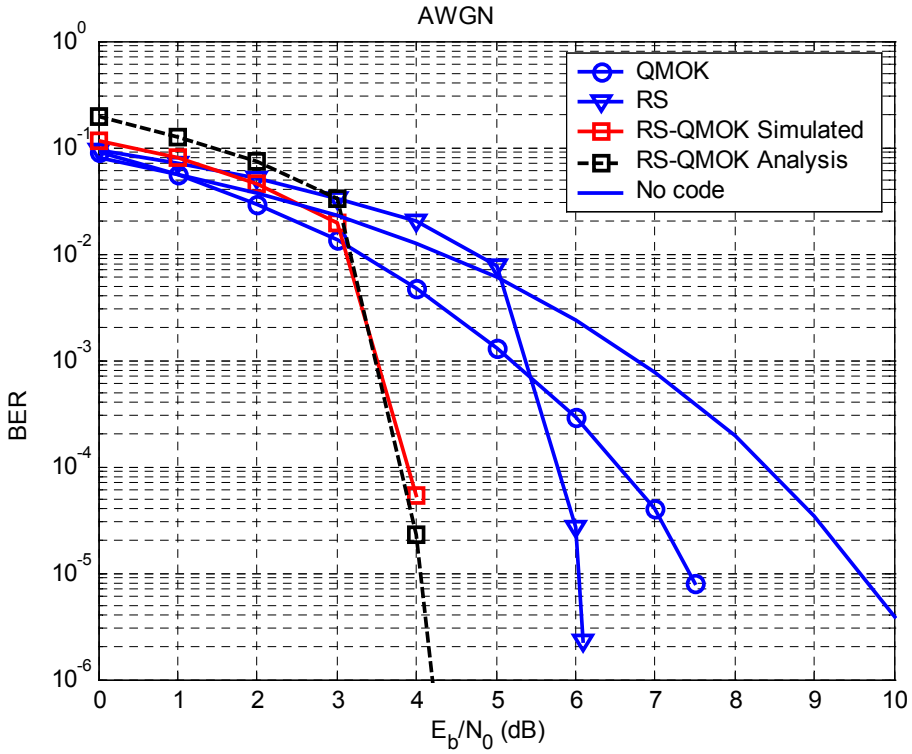

Figure 6.6 – BER performance of RS-QMOK code in AWGN channel

At BER=10^{-5}, RS-QMOK is able to achieve a coding gain of 5.5dB over an uncoded system. With the two codes concatenated, the inner code is efficient even at low SNR, helping to bring the BER curve to the "plunge point" of the RS code earlier. The RS-QMOK performance in a practical UWB channel will be presented in the next section.

6.2 Simulation Results and Discussions for RS-QMOK Code

The performance of the proposed coding method in multi-band UWB was investigated through extensive simulation studies. The performance of the proposed RS-QMOK code was simulated in Mode A of CM1, using QPSK modulation. This mode was chosen as it did not suffer from ISI (Table 5.2). Since ISI was absent, there was no difference between using a RAKE receiver or MMSE equalizer (Section 5.2.3). RAKE receiver was chosen, and perfect channel estimation and acquisition was assumed to simplify analysis.

As stated in the opening section, the performance of the proposed RS-QMOK code was compared with a ½ rate convolutional code with $K_c = 7$. In one of the early direct-spread UWB (DS-UWB) proposals to the IEEE 802.15 WPAN High Rate Alternative PHY Task Group 3a, a punctured code based on a ½ rate CC of $K_c = 7$ was also used for coding [41]. It would commendable if the RS-QMOK code were to turn out to outperform an unpunctured version CC. Since both the inner and outer codes were linear, their implementation complexity was expected to be less than CC, hence a more power efficient and yet powerful solution.

In the simulations, both the interleaved and un-interleaved versions of the various codes were shown to investigate the effects of the interleaver on the bit error rate, followed by the performance study of single- and multi-streaming.

6.2.1 Bit Error Rate Comparison - RS-QMOK vs CC

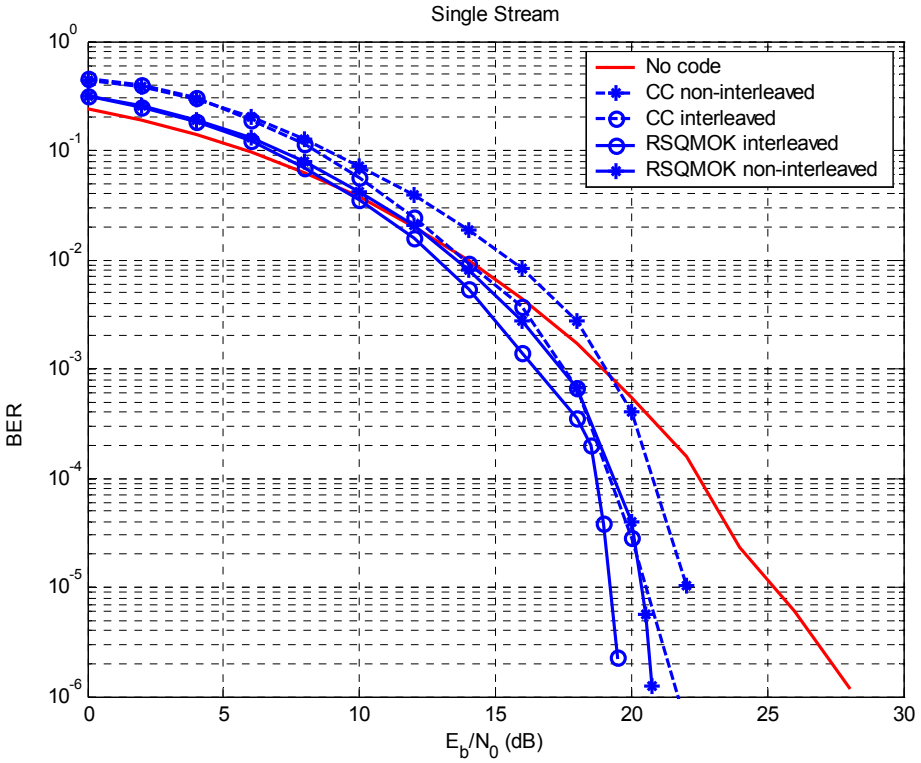

Figure 6.7 – BER comparison between RS-QMOK and CC in CM1 Mode A

Figure 6.7 shows the BER performance of RS-QMOK and CC. Coding gain was computed against an uncoded system at a BER of 10^{-5}, and is summarized in Table 6.3.

Table 6.3 –Coding gain of CC and RS-QMOK at BER of 10^{-5}

	CC	RS-QMOK
Un-interleaved	3.2dB	4.7dB
Interleaved	4.7dB	6.0dB

RS-QMOK managed a greater coding gain over CC. This performance gain was even more pronounced at lower BERs, because the RS-QMOK code reached its "plunge point" at 18dB. A closer look at Figure 6.7 revealed that RS-QMOK outperformed CC at all SNRs.

Another conclusion that could be drawn was that interleaving in a single-stream multi-band UWB implementation helped to decrease BER. With CC, interleaving gave an additional 1.5dB gain over an un-interleaved system at a BER of 10^{-5}. With RS-QMOK, the additional interleaving gain is only 1.3dB. This could be explained from the fact that Reed-Solomon codes and interleaving were both able to deal with burst errors. RS codes were capable of correcting burst errors by itself while an interleaver redistributed burst errors to become random errors for forward error correction. Therefore the benefit of interleaving was less pronounced in the proposed RS-QMOK scheme. Coding gain also came from frequency diversity. This means that if the channel conditions in a band were bad, rather than affecting many bits in a symbol, frequency diversity ensured that only one or two bits from the same symbol would be affected. This made error correction possible. The single-stream encode/decode chain was better to correct uniformly spaced symbol errors due to poor performance in particular sub-band, and this is demonstrated in Section 6.2.3.

6.2.2 Effects of Interleaving Pattern

In previous parts it has been shown that BER performance in single-stream multi-band UWB can be improved with interleaving. The interleaving pattern used is shown in Figure 6.8. Ideally, each bit should be allocated to a different sub-band, but since there were only 6 sub-bands for the 8 bits from each symbol, some bits are "spill-over". For example, the 1st bit of every symbol and the 2nd bit of certain symbols went into sub-band one.

Bits from n^{th} symbol	${}_nB_1$	${}_nB_2$	${}_nB_3$	${}_nB_4$	${}_nB_5$	${}_nB_6$	${}_nB_7$	${}_nB_8$

Figure 6.8 – Interleaving pattern used in Figure 6.7

The interleaving pattern shown in Figure 6.8 was regular, following a certain sequence. It may be possible that performance can be improved by randomizing this pattern, so that the "spill-over" bits were not adjacent to each other. The BER plots for other interleaving patterns, generated at random, are shown in Figure 6.9. It could be concluded from Figure 6.9 that the interleaving pattern did not influence the performance of the single-stream multi-band UWB system.

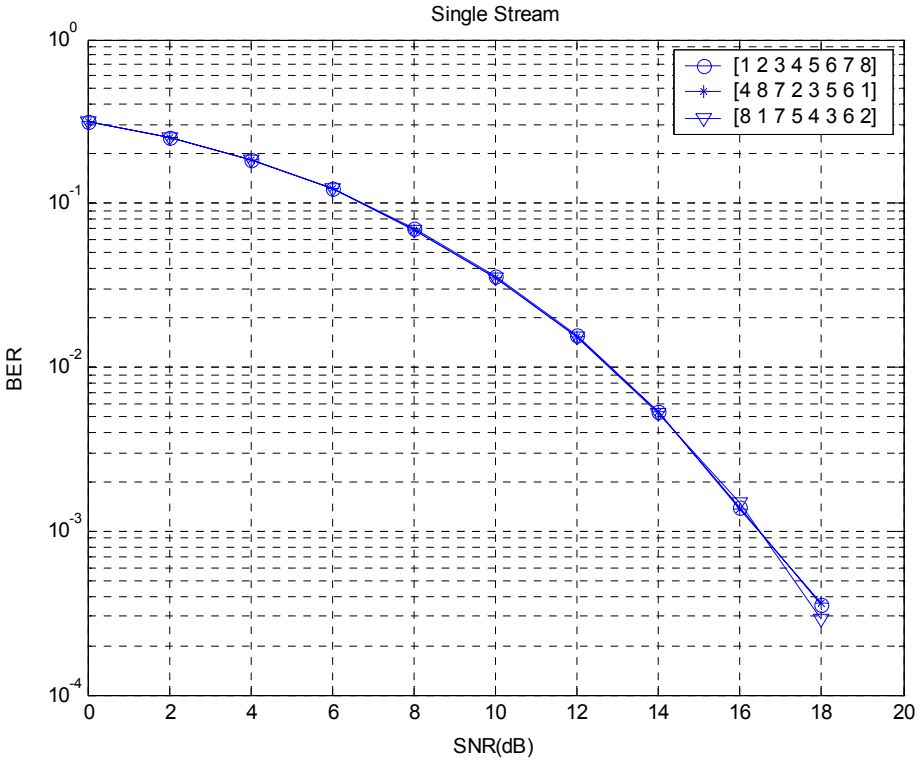

Figure 6.9 - BER of different interleaving patterns

6.2.3 Single-Streaming vs Multi-Streaming

After establishing the validity of RS-QMOK in terms of its BER, the performance of single-stream and multi-stream implementation was assessed next. The multi-stream performance with and without interleaving is shown in Figure 6.10.

Figure 6.10 shows that the interleaver did not have any effect on the BER performance for the multi-stream case. This was unlike the single-stream case when interleaving has a gain of about 1.3dB at a BER of 10^{-5} as shown in Table 6.3. This observation could be explained from the fact that in multi-stream implementation, interleaving did not distribute the bits from each symbol to different sub-bands. Interleaving merely rearranges the bits but they were still sent on the same sub-band. Therefore the advantage of frequency diversity observed in single-stream implementation was absent in the multi-stream case. At a BER of 10^{-5}, interleaved single-stream implementation had a coding gain of about 2.5dB over its multi-stream counterparts. Therefore single-stream is shown to be a better choice from the BER point-of-view.

However, multi-stream implementation of multi-band UWB is not without its merits. One argument for its deployment is its flexibility. Each band is self-contained, complete with its own coder, interleaver and decoder. In fact, multi-stream implementation can be considered as a few single-band UWB operating at different frequencies. Therefore, it is possible to create a multi-rate system, by using codes of different rates and modulation on each band.

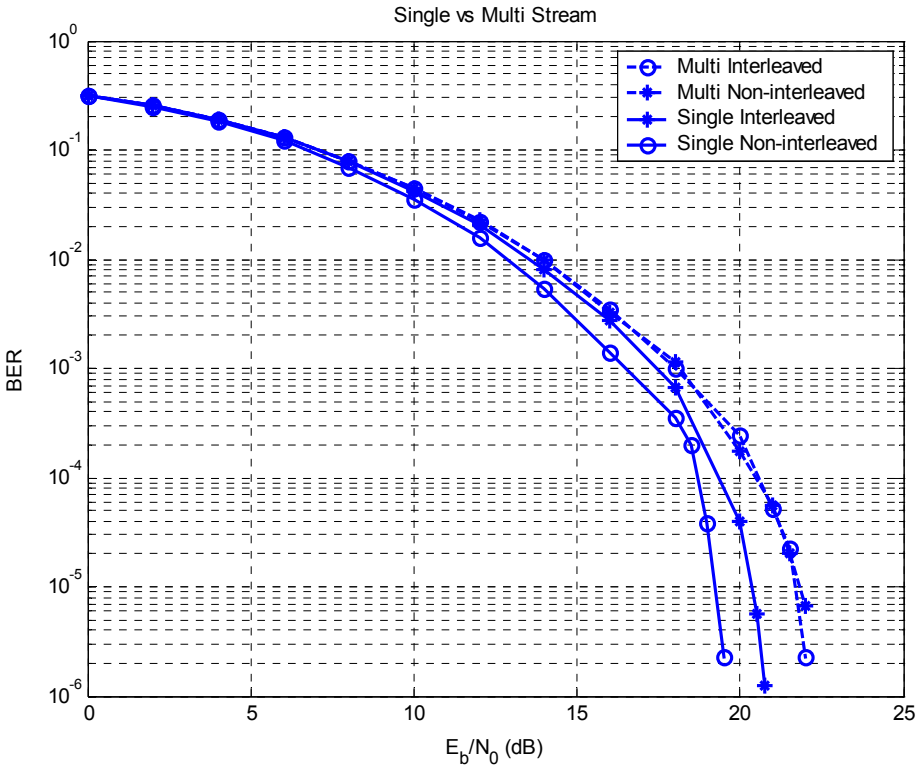

Figure 6.10 - BER of multi-stream implementation

6.2.4 Single-Streaming RS-QMOK Code in Various Channel Models

The performances of the proposed RS-QMOK code in CM1-CM4 are shown in Figure 6.11–Figure 6.14 respectively. Single-stream implementation was chosen so that interleaving can be used to bring about more coding gain. Both RAKE and over-sampling MMSE equalization were simulated. The proposed concatenated code with interleaving was shown to be able to improve performance that the asymptotic behavior observed in the RAKE receivers in Section 5.3 was all but eliminated except for CM4 Mode A. MMSE prevailed over RAKE receiver only in Mode A of CM3 and CM4, but gave little performance improvement in other modes and channel models. This brought to the conclusion that the RS-QMOK code compensated for almost all errors introduced by ISI in a single user environment.

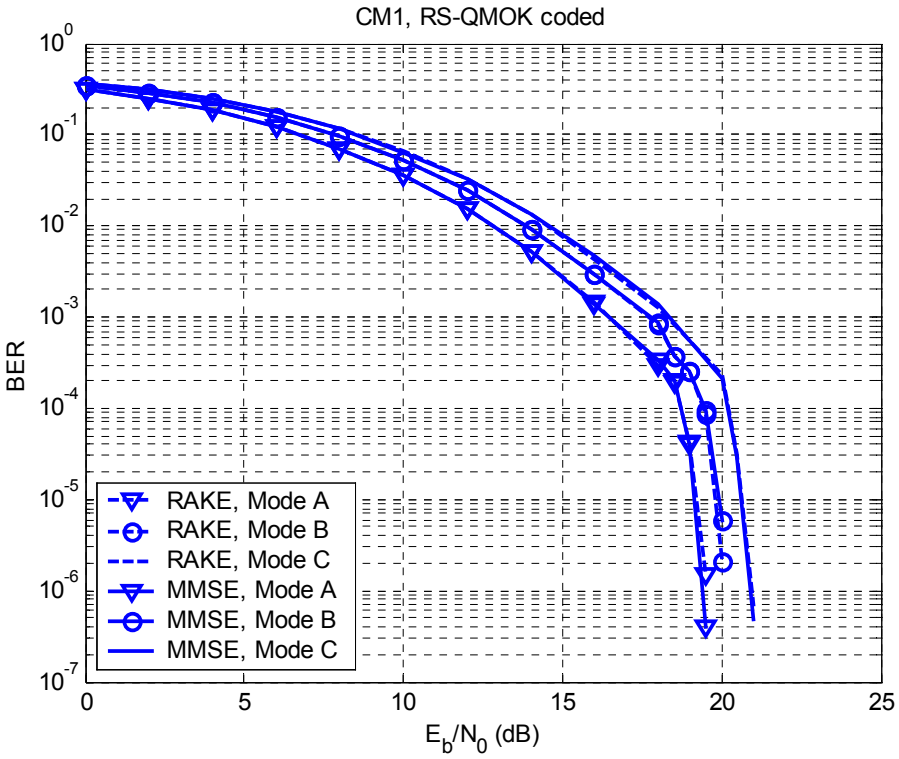

Figure 6.11 – RS-QMOK in various modes under CM1

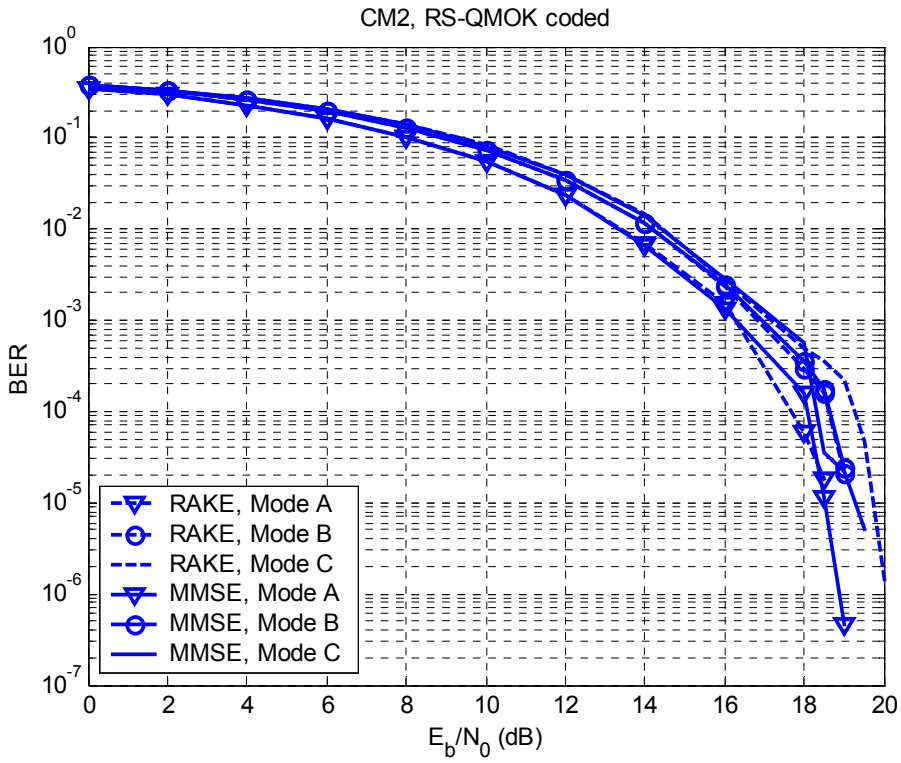

Figure 6.12 – RS-QMOK in various modes under CM2

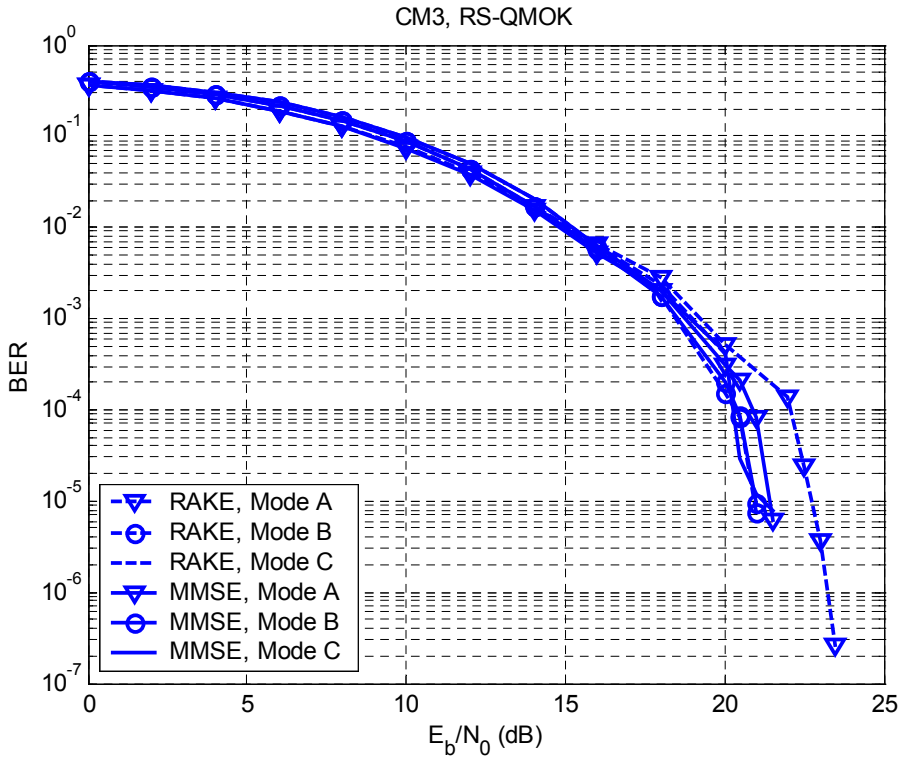

Figure 6.13 – RS-QMOK in various modes under CM3

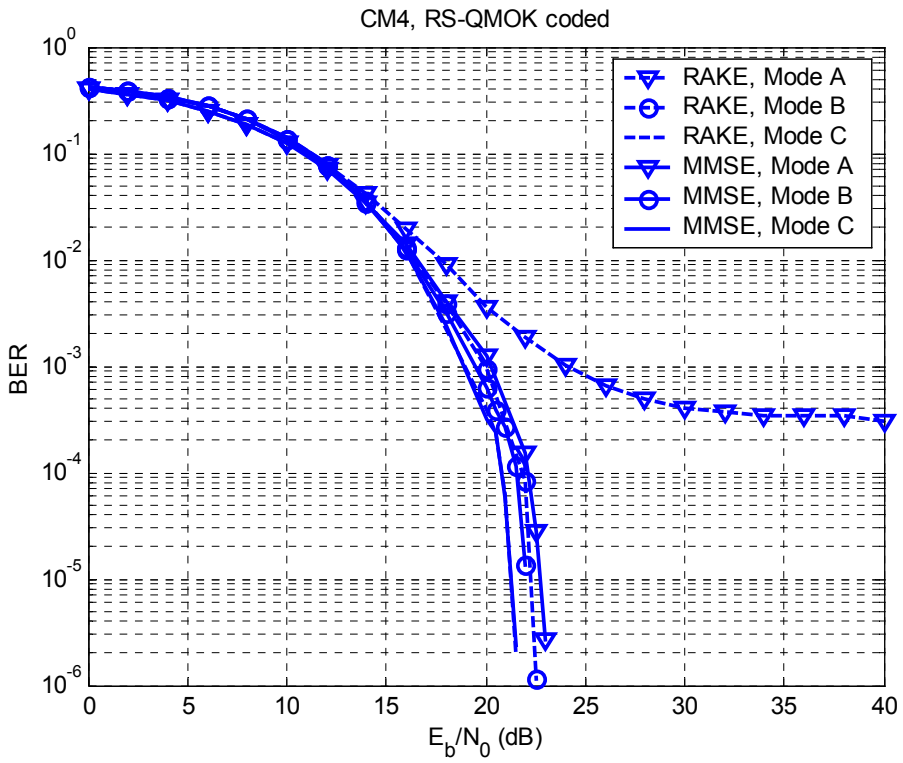

Figure 6.14 – RS-QMOK in various modes under CM4

The trade-off from the BER improvement of coding is a reduction in data rate. Table 6.4 records the data rate of the RS-QMOK coded system with QPSK modulation, based on the raw pulse rate in Table 2.2.

Table 6.4 –Data rate of the 3 modes after coding

Transmission Mode	Raw Pulse Rate (Mpps)	Coded QPSK Data Rate (Mbps)
A	308	267
B	154	133
C	77	67

6.3 Conclusion for Coding

In this chapter, a simplified coding scheme has been proposed using Reed-Solomon code as outer-code and Quadrature M-ary Orthogonal Keying (QMOK) as inner-code. Performance studies of a multi-band UWB system with the proposed coding scheme have been conducted. The proposed coding scheme makes the best use of bandwidth and complexity for multi-band UWB system. The results showed that the concatenation of RS and QMOK achieves better BER performance than convolutional code at all SNRs in QPSK modulation. The proposed coding scheme, being a concatenation of 2 linear block codes, was less complex and more power efficient than convolutional coding methods.

The interleaver in multi-band UWB was designed to ensure that the coded bits generated from one data bit are assigned to different bands so that frequency diversity could be achieved. Interleaving has been shown to achieve substantial BER improvement. On the other hand, the interleaving pattern was demonstrated to have no effect on the BER performance.

Furthermore, it has been shown that the single-stream implementation was superior to its multi-stream counterparts in terms of BER. In multi-stream, frequency diversity could not be exploited, as the interleaver merely rearranges the bits to be sent on the same band. However, multi-stream implementation was a more flexible scheme and was able to support a multi-rate system.

Finally, the RS-QMOK code has been shown to be able to correct almost all errors introduced by ISI. The performance gain by coding was considerable, to the effect that the multi-channel over-sampling MMSE equalizer had leverage over RAKE receiver only in Mode A of CM3 and CM4. This coding gain was achieved with a slight reduction in data rate.

The results in this chapter have been based on a single user multi-band UWB system, and can be somewhat ideal. In view of this the effectiveness of the proposed coding and equalization in a multi-user scenario is presented in the next chapter.

Chapter 7 Multi-User Performance

This chapter investigates the performance of the proposed receiver and coding scheme in a multi-user environment. The discussion centers on time-frequency code collision, in which 5 scenarios can be considered. The collision situations are illustrated in Figure 7.1(a)-(e).

In 1 x N collision in Figure 7.1(a), there is one full collision in each sub-band. Therefore collision occurs at one PRI with every simultaneously operating piconet (SOP). In B x 1 collision in Figure 7.1(b), each SOP suffers from at most one collision at each transmit instance. The worst-case scenario is depicted in B x N collision in Figure 7.1(c). The B x $^1/_2$ collision in Figure 7.1(d) arises from the multipath components that remain after one PRI by the interfering SOPs. Similarly, B x $^1/_3$ collision in Figure 7.1(e) depicts the interference that results from the SOPs after two PRIs.

The analysis and the simulation results of multi-band UWB in these multi-user scenarios are given in Sections 7.1 and 7.2 respectively.

Piconet	Reference	1	2	3	4	5	6
	#1	1	3	5	6	2	4
	#2	1	4	6	5	3	2
	#3	1	5	4	2	6	3

(a) – 1 x N, full collision from all users at one of the sub-bands

Piconet	Reference	1	2	3	4	5	6
	#1	1	3	5	6	2	4
	#2	5	4	2	1	3	6
	#3	4	2	6	3	1	5

(b) – B x 1, at most one collision in each sub-band

Piconet	Reference	1	2	3	4	5	6
	#1	1	2	3	4	5	6
	#2	1	2	3	4	5	6
	#3	1	2	3	4	5	6

(c) – B x N, full collision in every sub-band

Piconet	Reference	1	2	3	4	5	6
	#1	2	3	4	5	6	1
	#2	2	3	4	5	6	1
	#3	2	3	4	5	6	1

(d) – B x $^1/_2$, "half"-collision in every sub-band

Piconet	Reference	1	2	3	4	5	6
	#1	3	4	5	6	1	2
	#2	3	4	5	6	1	2
	#3	3	4	5	6	1	2

(e) – B x $^1/_3$, "one-third" collision in every sub-band

Figure 7.1 – Different time-frequency collision patterns

7.1 Analysis for Multi-User Collision

As seen from Figure 7.1(a)-(e), multi-user collision can be considered as a special case of ISI. The interference comes from other piconets, instead of from the different symbols. To compare and predict the performance of different scenarios without elaborate mathematics, a measure of multi-user interference I_{MU} is proposed, and is given by

1 x N: $$I_{MU} = 1 \cdot N_P \cdot (N_{ISI} + 1) \quad (7.1)$$

B x 1: $$I_{MU} = 1 \cdot N_P \cdot (N_{ISI} + 1) \quad (7.2)$$

B x N: $$I_{MU} = 6 \cdot N_P \cdot (N_{ISI} + 1) \quad (7.3)$$

B x ½: $$I_{MU} = 6 \cdot N_P \cdot (N_{ISI} + 1) \cdot 1/2 \quad (7.4)$$

B x ⅓: $$I_{MU} = 6 \cdot N_P \cdot (N_{ISI} + 1) \cdot 1/3 \quad (7.5)$$

where in (7.1)-(7.5), N_P stands for the number of interfering piconets, and N_{ISI} is defined as (5.1). Though the higher the value of I_{MU}, the more severe is the multi-user interference, it should be noted that it is a simplified indicator of interference. Other factors such as SIR also influence MAI performance.

7.2 Simulation Results and Discussion for Multi-User Performance

Extensive simulations has been conducted to investigate the multi-user performance with RS-QMOK coding and over-sampling MMSE equalization. RAKE receiver was simulated also for comparison. Due to the many permutations that were possible between the reference channel models and the interfering channel models, the reference piconet was assumed to be transmitting in Mode B of CM3. This transmission mode was chosen because from Figure 5.4 and Figure 6.13, it could be seen that it was sensitive to ISI, and hence to interference also. Any excessive SOP interference that cannot be mitigated by coding and equalization would turn up in this mode as an asymptotic error floor.

From Table 5.2, N_{ISI} = 0 (CM1 and CM2) or 2 (CM3 and CM4) only when transmitting in Mode B, hence the resulting I_{MU} corresponding to N_{ISI} = 0 and N_{ISI} = 2 is tabulated in Table 7.1 and Table 7.2 respectively.

Table 7.1 –I_{MU} of the various collision scenarios for N_{ISI}=0

	I_{MU} (N_{ISI}=0)				
N_P	1 x N	B x 1	B x N	B x ½	B x ⅓
1	1	1	6	3	2
2	2	2	12	6	4
3	3	3	18	9	6

Table 7.2 –I_{MU} of the various collision scenarios for N_{ISI}=2

	I_{MU} (N_{ISI}=2)				
N_P	1 x N	B x 1	B x N	B x ½	B x ⅓
1	3	3	18	9	6
2	6	6	36	18	12
3	9	9	54	27	18

The SIR was chosen to be at 0dB. The simulations started with a single interfering piconet, and then increased to two and three SOPs. The performance comparison among the various collision situations would be qualitatively explained based on Equations (7.1)-(7.5).

7.2.1 Performance With One Interferer

With one SOP operating $N_P = 1$, the case for '1 x N' was identical to that for 'B x 1' i.e. both having one TF collision. Therefore, their performances were expected to be identical. The simulated results for RAKE receiver with RS-QMOK coding in CM1-4 are shown in Figure 7.2-Figure 7.5 respectively.

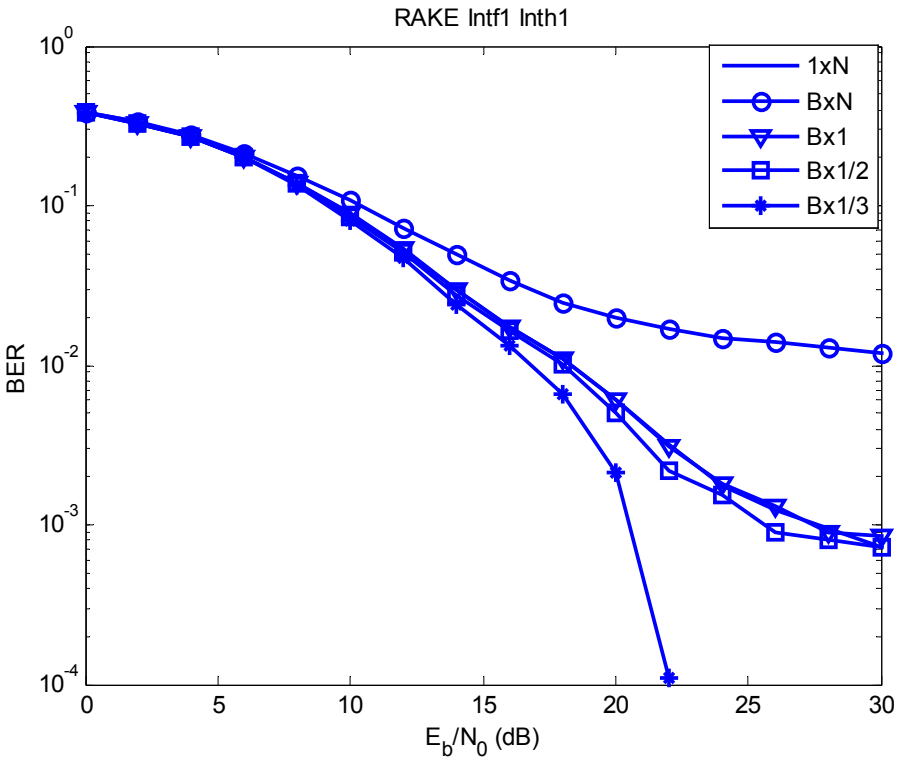

Figure 7.2 – BER performance with 1 SOP in CM1 for RAKE receiver

In Figure 7.2, 'B x N' had the worst BER performance while 'B x $^1/_3$' had the best. The other 3 scenarios gave almost identical results. All collisions types exhibited error floors except 'B x $^1/_3$'.

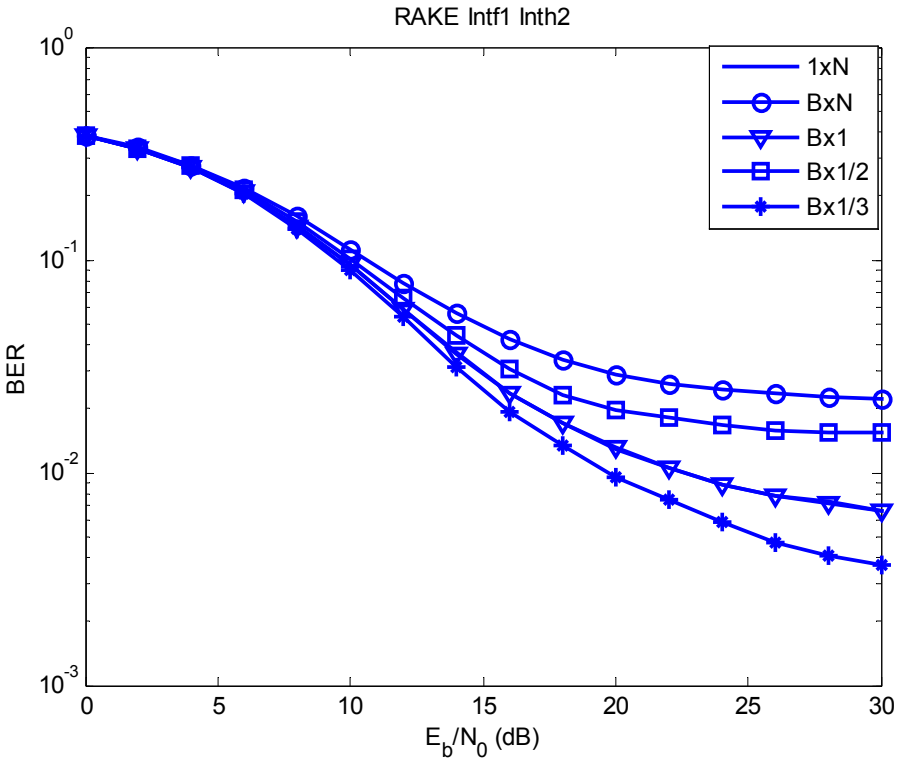

Figure 7.3 – BER performance with 1 SOP in CM2 for RAKE receiver

In Figure 7.3, again 'B x N' gave the worst performance, and the curve for '1 x N' was identical to that of 'B x 1' as expected. Asymptotic error floors were observed in all collision curves, even for 'B x $^{1}/_{3}$' that gave the best performance in Figure 7.2.

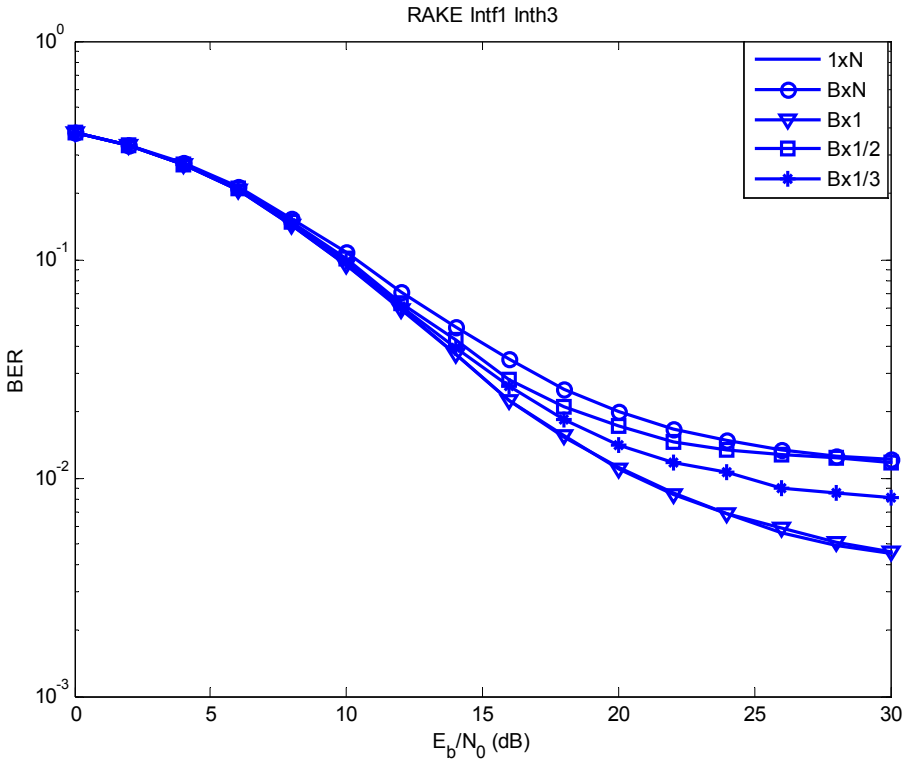

Figure 7.4 – BER performance with 1 SOP in CM3 for RAKE receiver

In Figure 7.4, the curves for '1 x N' and 'B x 1' performed identically as expected, since they suffer the same amount of collision with $N_P = 1$. All curves showed asymptotic error floors of various degrees.

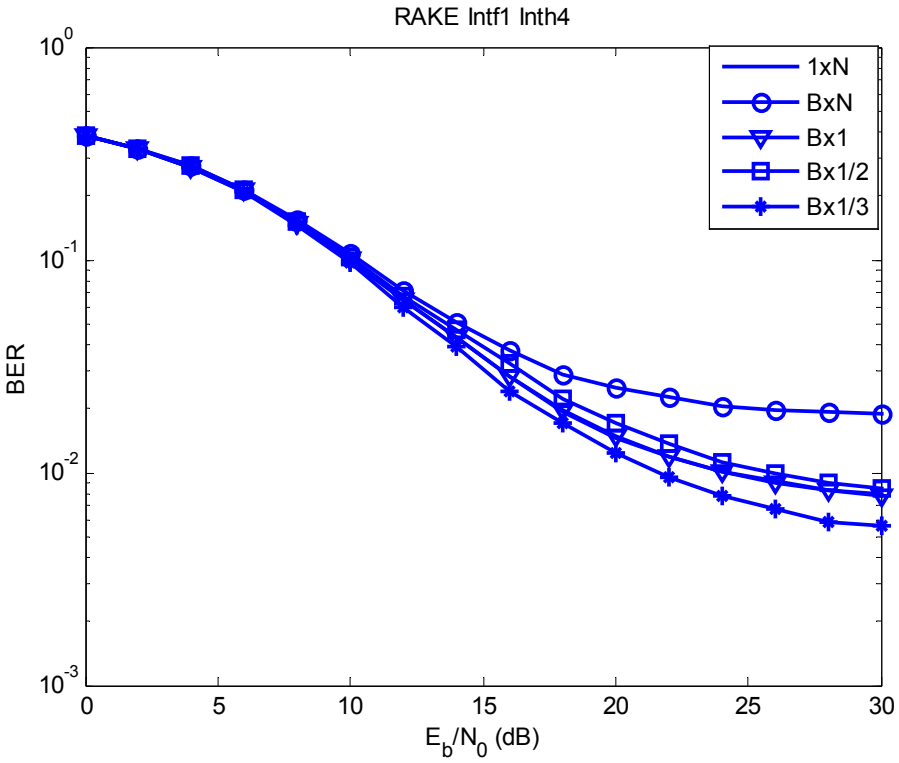

Figure 7.5 – BER performance with 1 SOP in CM4 for RAKE receiver

In Figure 7.5, simulation shows that the curves for '1 x N' and 'B x 1' were identical as expected. The worst performance came from 'B x N' and the best from 'B x $^{1}/_{3}$'. From the previous figures, it could be seen that RAKE was not adequate in mitigating for multi-user interference, as error floors of different severity were observed even with coding. With this in mind, the simulation for over-sampling MMSE equalization followed, and the results for CM1-4 are shown in Figure 7.6 - Figure 7.9.

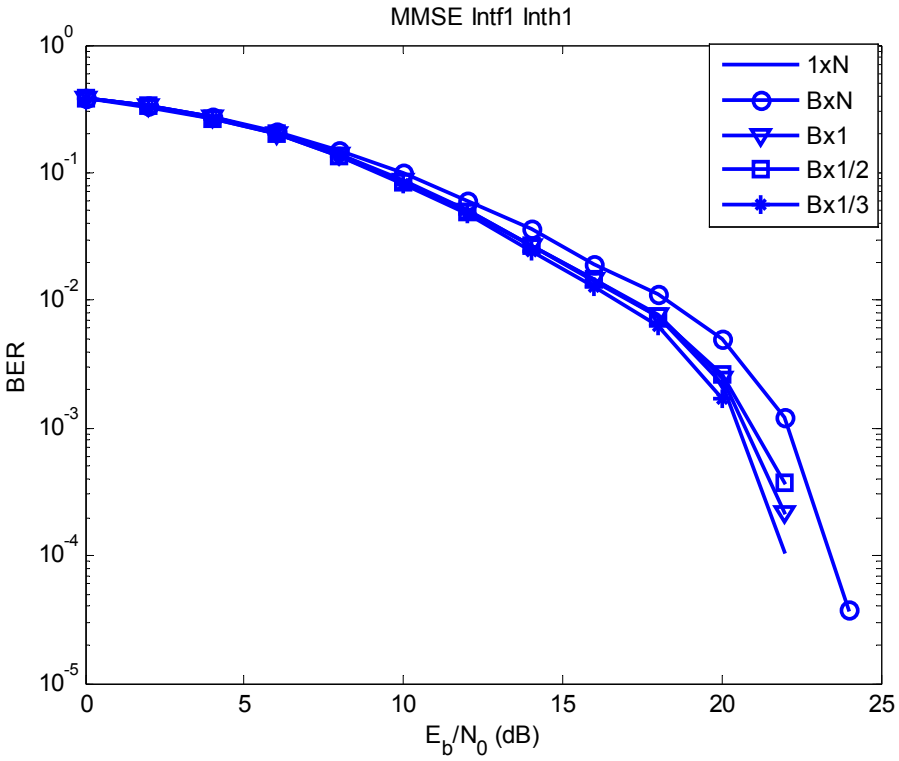

Figure 7.6 – BER performance with 1 SOP in CM1 for MMSE receiver

The simulated curves for all the various collision cases in Figure 7.6 were close to each other, except for 'B x N'. This could also be predicted from the first row of Table 7.1, as the I_{MU} values for '1 x N', 'B x 1', 'B x 1/3' and 'B x 1/2' differ from each other by a small amount.

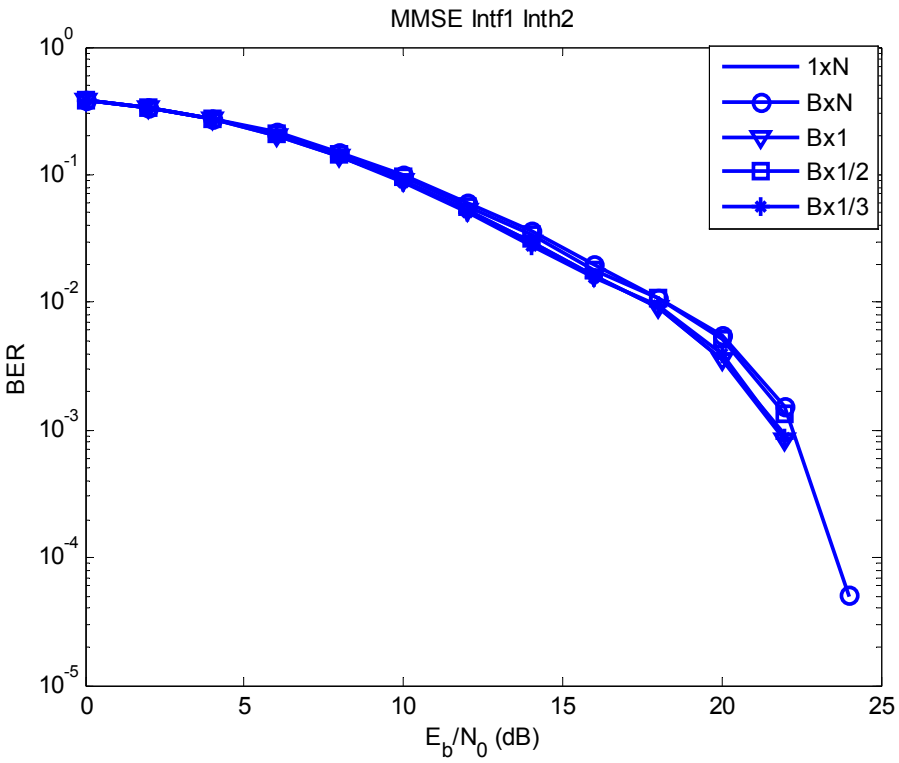

Figure 7.7 – BER performance with 1 SOP in CM2 for MMSE receiver

The curves in Figure 7.7 were also close to each other, even so for 'B x N' case. This shows that coded over-sampling MMSE equalizer was effective in countering the multi-user artifacts in this particular interference model. At high SNR, the curve for 'B x N' is observed to perform worse than the rest, as it registered a data point at E_b/N_0 = 24dB while the rest of the curves did not.

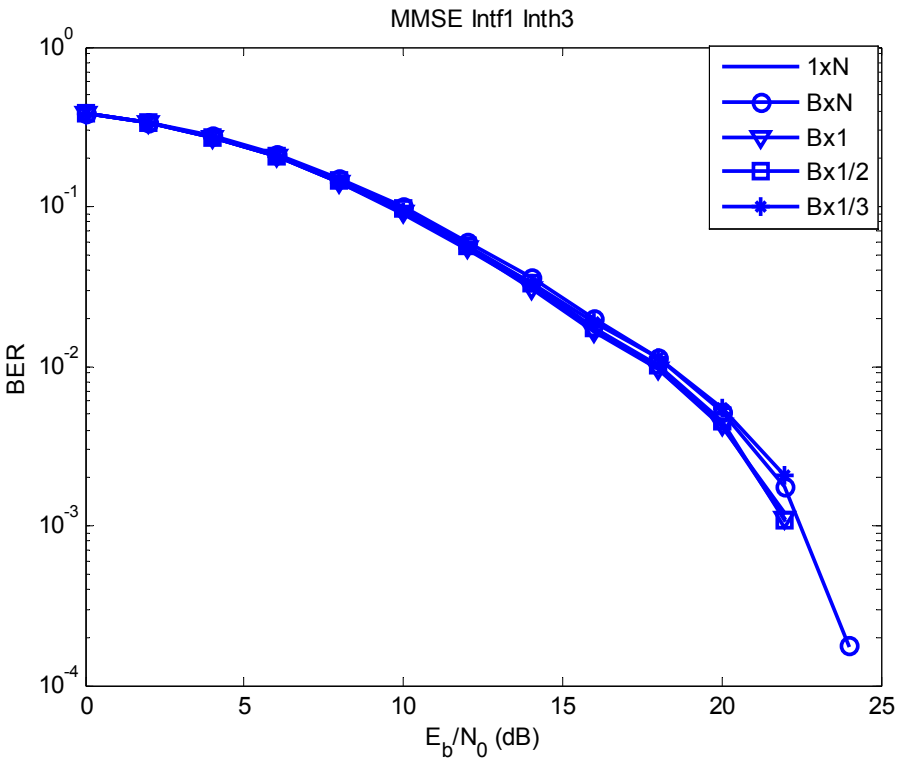

Figure 7.8 – BER performance with 1 SOP in CM3 for MMSE receiver

Under CM3 in Figure 7.8, the performances of all the collision scenarios were similar. Again coded over-sampling MMSE equalizer is effective in countering MAI from CM3, and 'B x N' performed slightly worse than others as it has a data point at E_b/N_0 = 24dB.

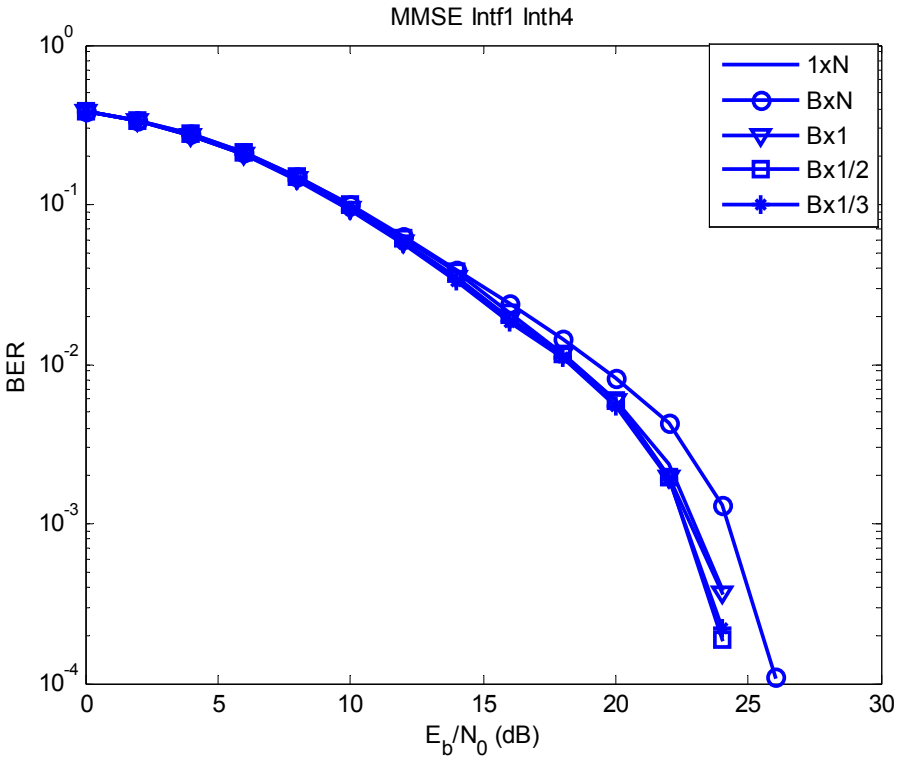

Figure 7.9 – BER performance with 1 SOP in CM4 for MMSE receiver

In Figure 7.9, similar observations to Figure 7.6 could be made. Only 'B x N' case gave a slightly worse performance. From Figure 7.6 to Figure 7.9, the coded over-sampling MMSE equalizer showed no error floor at any collision scenario, and hence is superior to RAKE receiver in handling MAI.

7.2.2 Performance With Two Interferers

From Section 7.2.1 it has been shown that RAKE receiver was inadequate in dealing with MAI even with N_p=1. Hence the simulations for N_p=2 and 3 were conducted only for coded over-sampling MMSE equalizer. The results of 2 SOPs operating in CM1-4 are shown in Figure 7.10-Figure 7.13 respectively. In this case, the collision scenarios for '1 x N' and 'B x 1' were no longer identical.

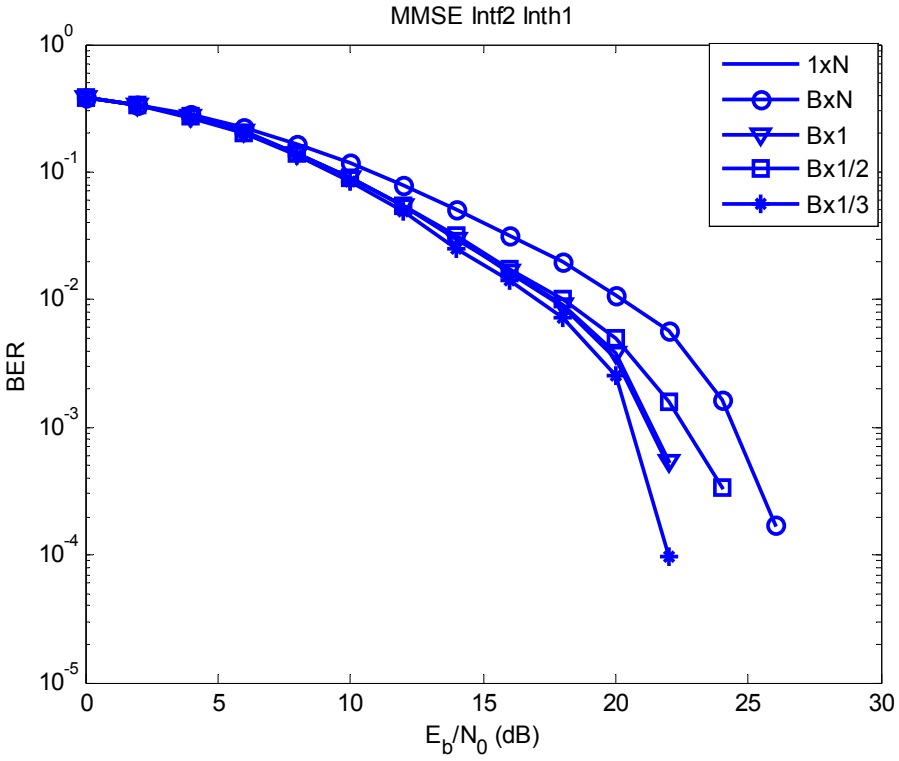

Figure 7.10 – BER performance with 2 SOPs in CM1 for MMSE receiver

In Figure 7.10, 'B x $^1/_3$' gave the best performance, followed by 'B x 1', '1 x N', 'B x $^1/_2$' and 'B x N' performing the worst. Using the I_{MU} values in row 2 of Table 7.1, the order of the various collision scenarios could be predicted except for 'B x $^1/_3$'.

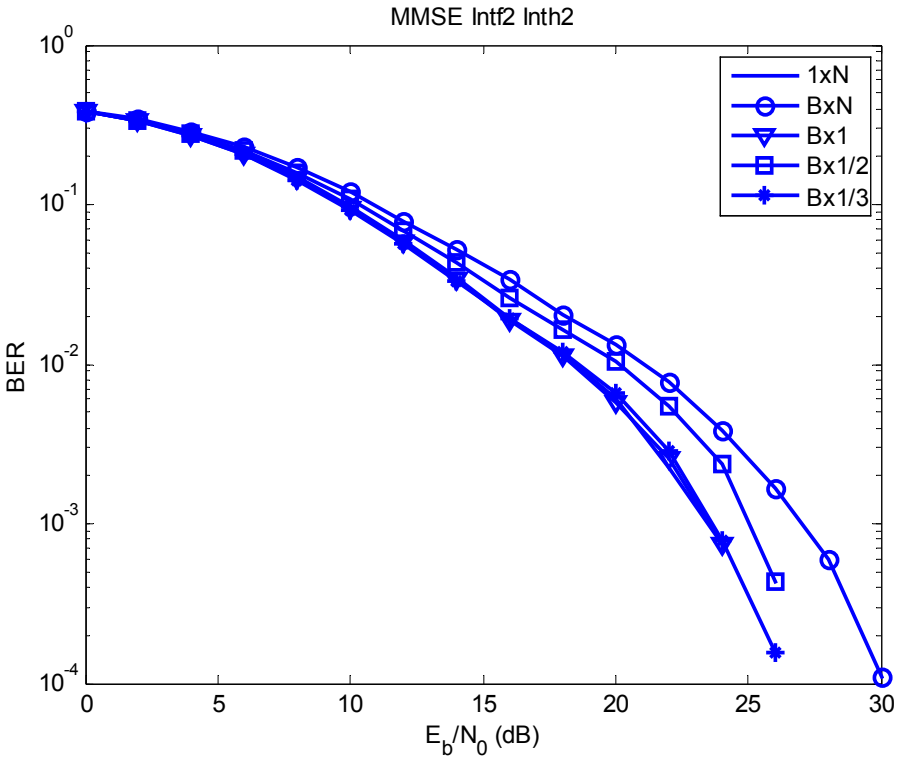

Figure 7.11 – BER performance with 2 SOPs in CM2 for MMSE receiver

Again, using the second row of Table 7.1, the observation in Figure 7.11 could be explained to a certain extent. 'B x N' and 'B x ½', having the largest I_{MU} values, performed worst. The other 3 curves were very close to each other.

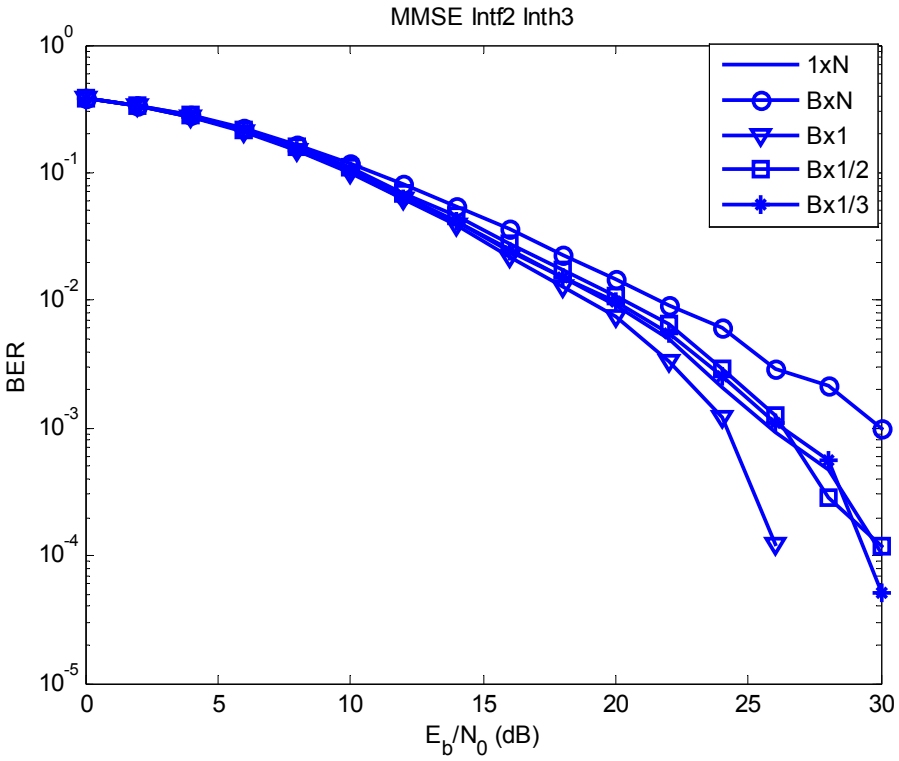

Figure 7.12 – BER performance with 2 SOPs in CM3 for MMSE receiver

The behavior of Figure 7.12 followed the I_{MU} values in the second row of Table 7.2 to a certain degree. The best and the worst performance curves, namely 'B x 1' and 'B x N', were both having the smallest and largest I_{MU} values respectively. The other 3 scenarios are close to each other.

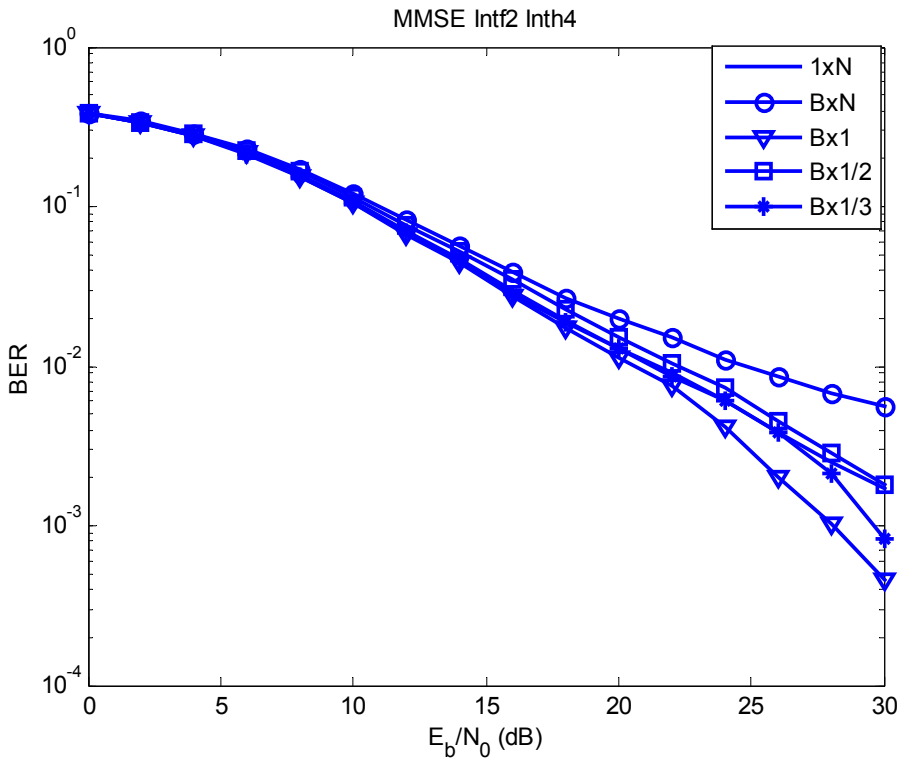

Figure 7.13 – BER performance with 2 SOPs in CM4 for MMSE receiver

Observations similar to Figure 7.12 could be made in Figure 7.13, when the interferers were operating in CM4, with 'B x 1' performing the best while 'B x N' performing the worst. The other cases are gave similar performance.

7.2.3 Performance With Three Interferers

The simulations then proceeded with 3 interferers, $N_P = 3$. The results for 3 SOPs in CM1-4 are shown in Figure 7.14-Figure 7.17 respectively.

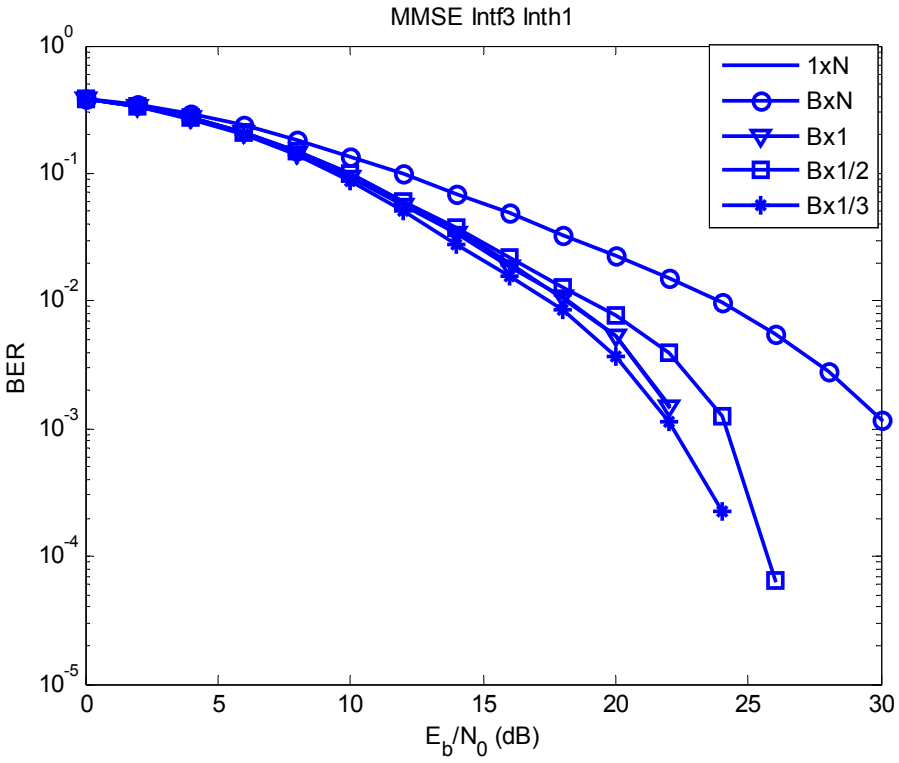

Figure 7.14 – BER performance with 3 SOPs in CM1 for MMSE receiver

From Figure 7.14, the best scenario appeared to be 'B x $^1/_3$', while '1 x N' and 'B x 1' gave the same performance, followed by 'B x $^1/_2$' and 'B x N' performing the worst. These results followed the third row of Table 7.1, except for the case of 'B x $^1/_3$'.

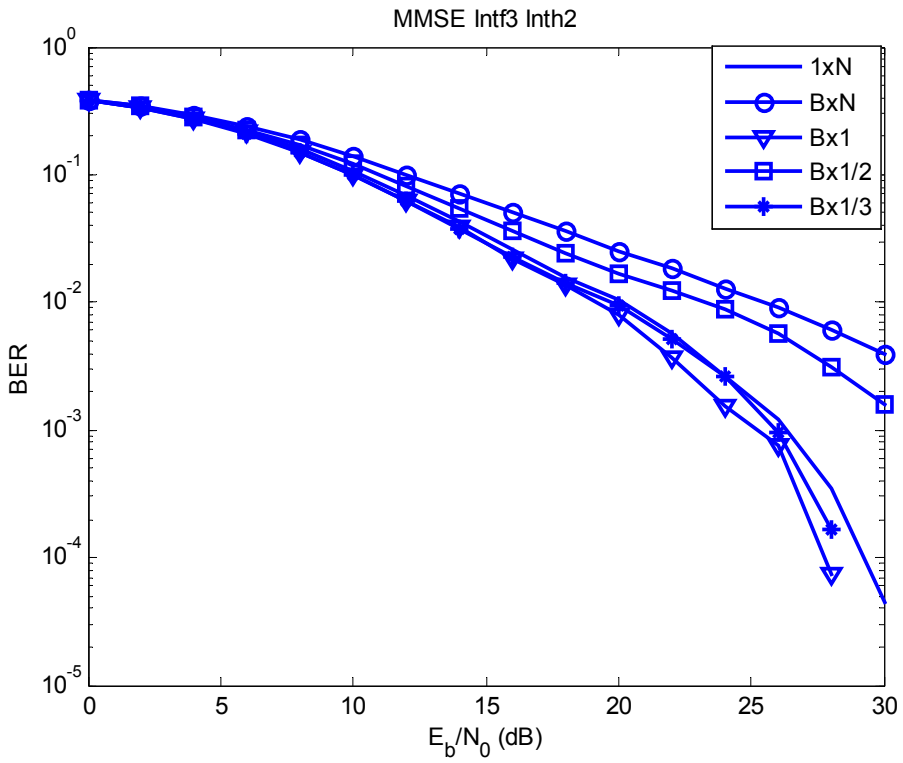

Figure 7.15 – BER performance with 3 SOPs in CM2 for MMSE receiver

The predictions from Table 7.1 were more accurate when applied to the plots in Figure 7.15. 'B x 1' appeared to perform best, followed by 'B x $^1/_3$', '1 x N', 'B x $^1/_2$' and with 'B x N' performing the worst.

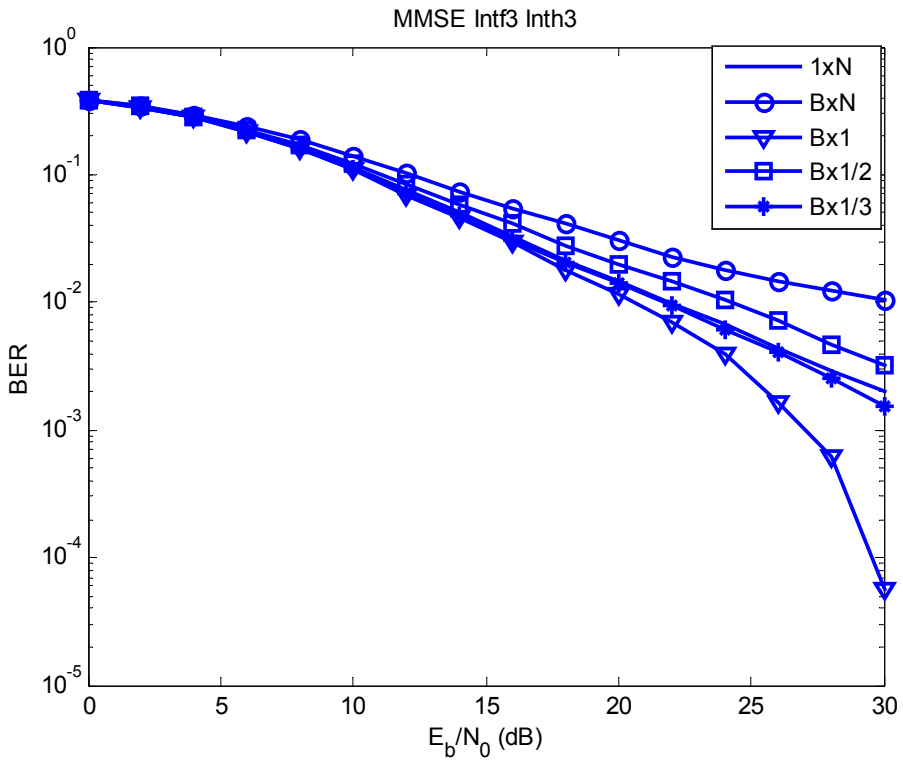

Figure 7.16 – BER performance with 3 SOPs in CM3 for MMSE receiver

Similar observations as Figure 7.15 can be made for Figure 7.16, which appears to comply with Table 7.1. The performance curves, ranking from best to worst, are: 'B x 1', 'B x ⅓', '1 x N', 'B x ½' and 'B x N'.

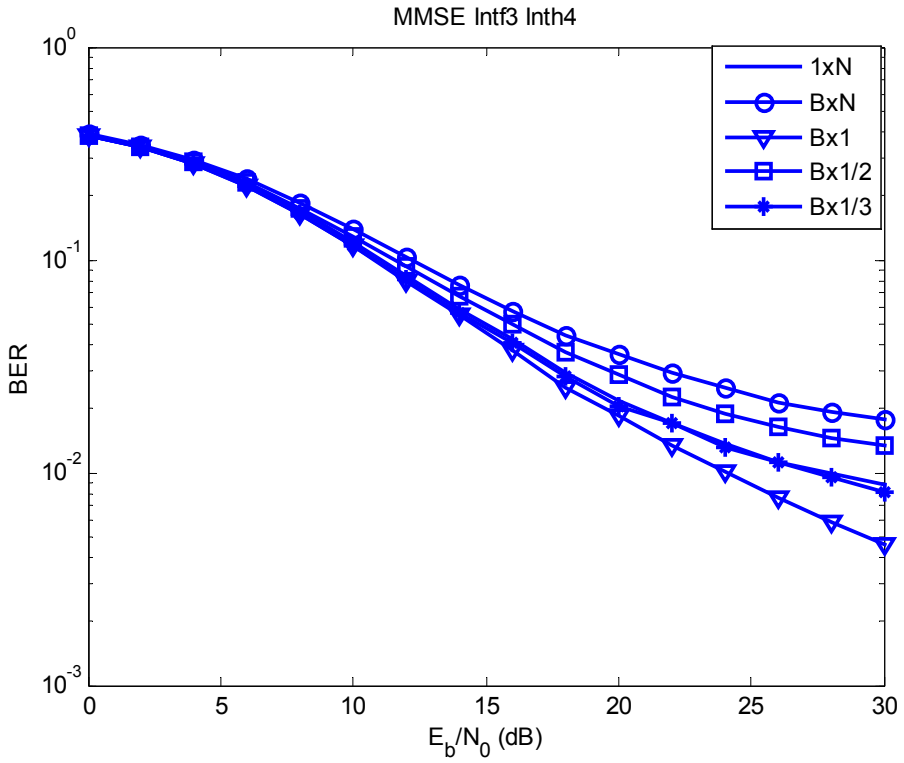

Figure 7.17 – BER performance with 3 SOPs in CM4 for MMSE receiver

In Figure 7.17, coded MMSE started to display asymptotic behavior at high SNR. However, this should not disavow the use of the over-sampling MMSE equalizer, because the simulations so far have been based on a rather pessimistic case of SIR=0dB for every SOP. An SIR=10dB for each of the 3 SOPs in CM4 is shown in Figure 7.18 for comparison with Figure 7.17.

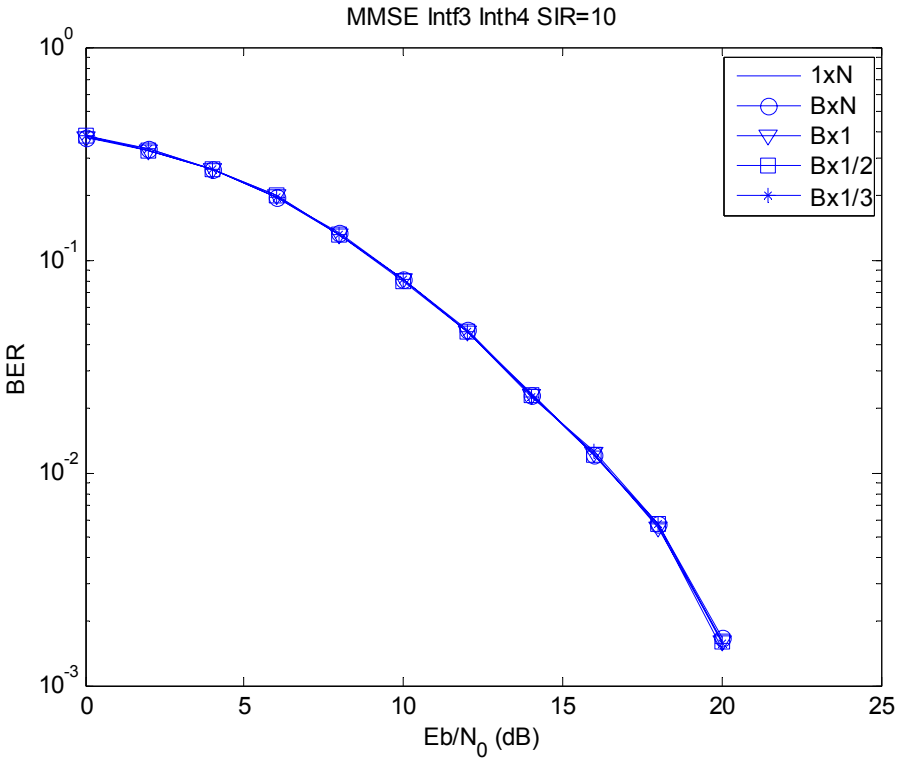

Figure 7.18 – BER performance with 3 SOPs in CM4 for MMSE receiver, SIR=10dB

From Figure 7.18, it could be observed that the over-sampling MMSE equalizer is able to alleviate the adverse consequences of multi-user interference at SIR=10dB.

7.3 Conclusion for Multi-User Performance

It has been shown in this chapter through extensive simulations that coded over-sampling MMSE equalizer is capable of mitigating for at least 3 simultaneously operating piconets with SIR = 0dB. Though coded RAKE receiver has been shown to give comparable performance as MMSE equalizer in the single user case in Chapter 6, it was shown not useful to handle even 1 interferer. It is therefore prudent to employ MMSE equalizer for multi-band UWB systems, since they are expected to operate in multi-user environments.

Five collision scenarios have been considered in the simulations, with different degrees of multi-user interference. In order to simplify analysis, multi-user interference was treated as a special case of inter-symbol interference. Different collision situations were compared by a collision metric I_{MU}. It depended on the number of users, number of bands in collision and also on the length of channel under inter-symbol interference. It has been shown that the I_{MU} values were able to predict the relative performance of the different collision scenarios quite accurately.

From the simulations with different number of SOPs, it has been shown that the band assignment 'B x 1' consistently gave relatively good BER performance. This could be deduced from the I_{MU} calculations also. This fact can be used to aid the SOPs to co-ordinate their TF band assignment. The best case scenario is of course for there to be no collision among the piconets. However through the investigations in this chapter it is possible for the multi-band UWB systems to tolerate at most one collision in each

band, without too much performance degradation. It should be noted also that in most practical cases, the SIR would possibly not as severe as 0dB.

Lastly, the BER performance in multi-user environment was shown to be dependent on the channel model of the interfering SOPs, given that they were operating in the same SIR. This could be explained from the ISI point of view. In NLOS models such as CM3 and CM4, the N_{ISI} was larger and affects more symbols. Despite more severe MAI in NLOS interference channels, coded over-sampling MMSE equalizer has been shown to be able to handle the errors introduced by multi-user interference.

Chapter 8 Conclusion

Multi-band UWB system is an interesting proposal due to its adaptive nature and its ability to avoid narrowband interference. Channel characteristics for UWB system are unique and different from its narrowband counterparts, and the various channel properties have been detailed in the IEEE channel models, standardizing and simplifying analysis and simulation. It is in this light that this work has been produced, focusing on the design of multi-band UWB receiver that exploits the unique properties of the UWB system.

In order to maximize the adaptive nature of multi-band UWB system, 3 transmission modes have been proposed and employed throughout this work. These modes differ from each other in terms of PRI, trading-off between channel delay spread tolerance and data rate. The transmission mode to be used can be made dependent on the channel characteristics.

In this work, the major components in the multi-band UWB receiver have been investigated, namely the receive LPF design, acquisition, equalization, coding and lastly multi-user performance. These components can be found in Figure 1.1. Transmission in the different bands is done by switching, based on the TF code assigned to each transceiver.

The purpose of the LPF at the receiver is to filter off the unwanted high frequency components after down-conversion. To simplify the receiver design, it is important to engage a single LPF configuration that can be used for all the 6 transmission bands. To this end, two metrics have been used for LPF selection in Chapter 3: energy captured

and ratio statistics test. Energy captured helped to ensure that maximum energy was transmitted after low pass filtering without using a large passband, as it may admit more noise. Ratio statistics test was used to measure the correlation properties of the received signals, so that diversity could be achieved.

The results from Section 3.2 showed that a Chebychev 3rd order filter with $f_{pass} = 0.10$ was found to be suitable as the LPF for multi-band UWB receiver. This configuration had a good energy captured percentage with a relatively small f_{pass}, showed good correlation properties.

Rapid acquisition is crucial for high data rate applications such as multi-band UWB systems. In Chapter 4, a double-dwell parallel search correlator is proposed. It makes use of phase elimination, which is a unique feature for the acquisition of multi-band UWB systems at the receiver. The proposed acquisition structure was tested on 10 repetitions of Barker-4 sequences and 2 repetitions of CAZAC-16 sequences as preamble. Simulation using the proposed system showed that Barker-4 sequences was a more suitable choice as preamble. It had a low probability of false alarm and a reduced number of correlation operations required. Depending on the threshold set, a 50% reduction in the number of correlation operations was shown to be possible.

In Chapter 5, detailed analysis of the bit error rate performance of the various transmission modes has been presented. Different transmission mode is able to deal with ISI in varying degrees. Based on the 10dB maximum delay spread, the ISI suffered in the various modes can be computed. The amount of ISI has been shown to have a direct bearing on the BER performance. Presence of ISI causes severe BER

degradation. To counter such effects, multi-channel RAKE receiver and multi-channel MMSE equalizer with 4-times over-sampling were considered. Simulations studies have shown that a 4-tap over-sampling MMSE equalizer was better equipped in dealing with ISI than a 4-tap RAKE receiver. In severely ISI-corrupted cases, asymptotic error floors could be observed for RAKE receiver. over-sampling MMSE equalizer on the other hand was able to mitigate for the most ISI-laden channel model and transmission modes. Also, detailed theoretical analysis and comparison between MMSE and RAKE receiver has been presented.

In Chapter 6, a simplified coding scheme called RS-QMOK is proposed. This concatenated code consists of a RS outer code and a QMOK inner code. The proposed code is less complex than convolutional codes because both RS and QMOK codes are linear. Through simulations, it has been shown also that interleaved RS-QMOK code outperforms a length-7 half-rate interleaved convolutional code at all SNRs. The interleaving pattern has been shown to have no effects on the BER performance. The performance and the application of single- and multi-streaming has been presented and discussed also. Single-streaming had a better BER performance than multi-streaming due to frequency diversity. However, multi-stream implementation was a more flexible scheme and was able to support a multi-rate system. It was shown that the proposed code was very effective in reducing bit error rate in any channel model.

In Chapter 7, five multi-user TF collision scenarios have been presented. Each scenario has been simulated in the presence of 1 to 3 SOPs. The bit error rate was plotted in various interfering channel models with an SIR = 0dB at each SOP. The coded over-sampling MMSE equalizer has been found to be able to alleviate the effects of multi-

user collision, in any interfering channel model. Coded multi-channel over-sampling MMSE equalizer hence is shown not only be able to offset BER introduced by ISI, but reduce errors brought about by multi-user interference too. It was found that the proposed system is able to tolerate one collision per sub-band among all interfering users. This helps in terms the assignment of TF code among the SOPs, increasing the number of potential users that could be supported in a multi-band UWB system.

Despite the extensive results that have been presented, there are some areas pertaining to the receiver design that are not dealt with in this work and is left for future research. For example, perfect channel estimation has been assumed throughout. Estimation errors may induce severe BER degradation. Channel estimation is a great challenge in UWB systems due to its fine time resolution and the high data speed. This normally requires a very high sampling rate with high system complexity [43]. With multi-band, this task is made even more challenging, as channel estimation has to be carried out on every sub-band.

In addition to channel estimation, more detailed investigations can be made for multi-user analysis. For example, the interfering SOPs can each operate in different collision scenarios, in various distances and SIRs from the reference piconet. This will be a more accurate simulation of multiple access interference in a practical situation.

In the final analysis, the pertinent aspects of the multi-band UWB receiver have been presented. The overall design takes advantage of certain UWB channel characteristics. The resulting receiver design is one with rapid acquisition, high coding gain and good multi-user performance by using over-sampling MMSE equalization.

References

[1] FCC 02-48 First Report and Order In the Matter of Revision of Part 15 of the Commission's Rules Regarding Ultra-Wideband Transmission Systems, adopted Feb. 14, 2002.

[2] Siwiak, K., "Ultra-wide band radio: introducing a new technology**",** *VTC 2001 Spring. IEEE VTS 53rd*, 6-9 May 2001 pp:1088 - 1093 vol.2

[3] Win, M.Z., Scholtz, R.A. "Impulse radio: how it works**",** *Comms. Letters, IEEE*, Vol 2 , Issue 2 , Feb. 1998 pp 36 – 38

[4] Woo Cheol Chung, Dong Sam Ha "On the performance of bi-phase modulated UWB signals in a multipath channel**",** *VTC 2003-Spring. The 57th IEEE Semiannual*, Vol 3 , 22-25 April 2003 pp:1654 - 1658

[5] Huaping Liu, "Error performance of a pulse amplitude and position modulated ultra-wideband system over lognormal fading channels**",** *Comms. Letters, IEEE*, Vol. 7 , Issue 11 , Nov. 2003 pp:531 – 533

[6] D. Barras, F. Ellinger and H. Jackel, "A Comparison between Ultra-Wideband and Narrowband Transceivers," *TRLabs/IEEE Wireless 2002,* Calgary, pp. 221-214, Jul 2002.

[7] Molisch, A.F., Foerster, J.R., Pendergrass, M., "Channel models for ultrawideband personal area networks**",** *Wireless Communications*, IEEE, Volume: 10 , Issue: 6 , Dec. 2003 Pages:14 – 21

[8] Baccarelli, E., Biagi, M., Taglione, L., "A novel approach to in-band interference mitigation in ultra wideband radio systems", *Ultra Wideband Systems and Tech., 2002. Digest of Papers. 2002 IEEE Conf.*, pp 297-301

[9] Borah, D.K., Jana, R., Stamoulis, A., "Performance evaluation of IEEE 802.11a wireless LANs in the presence of ultra-wideband interference", *Wireless Comms. and Networking, 2003. WCNC 2003,* 2003 IEEE , Vol 1, pp 83-87

[10] V.S. Somayazulu, J.R.Forester, S. Roy. "Design Challenges for Very High Rate UWB Systems" *Intel Tech. Papers,* (http://www.intel.com/technology/ultrawideband/downloads/Asilomar_2002_final.pdf)

[11] Win, M.Z., Scholtz, R.A., Barnes, M.A., "Ultra-wide Bandwidth Signal Propagation for indoor wireless communications", *Comms., 1997. ICC 97*

Montreal, 'Towards the Knowledge Millennium'. 1997 IEEE International Conf. on, Vol 1 , 8-12 June 1997 Pages:56 - 60 vol.1

[12] Win, M.Z., Scholtz, R.A., "On the energy capture of ultrawide bandwidth signals in dense multipath environments," *IEEE Comms. Lett.,* Vol 2, Sept 1998, pp 245-247

[13] R. J. Cramer, M. Z. Win, and R. A. Scholtz, "Impulse radio multipath characteristics and diversity reception," in *Proc. 1998 ICC*, 1998, pp. 1650–1654.

[14] C. Surya, "Circuit Design- Chapter 1", http://www.eie.polyu.edu.hk/~ensurya/lect_notes/commun_cir/Ch1/Chapter1.htm

[15] Wong Sai Ho; Madhukumar, A.S.; Chin, F.; "Conventlonal quadrature mixer for impulse radio receivers- filter design issues**"** *PIMRC 2003. 14th IEEE Proceedings on*, Vol 3 , Sept. 7-10, 2003 pp 2716 - 2720

[16] J.K. Proakis, "Digital Communications", McGraw-Hill Inc., 4th ed., 2001

[17] A.J. Viterbi, "A Robust Ratio-Threshold Technique To Mitigate Tone And Partial Jamming In Coded MFSK Systems", *Proc. Milit. Commun. Conference*, p22.4.1-5, Oct 1982

[18] Homier, E.A.; Scholtz, R.A. **"**Rapid acquisition of ultra-wideband signals in the dense multipath channel"**,** *Ultra Wideband Sys. and Tech., 2002*. Digest of Papers. 2002 IEEE Conf. on, 2002

[19] Yao Ma, S. Pasupathyb, Francois Chin, B. Kannan, "Acquisition Performance of an Ultra Wide-band Communications System over a Multiple-Access Fading Channel", *UWBST 2002*

[20] Fleming, R.; Kushner, C.; Roberts, G.; Nandiwada, U.*;* "Rapid acquisition for ultra-wideband localizers", *Ultra Wideband Sys. and Tech., 2002*. Digest of Papers. 2002 IEEE Conf. on, 2002

[21] Wong Sai Ho; Xiaoming Peng; Madhukumar, A.S.; Chin, F.; "Rapid acquisition for multiband UWB systems: CAZAC vs. barker sequences**",** *Information, Comms. and Signal Processing, 2003 & the 4th Pacific Rim Conf. on Multimedia. Proc. of 2003 Joint Conf. of 4th Intl. Conf. on*, Vol 3, pp1727 - 1731

[22] Bartsch, E.K.; Wassell, I.J.; "Multiuser cross-correlation channel estimation for SDMA/TDMA systems**",** *Signals, Sys. & Comps*., 2001. Conf. Rec. of the 35th Asilomar Conference on , Vol 2, pp:1753 - 1757 vol.2

[23] Wai Ho Mow, "A new unified construction of perfect root-of-unity sequences**"** *Spread Spectrum Techniques and Applications Proceedings, 1996*., IEEE 4th Intl. Symposium on , Vol 3 , 22-25 Sept. 1996 pp:955 - 959 vol.3

[24] Barker, R. H., "Group synchronizing of binary digital systems in communication theory", Butterworth London 1953, pp 273-287

[25] Bomer, L.; Antweiler, M.; " Polyphase Barker sequences**",** *Elect. Letters* , Vol. 25 , Issue: 23 , 9 Nov. 1989 pp1577 – 1579

[26] J. R. Foerster, "The performance of a direct sequence spread ultra wideband system in the presence of multipath, narrowband interference, and multiuser interference," in *Proc. 2002 UWBST*, 2002, pp. 87–92.

[27] F. Ramirez-Mireles, "On performance of ultra wideband signals in Gaussian noise and dense multipath," *IEEE Trans. Veh. Technol.*, vol. 50, pp. 244–249, Jan. 2001.

[28] D. Cassioli et al., "Performance of low-complexity rake reception in a realistic UWB channel," *in Proc., 2002 ICC*, pp 763-767

[29] Qinghua Li, Rusch, L.A., "Multiuser detection for DS-CDMA UWB in the home environment**",** *Selected Areas in Commus, IEEE Journal on* , Vol 20 , Issue: 9 , Dec. 2002 pp:1701 – 1711

[30] Boubaker, N., Letaief, K.B., "A low complexity MMSE-RAKE receiver in a realistic UWB channel and in the presence of NBI**",** *Wireless Comms and Networking, 2003.* WCNC 2003. 2003 IEEE , Vol 1 , 16-20 March 2003 pp:233 - 237

[31] Qinghua Li; Rusch, L.A., "Multiuser receivers for DS-CDMA UWB**",** *Ultra Wideband Systems and Technologies, 2002*. Digest of Papers. 2002 IEEE Conference on, 21-23 May 2002 pp:163 – 167

[32] Cassioli, D., Win, M.Z., Vatalaro, F., Molisch, A.F., **"**Effects of spreading bandwidth on the performance of UWB RAKE receivers**",** *Comms., 2003. ICC '03. IEEE Intl. Conf. on* , Vol 5, 11-15 May 2003 Pages:3545 - 3549 vol.5

[33] Cassioli, D., Win, M.Z., Vatalaro, F., Molisch, A.F., "Performance of low-complexity RAKE reception in a realistic UWB channel" *Comms, 2002. ICC 2002. IEEE Intl. Conf. on* , Vol 2 , 28 April-2 May 2002 Pages:763 - 767 vol.2

[34] G. Durisi, J. Romme, S. Benedetto, "Performance of TH and DS UWB Multiaccess Systems in Presence of Multipath Channel and Narrowband

interference", *IWUWBS 2003,* Oulu, Finland,2-5 June 2003. http://www.whyless.org/files/public/IWUWBS2003_Durisi.pdf

[35] Rajeswaran, A.; Somayazulu, V.S.; Foerster, J.R. "RAKE performance for a pulse based UWB system in a realistic UWB indoor channel**",** *Comms. 2003. ICC '03. IEEE Intl. Conf. on*, Vol 4 , 11-15 May 2003 Pages:2879 - 2883 vol.4

[36] B. Holter and G. E. Øien, "The optimal weights of a maximum ratio combiner using an eigenfilter approach", in Proc. *5th IEEE Nordic Signal Processing Symposium (NORSIG-2002)*, Hurtigruten, Norway, October 2002.

[37] Xiaoming Peng; Wong Sai Ho; Madhukumar, A.S.; Chin, F.; "A simplified coding and interleaving method for multi-band UWB systems: a performance comparison**"** *Information, Comms. and Signal Processing, 2003 & the 4th Pacific Rim Conf. on Multimedia. Proc. of 2003 Joint Conf. of 4th Intl. Conf. on*, Vol 3, pp 1742 – 1746

[38] Stephen G. Wilson; "Digital Modulation and Coding", Prentice-Hall, Inc., 1996

[39] Kasami, T.; Takata, T.; Fujiwara, T.; Lin, S.; "A concatenated coded modulation scheme for error control**"** *Comms., IEEE Trancs. on* , Vol: 38 , Issue: 6, Jun 1990 pp:752 – 763

[40] R. Fisher, R. Kohno, H. Ogawa, H. Zhang, K. Takizawa "DS-UWB proposal proposal update" ftp://ftp.802wirelessworld.com/15/04/15-04-0140-02-003a-merger2-proposal-ds-uwb-presentation.ppt

[42] Kasami, T.; Takata, T.; Fujiwara, T.; Lin, S.; "A concatenated coded modulation scheme for error control**"** *Comms., IEEE Trancs. on* , Vol: 38 , Issue: 6, Jun 1990 pp:752 – 763

[43] Mielczarek, B.; Wessman, M.; Svensson, A.; "Performance of coherent UWB rake receivers with channel estimators" *Vehicular Technology Conference, 2003. VTC 2003-Fall.* 2003 IEEE 58th , Vol: 3 , 6-9 Oct. 2003

List of Publications

Published Journal Paper:

1. Wong Sai Ho; Madhukumar, A.S.; Chin, F.; "Peak-to-average power reduction using partial transmit sequences: a suboptimal approach based on dual layered phase sequencing**"** *Broadcasting, IEEE Trans. on*, Vol: 49 , Issue:2 , Jun 2003 pps:225 – 231

Published Conference Papers:

2. Wong Sai Ho; Madhukumar, A.S.; Chin, F.; "A novel two-layered suboptimal approach to partial transmit sequences**"** *VTC 2003-Spring. The 57th IEEE Semiannual*, Vol: 2, 22-25 Apr 2003 pp:1268 - 1272 vol.2
3. Xiaoming Peng; Wong Sai Ho; Madhukumar, A.S.; Chin, F.; "A simplified coding and interleaving method for multi-band UWB systems: a performance comparison**"** *Information, Comms. and Signal Processing, 2003 & the 4th Pacific Rim Conf. on Multimedia. Proc. of 2003 Joint Conf. of 4th Intl. Conf. on*, Vol 3, pp 1742 – 1746
4. Wong Sai Ho; Madhukumar, A.S.; Chin, F.; "Conventlonal quadrature mixer for impulse radio receivers- filter design issues**"** *PIMRC 2003. 14th IEEE Proceedings on*, Vol 3 , Sept. 7-10, 2003 pp 2716 – 2720
5. Wong Sai Ho; Xiaoming Peng; Madhukumar, A.S.; Chin, F.; "Rapid acquisition for multiband UWB systems: CAZAC vs. barker sequences**",** *Information, Comms. and Signal Processing, 2003 & the 4th Pacific Rim Conf. on Multimedia. Proc. of 2003 Joint Conf. of 4th Intl. Conf. on*, Vol 3, pp1727 – 1731

Submitted Journal Paper:

6. Wong Sai Ho, Xiaoming Peng, Chin F., Madhukumar A.S., "Performance Analysis of an Over-Sampling Multi-channel Equalization for a Multi-Band UWB System", *Wireless Comms, IEEE Transactions on*